UNIVERSITY of CALIFORNIA
Santa Barbara

Understanding Turbulence in Massive Star Envelopes: Impacts of Near-Surface Convection Zones on Stellar Envelope Structure and Observables

A dissertation submitted in partial satisfaction of the
requirements for the degree of

Doctor of Philosophy

in

Physics

by

William C. Schultz

Committee in charge:

Professor Lars Bildsten, Chair

Professor Timothy Brandt

Professor Omer Blaes

June 2023

The dissertation of William C. Schultz is approved:

Professor Omer Blaes

Professor Timothy Brandt

Professor Lars Bildsten, Chair

June 2023

This work is dedicated to my family.

To my loving parents, Susan and David Schultz, whose unwavering love and support helped me through thick and thin. To my grandmother Joyce Dougherty who helped raise me, keeps me grounded, and reminds me to continue seeking fun.

And to my future family, specifically my lovely fiance, Sarah Steiger, without whom my graduate career would not have been the same.

Acknowledgements

I would like to start by acknowledging the tremendous privilege it is to be able to do this work, and to be welcomed into the astronomical community. I would also like to acknowledge my personal privilege in arriving at this position. I am the son of two PhDs (Physics and Science Education) and a third generation Physics BA from UC Berkeley. I was perfectly poised to address the challenges of graduate school and I applaud everyone who has reached this same pinnacle without the privileges I have benefited from.

I could not have asked for a better PhD advisor, Lars Bildsten, who perpetually supported me and allowed me to grow as a researcher. I thank him for the years of thought-provoking conversations, guidance, patience, encouragement, feedback, and interesting project ideas. His insight into all things stellar is expansive; his love for astrophysics genuine, inspiring, and contagious; and his leadership unparalleled. I would not be the researcher, writer, scientist, and human I am today if it were not for his mentorship.

I thank Yan-Fei Jiang for his scientific guidance, technical expertise, and for implementing and utilizing incredible tools to solve challenging computational problems. He always humbles me with his quick thinking and endless expertise on all things computational and physical. It has been a pleasure to work with him and I have learned more than I can recount in this short acknowledgement.

Benny T.H.-Tsang has also been essential to my PhD experience. Ever since we wrote our first paper together while he was a postdoc at KITP, he has been an amazing mentor, colleague, and friend. I will always cherish our lengthy discussion on topics ranging from advanced Monte Carlo frequency dependent radiation transport to sourdough bagel recipe tweaking and look forward to many more discussions to come.

I would like to thank Bill Paxton, Adam Jermyn, and the whole MESA Development team. You have revolutionized the field towards open-source, reproducible work, sending ripples through all of astronomy. I would also like to recognize the tremendous value of my conversations and connections within the Zwicky Transient Facility Theory Network, academic conferences, and all of my extended collaborations. I especially thank Eliot Quataert, Matteo Cantiello, Jorick Vink, and Dan Kasen. I would also like to thank the other members of my committee, Timothy Brandt and Omer Blaes, for their moral and intellectual support as well as their guidance throughout my PhD.

My friends and colleagues in and out of academia also made this work possible. I especially thank the other members of the Bildsten group for vibrant conversations and insight, computational prowess, aesthetic feedback, and so much more. Thank you to my academic "siblings" Evan Bauer, Jared Goldberg, Bill Wolf, and Sunny Wong, former and current postdocs Jennifer Barnes, Rocio Kiman, May Gade Pedersen, Logan Prust, Chris White, and Hang Yu. It has also been a pleasure to converse with and learn from my other officemates, Stephanie Ho and Mike Lipatov. I also must acknowledge my fellow cohort of grad students, especially Remi Boros, Zhitao (Tom) Chen, Joe Costello, Sergio Hernandez Cuenca, Aaron Kennon, Aleksei Khindanov, Seamus O'Hara, Noah Swimmer, Brendt Tan, Navin Tsung, and Mark Turiansky. I thank those friends who have allowed me to flourish at home and helped me stay sane during the pandemic that

swept the globe: Joshua Straub, Iman Salty, Paige Fitzgibbon, and Sophie McComb. I have also been lucky enough to have many old friends who have been a crucial source of moral support throughout these years: Katie Coyne, Sam Falkenhagen, Scott Gharda, Justin Hom, David McDonnaugh, Austin McDowell, Jordan Petersen,Gavin Rae, and Joe Zalesky.

I thank the KITP staff for making me and many other scholars feel at home. Perhaps most importantly, I thank the custodians, groundskeepers, support staff, and all those who maintain our spaces and enable us to do this work. Without you, science and discovery and society do not and cannot progress.

These acknowledgements cannot be complete without expressing my limitless gratitude for the boundless support of my family. My parents, Susan and David, who had me performing basic chemistry experiments in our kitchen when I was 4 years old, have always encouraged me to be curious, and provided a safe and loving environment that allowed me to flourish both academically and personally. My grandmothers, Joyce Dougherty, Marj Schultz, and Ute Schultz, who helped raise me to be kind and considerate and always ensured I continue to seek fun and enjoy life. My grandfather and namesake, Cramer William Schultz, who showed me what true strength meant as he battled with Alzheimers throughout my childhood. And lastly my grandfather Dennis Dougherty, whom I never met but always feel a connection to when I look up at the star-filled night sky.

This dissertation would not have been possible without the love and support of my fiance, Sarah Steiger, whom I met my first year and have loved ever since. She means the universe to me and I am very excited for our future together. The love and support from her family has also been amazing as they have welcomed me with open arms and made me feel a part of their large family from day one.

I am certain that there are individuals who deserve acknowledgement whose names do not appear above. If you are reading this and your name did not appear above, I am immensely thankful to you for reading this work.

Curriculum Vitæ

William C. Schultz

Education

2023	*Ph.D., Physics*, University of California, Santa Barbara, CA, USA
2020	*M.A., Physics*, University of California, Santa Barbara, CA, USA
2017	*B.A., Physics & B.A., Astrophysics*, University of California, Berkeley, CA, USA

Publications

"Turbulence Supported Massive Star Envelopes ," **William C. Schultz**, Lars Bildsten, and Yan-Fei Jiang, Submited to *The Astrophysical Journal Letters* (2023)

"Synthesizing Spectra from 3D Radiation Hydrodynamic Models of Massive Stars Using Monte Carlo Radiation Transport," **William C. Schultz**, Benny T.-H. Tsang, Lars Bildsten, and Yan-fei Jiang, *The Astrophysical Journal*, 945, 58 (2023)

"Stochastic Low-frequency Variability in Three-dimensional Radiation Hydrodynamical Models of Massive Star Envelopes," **William C. Schultz**, Lars Bildsten, and Yan-Fei Jiang, *The Astrophysical Journal Letters*, 924, L11 (2022)

"Convectively Driven 3D Turbulence in Massive Star Envelopes. I. A 1D Implementation of Diffusive Radiative Transport," **William C. Schultz**, Lars Bildsten, and Yan-fei Jiang, *The Astrophysical Journal*, 902, 67 (2020)

"Deep Neural Network Classifier for Variable Stars with Novelty Detection Capability," Benny T.-H. Tsang, **William C. Schultz**, *The Astrophysical Journal Letters, 877, L14* (2019)

Abstract

Understanding Turbulence in Massive Star Envelopes:

Impacts of Near-Surface Convection Zones on

Stellar Envelope Structure and Observables

by

William C. Schultz

Modeling of massive star ($M > 10\,M_{\odot}$) outer envelopes has remained a challenge for decades. Due to the complex physics involved, 1D models of stellar envelopes can only be evolved under many approximations that attempt to incorporate (or alleviate) the intricate interactions between matter and radiation. To reveal the multi-dimensional nature of massive star envelopes, we performed 3D radiation hydrodynamic simulations of the main sequence and post-main sequence evolution of massive stars using `Athena++`. These 3D models capture the detailed structures and interactions of the gas and radiation fields, in particular the time-dependent, vigorous turbulence excited by iron and helium opacity peaks in the near-surface convection zones. This turbulence becomes trans-sonic and creates large density fluctuations that propagate to the surface, eliminating the common notion of a spatially confined convection zone and a constant-radius photosphere. Strong anti-correlations between radiation flux and density decrease the radiation pressure force by up to 80%, rendering the dynamical pressure of the turbulence

essential in maintaining force balance. As predicted by Henyey et. al. (1965), we show that this turbulent pressure support impacts the adiabatic temperature gradient and significantly reduces the superadiabaticity of these convection zones. Turbulent motions propagating to the surface from the Fe convection zone have significant observational impacts. The dynamic surface topography generates stochastic low-frequency brightness variability that is consistent with that observed in similar stars by recent photometric surveys (e.g. TESS). Additionally, we used the frequency-dependent Monte Carlo radiation transport code `Sedona` to self-consistently synthesize the spectral features of these turbulent stellar envelopes, revealing that the time-dependent surface velocities generate spectral line broadening and variability. Our work proposes future improvements to 1D stellar evolution models and suggests the need for a novel understanding of how turbulent surface velocities affect spectral line profiles.

Contents

1 Introduction **1**
- 1.1 Massive Stars and Near-Surface Convection Zones . . . 1
- 1.2 Recent Massive Star Observations . . . 3
- 1.3 Radiative Leakage in Convective Dynamics . . . 5
- 1.4 Summary . . . 6
- 1.5 Software . . . 8
- 1.6 Permissions and Attributions . . . 9

2 Investigating Correlations in 3D RHD Stellar Envelope Models **10**
- 2.1 3D Simulations of Massive Star Envelopes . . . 12
  - 2.1.1 3D Radial Variations . . . 14
  - 2.1.2 Correlation of Flux, Opacity, and Density . . . 19
  - 2.1.3 Pseudo-Mach Number Definition and Value . . . 23
  - 2.1.4 Variance and Covariance of Density and Radiative Flux . . . 28
- 2.2 Calibrating the Impact of Fluctuations on Optically Thick Transport . . . 31
- 2.3 Domain of Applicability in 1D Models and Future Work . . . 39
- 2.4 Conclusion . . . 43

3 The Impact of Turbulence on Stellar Structure **45**
- 3.1 Hydrostatic Balance in 3D Models of Turbulent Envelopes . . . 47
- 3.2 Comparing Averages of 3D Models to 1D Profiles . . . 51
  - 3.2.1 Extracting 1D Models from 3D Wedges . . . 52
  - 3.2.2 Comparing to MESA Models . . . 55
  - 3.2.3 Temperature Gradients in Turbulent Envelopes . . . 58
- 3.3 Conclusions . . . 59

4 Photometric Variability from Near-Surface Convection Zones **61**
- 4.1 3D Models . . . 62
  - 4.1.1 Computational Methods . . . 63
  - 4.1.2 Model Parameters and Characteristics . . . 64
- 4.2 Comparisons to Observations . . . 68
  - 4.2.1 Near-Surface Convection and Surface Velocities . . . 69
  - 4.2.2 Stochastic Low Frequency Variability . . . 71

4.3 Conclusion 76

5 Spectroscopic Synthesis from Turbulent Massive Star Envelopes in 3D 78
5.1 3D Gray Radiation Hydrodynamic Modeling 83
5.1.1 `Athena++` Model Description 84
5.1.2 Photospheric Definition in a Clumpy Surface 88
5.2 Post-Processing Using Monte Carlo Methods 95
5.2.1 Verifying Novel Modifications: Comparing Gray Radiation Transport 98
5.3 Synthesizing Spectra via Post-Processing 101
5.4 Variety in Synthetic Spectra of 3D Envelope Models 106
5.4.1 Viewing Angle Dependence 106
5.4.2 Synthetic Spectral Profiles 111
5.4.3 The Effect of Micro- and Macroturbulence 114
5.4.4 Thermal Profile Comparison 116
5.5 Conclusion 117

6 Future Directions 119

A 1D Velocity Estimates 124

Bibliography 129

Chapter 1

Introduction

1.1 Massive Stars and Near-Surface Convection Zones

Massive stars are at the forefront of astrophysical research, due in part to their rapid evolution on the main sequence, and soon thereafter, their explosions caused by the emergence of a strong shock from the collapsed core. However, they also play a fundamental role in many astrophysical environments. The ionizing radiation from massive stars was important in the reionization of the early universe (Bromm & Larson, 2004). This radiation, along with strong winds and chemical elements produced by massive stars, are important feedback mechanisms that regulate star formation and the structure of the interstellar medium in galaxies (Kennicutt, 2005; Smith, 2014). The explosions of massive stars produce various types of supernovae and high energy transients and leave behind black holes and neutron stars. The properties of both the explosions as well as the remnants depend strongly on the evolution of the massive star progenitor (Heger et al., 2003;

Farmer et al., 2016).

For stars with near solar metallicity, the opacity increase associated with iron at $T \approx 1.8 \times 10^5$ K and helium at $T \approx 2 \times 10^4$ K imply locally super-Eddington luminosities (e.g. Paxton et al., 2013, and references therein). These opacity increases lead to near-surface convection zones (NSCZs), radially thin regions in the outer $\lesssim 10\%$ of the stellar envelope that are unstable to convection (Cantiello et al., 2009). As these NSCZs are close to the surface, they are expected to have observational impacts (e.g. Grassitelli et al., 2015), however their confined extents in 1D models lead to questions about their impact on stellar surfaces (e.g. Bowman et al., 2020). However as one dimensional (1D) modeling of massive stars in these regimes is notoriously challenging, no coherent consensus has been reached.

In NSCZs, the locally super-Eddington luminosities lead to a dominance of radiation pressure over that of the gas (Crowther, 2007; Maeder et al., 2012; Sanyal et al., 2015). In these regimes, 1D stellar models yield density and gas pressure inversions (Joss et al., 1973; Gräfener et al., 2012; Paxton et al., 2013; Owocki, 2015) that trigger new convective instabilities. These instabilities stymie 1D models when the iron opacity peak is close to the surface where mixing length theory (MLT; Cox & Giuli 1968) convection is super-sonic. As MLT velocities cannot surpass the sound speed, the convective energy transport cannot carry the necessary luminosity resulting in erroneous stellar structure estimates. In the absence of an improved 1D modeling approach, stellar modelers simply bypass this obstacle with explicit "patches" that enable continued evolution (e.g. Stothers & Chin,

1979; Maeder, 1987; Paxton et al., 2013). However, these "patches" have not yet been tested for physical accuracy and a physically motivated solution is highly desired (e.g. Figure 20 of Köhler et al., 2015).

Recent three dimensional (3D) calculations (Jiang et al., 2015, 2018) found surprising properties of these massive star envelopes. For example, the 3D models revealed that the velocity and density fluctuations from the iron opacity peak convection zones (FeCZs) propagate well out to the stellar photosphere (Jiang et al., 2015, 2018), eliminating the intervening radiative layer predicted in 1D models. Even further out, Jiang et al. (2018) showed that helium recombination causes an even larger increase in opacity that can lead to a continuum driven wind. Though these 3D models provide important information regarding the dynamics in massive star envelopes, they take over ten million CPU hours to resolve the steady-state behavior for ≈ 10 days of model time. Hence in order to see how massive stars evolve throughout their lives, accurate 1D modeling is required. Additionally, in order for 1D models to be improved based on these 3D simulations, a wide variety of stars must be modeled to generate a prescription that accurately interpolates between the different stellar regimes.

1.2 Recent Massive Star Observations

The turbulent convection in the FeCZ likely plays a dynamical role, exciting plumes that reach the surface and cause photometric brightness variability and spectroscopic line broadening (Cantiello et al., 2009). In agreement with the theoretical models, observa-

tions of massive stars exhibit clear signs of highly turbulent surfaces.

The Transiting Exoplanet Survey Satellite (TESS, Ricker et al., 2015) has observed many O- and B- stars and found that nearly all exhibit brightening variations at low frequencies, $\nu \lesssim 10^{-4}\,\mathrm{Hz}$, or 10 cycles per day (Bowman et al., 2019a; Burssens et al., 2020). Termed stochastic low-frequency (SLF) variability, it is thought to be produced by large scale turbulent motions. The physical mechanism that generates this SLF variability could have several origins: turbulent plumes from near-surface convection zones (Cantiello et al., 2021; Schultz et al., 2022), internal gravity waves (IGWs) launched from the convective core (Aerts & Rogers, 2015; Edelmann et al., 2019), and wind variability and dynamics (Krtička & Feldmeier, 2021). Though near-surface convection zones appear to generate the same trend as the observed SLF variability strength and characteristic frequency (Cantiello et al., 2021; Schultz et al., 2022), the question still remains worthy of exploration across the Hertzsprung-Russell (HR) diagram.

Additionally, the large-scale fluctuations thought to produce this photometric variability, irregardless of origin, must be correlated with substantial photospheric velocities that impact spectral lines. There are many spectroscopic surveys investigating line broadening from stellar atmospheres across the HR diagram. One particular example is the IACOB project which has specifically looked at massive stellar spectra and attempted to quantify their surface velocity fields (Simón-Díaz et al., 2010, 2014, 2017, 2018; Holgado et al., 2022). They attempt to disentangle the impact of rotation ($v \sin i \approx 100\,\mathrm{km\,s^{-1}}$) with two distinct turbulent velocity fields, microturbulence ($\xi \approx 10\,\mathrm{km\,s^{-1}}$) on small

scales and macroturbulence ($v_{\rm macro} \approx 100\,{\rm km\,s^{-1}}$) on larger scales (see Ch. 5 for further discussion).

Analyzing spectral lines from these massive stars is a distinct additional probe, as photospheric spectral lines are broadened by the velocity fields in the emitting regions. Analysis of 2D models by Rogers et al. (2013) suggested that IGWs could generate photospheric spectral line variability that could be observable by future surveys (Aerts & Rogers, 2015). Other 1D models of NSCZs indicate that they can reproduce similar magnitude velocity fields (Cantiello et al., 2009; Grassitelli et al., 2015). However, full 3D frequency dependent radiation hydrodynamic (RHD) models have not been computed to verify or refute these claims.

1.3 Radiative Leakage in Convective Dynamics

In discussions of convection in the cores of massive stars, the convective efficiency often refers to a comparison between the convective velocity and the sound speed. Supersonic plumes create shocks resulting in a loss of heat transport efficiency when compared to the subsonic case. In NSCZs, a second impedance to convective energy transport dominates the inefficiencies. As plumes rise, they lose their heat via radiative diffusion to the surrounding stellar background.

As discussed in Goldberg et al. (2021); Jermyn et al. (2022); Schultz et al. (2022, 2023), the convective efficiency associated with this radiative leakage can be quantified by the parameter $\gamma \sim P_{\rm th} v_{\rm c} \tau / P_{\rm rad} c$, where $v_{\rm c}$ is the convective velocity, c is the speed of

light, and the total thermal pressure, $P_{\rm th} = P_{\rm g} + P_{\rm r}$, where $P_{\rm g}$ and $P_{\rm r}$ are the gas and radiation pressure respectively. This is essentially comparing convective energy transport to local radiative diffusion. When $\gamma < 1$, substantial radiation losses occur in moving fluid elements, defining a critical optical depth,

$$\tau_{\rm crit} = \frac{P_{\rm r} c}{(P_{\rm r} + P_{\rm g}) v_{\rm c}}. \tag{1.1}$$

Thus if a convective zone lies at $\tau > \tau_{\rm crit}$, we expect convective energy transport to dominate there. Otherwise, though still convective, the majority of the luminosity is carried via radiative diffusion in the turbulent medium. In massive stars, $\tau_{\rm crit} \gtrsim 1000$, yielding large regions of these stellar envelopes susceptible to inefficient convection which has only recently been achieved in full 3D radiation hydrodynamical (RHD) simulations (Jiang et al., 2015, 2018). This dissertation focuses on the analysis of these and novel 3D RHD models to provide insights into this novel regime of convective energy transport.

1.4 Summary

This dissertation is divided into two main sections. The chapters 2 and 3 discuss the theoretical implications of our novel 3D RHD stellar envelope models, while chapters 4 and 5 investigate their observational implications.

In Ch. 2, we highlight the many order of magnitude spatial fluctuations seen in physical quantities in our 3D RHD `Athena++` models. We then investigate correlations between density and radiative flux in two Hertzsprung Gap models. The correlations combine with the significant spatial variability to reduce the radiation pressure support

expected from 1D analogs. The impact is quantified and a fitting function is generated to investigate the potential implications in future 1D models.

Ch. 3 introduces three additional main sequence `Athena++` simulations and investigates the correct methodology to extract 1D averages from 3D models. We then confirm the force balance between pressure gradients and gravity in turbulent stellar envelopes. Comparing several temperature gradients from the 1D averages of the 3D models, we diagnose the energy transport in all five simulations. We confirm that Henyey et al. (1965) correctly predicted the impact of turbulence on the adiabatic temperature structure in massive star envelopes when the turbulence is trans-sonic. Lastly, two distinct regimes arise where stellar envelopes are either nearly spherically symmetric or inherently 3D, and thus require more advanced modeling methodologies.

Shifting towards the observational impacts, we investigate the origin of SLF variability using three models in Ch. 4. We find our ab initio simulations produce similar SLF variability to observations with similar characteristic frequencies and amplitudes, suggesting NSCZs are responsible for this photometric brightness variability in certain regions of the HR diagram. We highlight the lack of confinement in the 3D realizations of NSCZs, completely breaking from the 1D calculations and suggesting they impact photospheric observations more than previously predicted.

In these previous analyses, we noticed that the surfaces of the 3D RHD models with significant turbulence are inherently non-uniform with complex surface topography breaking the 1D notion of a single effective temperature and photospheric radius. These 3D

structures combined with the substantial velocity fields at the surfaces made it clear these stars should have broad photospheric lines. Thus we decided to pursue a frequency dependent post-processing methodology. In Ch. 5 we expand upon the Monte Carlo frequency dependent code, `Sedona`, to post-process our gray 3D RHD `Athena++` models and synthesize photospheric absorption lines. After confirming the gray transport agreed between the two independent radiation implementations, we modeled photospheric lines from three RHD models and highlighted the impact the surface velocities had on spectroscopically derived velocity estimates.

1.5 Software

This work is fundamentally based on utilization of the 3D fluid simulation software instrument `Athena++` (Stone et al., 2020), and in particular, the radiation-hydrodynamics modules described by Jiang et al. (2014); Jiang (2021). It has also greatly benefited from the use of the open-source software instrument `MESA` (Modules for Experiments in Stellar Astrophysics). The `MESA` instrument papers are often referred to using roman numerals: Paxton et al. (2011, MESA I), Paxton et al. (2013, MESA II), Paxton et al. (2015, MESA III), Paxton et al. (2018, MESA IV), Paxton et al. (2019, MESA V), and Jermyn et al. (2023, MESA VI).

Analysis made significant use of the following packages: `py_mesa_reader` (Wolf & Schwab, 2017), `NumPy` (Harris et al., 2020), `SciPy` (Virtanen et al., 2020), and `matplotlib` (Hunter, 2007). Figure colors made use of the additional `python` packages `cmocean`

(Thyng et al., 2016) and `cmasher` (van der Velden, 2020).

1.6 Permissions and Attributions

1. The content of Chapter 2 is adapted and reproduced from Schultz et al. (2020) with permission from *The Astrophysical Journal*.

2. The content of Chapter 3 is adapted and reproduced from work submitted to *The Astrophysical Journal Letters* to be published in 2023.

3. The content of Chapter 4 is adapted and reproduced from Schultz et al. (2022) with permission from *The Astrophysical Journal Letters*.

4. The content of Chapter 5 is adapted and reproduced from Schultz et al. (2023) with permission from *The Astrophysical Journal*.

My graduate work has also afforded me the opportunity to participate in an exciting and tangential research effort. In collaboration with Benny T.-H. Tsang, we generated a novel neural network classifier of variable star light curves (Tsang & Schultz, 2019). Unfortunately, this work does not appear in this dissertation.

Chapter 2

Investigating Correlations in 3D RHD Stellar Envelope Models

In this chapter, we present a new prescription to calculate radiation pressure gradients in the outer layers of 1D models of massive stars. Our prescription incorporates the correlations between fluctuations of density and radiative flux observed in the 3D models of Jiang et al. (2018). As these stars are radiation pressure dominated, accurately determining the radiation pressure gradient is fundamental to the structure of their stellar envelopes throughout the stars' evolution. In developing the prescription, we also identified a useful independent parameter to identify regions of inefficient convection across different 3D models with different masses and luminosities.

Strong effects caused by the correlation between density and radiative flux in optically thin, $\tau \lesssim 1$, have been detailed in previous literature. Many investigations that

considered the interaction between density fluctuations and radiation in the context of radiation-driven turbulent winds in star forming regions, finding significant effects from their correlation (e.g. Krumholz & Thompson, 2012; Davis et al., 2014; Rosdahl & Teyssier, 2015; Tsang & Milosavljević, 2015). Krumholz & Thompson (2013) noted the pronounced effect this correlation has on estimations of the asymptotic momentum of dusty, radiative driven winds. Tsang & Milosavljević (2018) observe a sizable effect of the correlation between radiative flux and density in the super star cluster formation and evolution. Recently, many advances have been made towards characterizing the effect of density fluctuations on the radiation transport through clumpy stellar winds (e.g. Owocki & Sundqvist, 2018, and references therein). Despite these correlations being observed, no work has been able to reproduce the effect of these correlations in either 1D evolution or subgrid recipe contexts. Though these correlations have been identified in other astrophysical environments, proper analysis has not been applied to the optically thick, $\tau \gg 1$, regions of massive star envelopes.

The remainder of the chapter is organized as follows. In § 2.1 we detail the 3D models used in our analysis, characterizing fluctuations in density and radiative flux, and quantifying their variance and covariance. We also introduce a new independent parameter that characterizes the turbulent convection. § 2.2 describes our proposed prescription as well as providing evidence for its efficacy. We discuss the implications of our prescription in future 1D stellar evolution models in § 2.3, and summarize our key results in § 2.4.

2.1 3D Simulations of Massive Star Envelopes

The 3D simulations used in this work modeled the outer $< 1\%$ of massive star envelopes with the radiation magneto-hydrodynamic (MHD) code `Athena++` (Stone et al., 2020). The code solves the ideal hydrodynamic equations coupled with the time-dependent, frequency-integrated radiation transport equation for specific intensities over discrete angles based on the numerical algorithm as described by Jiang et al. (2014). All the simulations are done in the spherical polar coordinate with effective resolution $512 \times 512 \times 256$ covering the radial, longitudinal ($\phi \in [0, \pi]$) and latitudinal ($\theta \in [\pi/4, 3\pi/4]$) directions. The angular grid for the radiation field are constructed in the same way as specified in Davis et al. (2012). Results for three simulations were briefly described by Jiang et al. (2018) and are being additionally studied in a paper in preparation. Here we include a few additional models with different metallicities. The physical characteristics of the models are listed in Table 2.1. These include the core mass beneath the model, $M_{\rm core}$, the envelope mass being simulated, $M_{\rm env}$, the effective temperature, $T_{\rm eff}$, the luminosity, L, the Eddington luminosity for electron scattering, $L_{\rm Edd} = 4\pi G M_{\rm core} c/\kappa_{\rm es}$, and the radial location of the bottom, $r_{\rm base}$, and the top, $r_{\rm max}$, of the model grids. We also show the radial location where the expected value of optical depth to infinity is unity, $r_{\rm ph}$, the radial location and optical depth at the iron opacity peak, $r_{\rm Fe}$ and $\tau_{\rm Fe}$, and the metallicity, Z. We focus here on the 3D model properties when they have reached a steady-state equilibrium, allowing us to assume that optically thick regions have reached local thermal equilibrium. Despite the models reaching steady-state they still exhibit luminosity

Table 2.1: Properties of the 3D Stellar Models

Model Name	Masses		Temperature	Luminosities	
	$M_{\rm core}$	$M_{\rm env}$	$T_{\rm eff}$	L	$L_{\rm Edd}$ [a]
	($M_\odot$)	($M_\odot$)	(10^3 K)	($\log(L/L_\odot)$)	($\log(L/L_\odot)$)
M56HG	56	0.13	9	6.20	6.26
M80HG	80	0.011	19	6.40	6.42
M56HGZ0.1	56	0.13	9	6.20	6.26
M80HGZ0.1	80	0.011	19	6.40	6.42
M80HGZ2	80	0.011	19	6.40	6.42

Model Name	Radii				Optical Depth	Metallicity
	$r_{\rm base}$	$r_{\rm max}$	$r_{\rm ph}$ [b]	$r_{\rm Fe}$	$\tau_{\rm Fe}$	Z
	($R_\odot$)	($R_\odot$)	($R_\odot$)	($R_\odot$)		($Z_\odot$)
M56HG	35.0	809.8	353.3	80.3	28,000	1
M80HG	16.3	335.5	99.0	44.0	5,400	1
M56HGZ0.1	35.0	809.8	322.5	87.5	16,000	0.1
M80HGZ0.1	16.3	335.5	102.2	45.7	3,100	0.1
M80HGZ2	16.3	335.5	104.7	45.7	8,300	2

[a] For an assumed electron scattering opacity.
[b] The photosphere radii specified are where $\langle\tau(r_{\rm ph})\rangle = 1$ (see Equation 2.1).

variations on the order of 50% on time scales of days (Jiang et al., 2018). These envelope models only account for the gravitational accelerations caused by the cores, which account $> 99\%$ of the stellar mass. The models do not include any initial rotation. In this paper, we use model M56HG to investigate the properties of the turbulent envelopes (§ 2.1.1), models M56HG and M80HG to quantify the variations in density and radiative flux (§ 2.1.4), and the remaining three models (M56HGZ0.1, M80HGZ0.1, M80HGZ2) to test the prescription we developed (§ 2.3).

Throughout these envelope models, the radiation pressure is substantially larger than the gas pressure by nearly a factor of 10. However, as the optical depth decreases at larger radii, the photons can no longer support the gas against local compression and the gas

pressure becomes dominant post-shock support. This occurs at a critical optical depth defined as $\tau_{\rm c} \approx c/c_{\rm g,0}$ where $c_{\rm g,0}$ is the isothermal gas sound speed at the iron opacity peak (Jiang et al., 2015). The iron opacity peak is a convenient choice as it typically instigates the majority of the convection in massive star envelopes and occurs at the same temperature so $\tau_{\rm c} \approx 6,300$ for all the models. In our models, the iron opacity peak causes the luminosity to become super-Eddington, causing turbulence and subsequent density fluctuations as we shall discuss. Jiang et al. (2015) highlighted the contrast in the outcome of convective properties as a function of τ. If convection occurs at $\tau \ll \tau_{\rm c}$, the plasma is optically thick enough to be locally supported by the radiation pressure allowing the convection to be efficient and reasonably well described by classical MLT. If convection occurs at $\tau \gg \tau_{\rm c}$, the plasma is optically leaky, letting the photons escape and leaving only the minimal gas pressure to support against local perturbations. This convection will be inefficient and may behave very differently when compared to classical MLT. The models in Table 2.1 span this boundary at the iron opacity peak and, as we show, exhibit large density fluctuations as $\tau \ll \tau_{\rm c}$.

2.1.1 3D Radial Variations

One distinctive characteristic of these 3D massive star envelope simulations is the extraordinary variations in density, opacity, optical depth, and radiation flux deep in the models, at $\tau \gg 1$. At the base, where the models are entirely radiative, the opacity is dominated by electron scattering, and the luminosity is very close to the local Eddington

luminosity. As the temperature decreases outwards, the plasma cools enough for iron to cause an increase in opacity once the temperature reaches $T \approx 1.8 \times 10^5\,\mathrm{K}$, known as the iron opacity peak. This increase in opacity decreases the local Eddington luminosity causing the stellar luminosity to surpass it, which results in vigorous convection (Joss et al., 1973; Paxton et al., 2013) that causes large density fluctuations in this region. Even further out, helium recombination causes an even larger increase in opacity; the helium opacity peak. This opacity peak is sensitive to density which, combined with the large density fluctuations of the turbulent convection, leads to radiation accelerating dense clumps. Some clumps reach the escape velocity, while most others fall back onto the star (Jiang et al., 2018). The cyclic motion of this process creates large inhomogeneities above the surface of the star and large optical depth fluctuations.

To quantify these variations, we first calculate the optical depth of a given location in the models by integrating from the location's radius to the edge of the simulation along the radial direction. The result is one τ measurement per cell or 131,072 measurements per radial shell, as set by the resolution of these simulations. For diagnostic purposes, the radial integral is adequate and so we do not calculate τ for other directions. Figure 2.1 shows the probability distributions of τ as a function of radius for a single snapshot of the M80HG model. The color represents the probability of finding a specific value of τ at a given radius. The vertical axis is logarithmic in scale and in certain regions, the optical depth spans six orders of magnitude! The black-dashed line is the radial average of τ weighted by each cell's radial area , $\langle \tau(r) \rangle$, defined by,

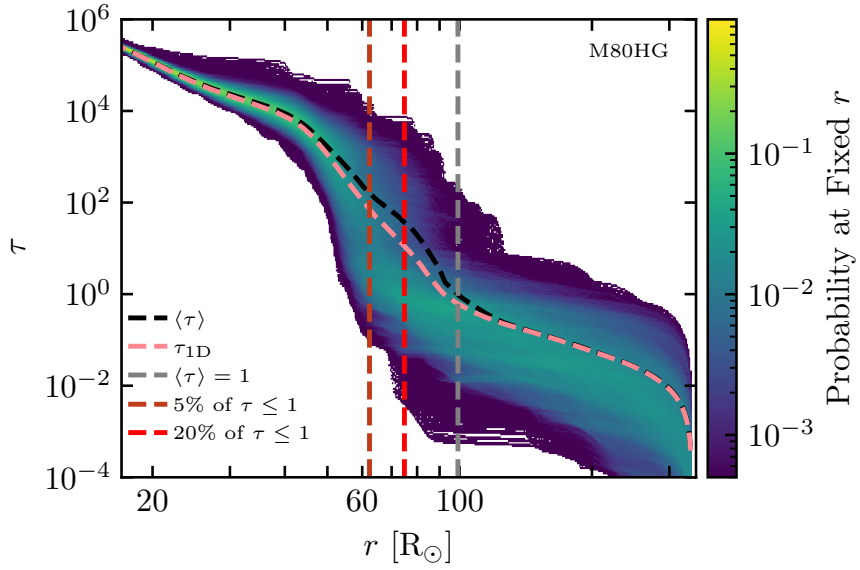

Figure 2.1: Probability mass distribution of radial optical depth, τ, to infinity as a function of radius for one snapshot of model M80HG. The optical depth is calculated by integrating radially along lines of constant angle. The black-dashed line shows the angular average of τ, weighted by the cell's area. The gray vertical dashed line shows where $\langle\tau\rangle = 1$, a typical definition of the photosphere. The pink-dashed line shows the radial profile of a 1D approximation of τ, τ_{1D} (defined in Equation 2.2). We denote the radii where 5% (dark red-dashed) and 20% (bright red-dashed) of the shell's area has an optical depth to infinity of 1 or less. Each distribution is generated from optical depths calculated in the 131,072 cells at each radius.

$$\langle \tau(r) \rangle \equiv \frac{\int_{\phi_{\min}}^{\phi_{\max}} \int_{\theta_{\min}}^{\theta_{\max}} \tau(r, \theta, \phi) d(\cos\theta) d\phi}{\int_{\phi_{\min}}^{\phi_{\max}} \int_{\theta_{\min}}^{\theta_{\max}} d(\cos\theta) d\phi}, \tag{2.1}$$

where the angle integrals are evaluated over the entire solid angle of the simulation. Angle brackets will represent angular averages at fixed radius for the remainder of the work. The pink line is the optical depth calculated from the average opacity and average density, or

$$\tau_{1\mathrm{D}}(r) \equiv \int_{r}^{r_{\max}} \langle \kappa(r') \rangle \langle \rho(r') \rangle dr', \tag{2.2}$$

where $r_{\max}$ is the outer radius of the simulation grid, listed in Table 2.1. The two red, vertical dashed lines represent the radius where 5% (dark red) and 20% (bright red) of the shell's area have an optical depth of less than 1. The percentages were chosen to approximate, to varying degrees, where the assumption of optically thick radiative transport would begin to fail. These locations are significantly different from the location of the photosphere as defined by either $\langle \tau \rangle = 1$ or $\tau_{1\mathrm{D}} = 1$.

The variations in density, ρ, radiative flux, F_r, opacity, κ, and temperature, T, are shown in Figure 2.2 for a single snapshot of model M80HG. Similarly to Figure 2.1, the color represents the probability that the quantity has the given value at that particular radius. The angle average of the quantities, shown by the black-dashed lines, mostly agree with the center of the probability distributions at all optically thick radii. The temperature has small fluctuations below the iron opacity peak and only varies by a factor of a few above it. Radiation pressure is the main source of hydrostatic support of these outer envelopes, constraining the temperature fluctuations to be relatively low

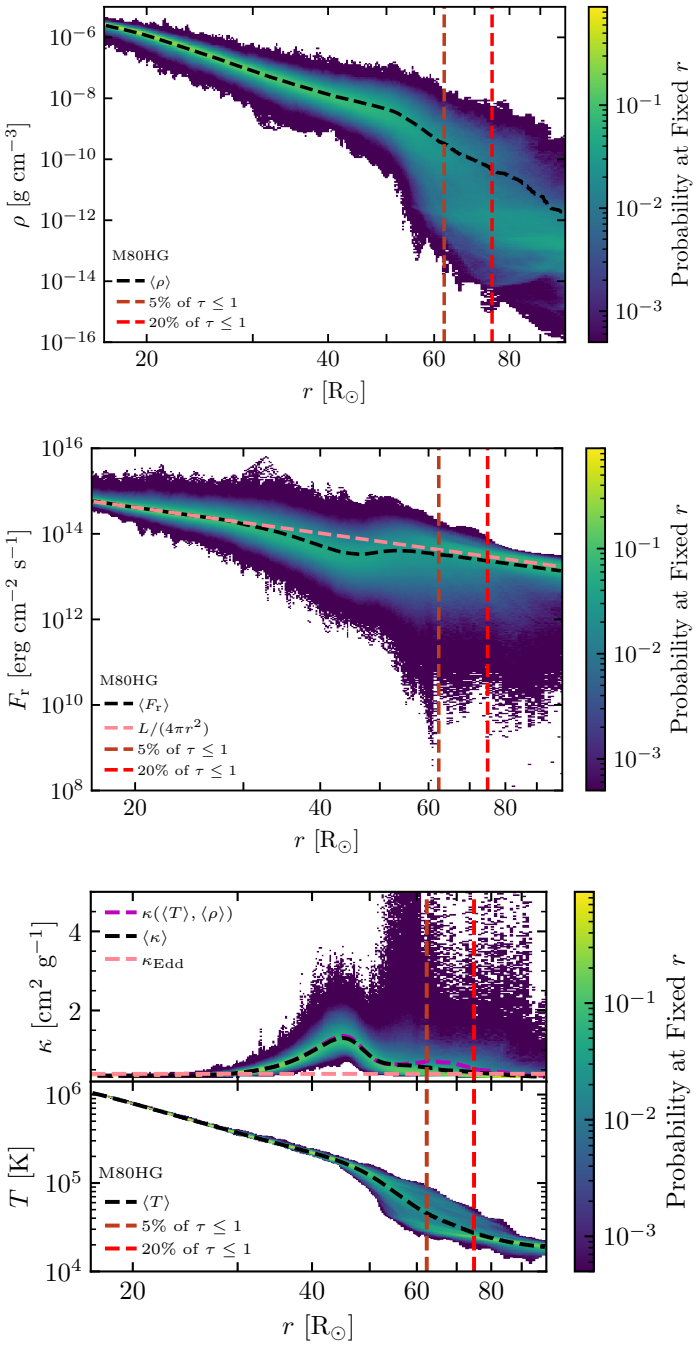

Figure 2.2: Probability mass distributions of density (top), radiative flux (middle), opacity and temperature (bottom) as a function of radius for model M80HG. The black-dashed line represents the average value. The vertical red lines are the same as in Figure 2.1, showing the radial location where an optically thick assumption would breakdown. The opacity calculated using the average temperature, $\langle T \rangle$, and average density, $\langle \rho \rangle$, (magenta-dashed line) as well as the opacity needed for a local Eddington ratio of 1 (pink-dashed line) are shown in the upper panel of the bottom figure. The pink-dashed line in middle panel represents the total average flux, $L/(4\pi r^2)$, for this snapshot. The distributions are generated from 131,072 cells at each radius.

at any fixed radius. The density variations at a fixed radius grow quickly above the iron opacity peak, where the strong turbulent motion initiates, and ρ can vary by as much as six orders of magnitude at a fixed radius. The iron opacity peak is also where the convective flux becomes comparable to the radiative flux. Comparing the average total flux, $L/(4\pi r^2)$ (pink line in middle panel of Figure 2.2), to the average radiative flux, $\langle F_r \rangle$ (black line in middle panel of Figure 2.2), shows that the convective flux is the dominant form of energy transport throughout the iron opacity peak. The turbulent convection continues to carry a significant fraction of the flux throughout the remainder of the optically thick region. The small opacity variations in the optically thick regions are due to the low levels of temperature fluctuations. Though the density variations can be large, the opacity is not very sensitive to density in these locations. However in the outer layers, helium recombination increases the opacity (up to $10\,\mathrm{cm}^2/\mathrm{g}$), giving rise to optically thick winds in these models (Jiang et al., 2018). The model is also substantially Eddington-limited for much of its radial extent as shown by the pink-dashed line in the bottom panel of Figure 2.2, which represents the opacity, κ_{Edd}, required for the local Eddington ratio to be unity. The mean opacity quickly surpasses it at the iron opacity peak.

2.1.2 Correlation of Flux, Opacity, and Density

Figure 2.3 shows the distributions of density, radiative flux, opacity, temperature, and the radiation pressure gradient as well as their correlations at three radii of model M80HG.

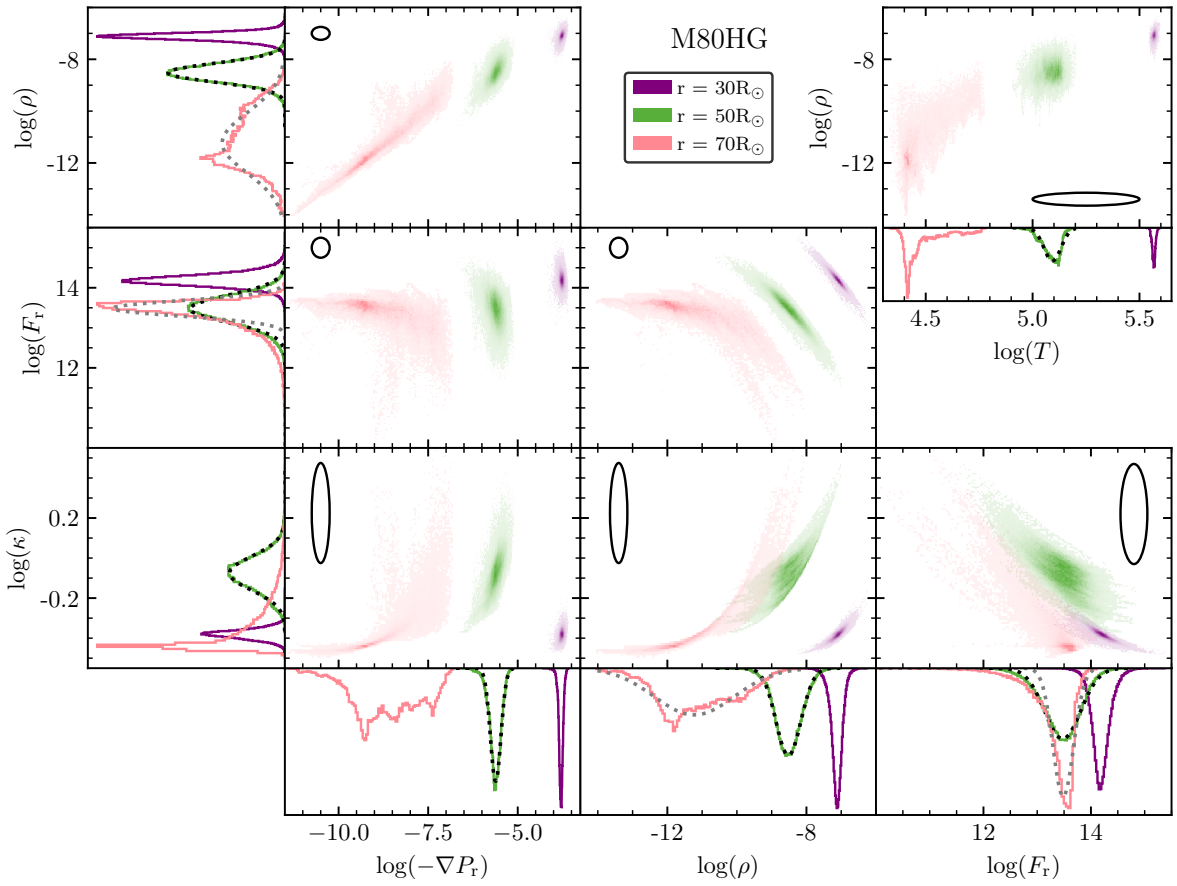

Figure 2.3: Distributions of and correlations between density, radiative flux, opacity, the radiation pressure gradient, and temperature at three radii for model M80HG. The three radii choices are just below the iron opacity peak (purple), just above the iron opacity peak (green), and where the optically thick radiative transfer assumption begins to break down (pink). The black lines are circles with the radii of $\log(x) = 0.25$ and highlight the difference in axis scaling. The black-dotted line in the distributions of density, radiative flux, opacity, and radiation pressure gradient are log-normal distribution fits to the intermediate radius choice (green). The gray-dotted line in the distributions of density and radiative flux are log-normal distribution fits to the outer radius choice (pink). Each distribution is generated by sorting the quantities in the 131,072 cells at each radius into 100 bins.

Here, and for the rest of the work, the symbol $\nabla P_{\rm r}$ is used for the radiation pressure gradient as calculated by the radial area weighted average of the diffusion equation,

$$\nabla P_{\rm r} \equiv -\frac{1}{c}\langle F_{\rm r}\,\kappa\,\rho\rangle. \tag{2.3}$$

The correlations and distributions of quantities at a radius below the iron opacity peak, $r = 30$ R$_\odot$, are shown by the purple distributions. Deep in the stellar envelope, fluctuations of all quantities follow log-normal distributions at a fixed radius and are well represented by the probability distribution function,

$$\begin{aligned} f(x) &= \frac{1}{\sqrt{2\pi}\sigma_{\ln(x)}} \exp\left(-\frac{(\ln(x)-\langle\ln(x)\rangle)^2}{2\sigma^2_{\ln(x)}}\right), \\ \text{and } \sigma^2_{\ln(x)} &\equiv \frac{\sum_{i=1}^{N}\Big(\ln(x_i)-\langle\ln(x)\rangle\Big)^2 V_i}{\sum_{i=1}^{N} V_i}, \end{aligned} \tag{2.4}$$

where $\sigma_{\ln(x)}$ is the volume-weighted standard deviation of $\ln(x)$, N is the number of angular cells at a given radius, V_i is the volume of cell i, and $\int_{-\infty}^{\infty} f(x)d(\ln(x)) = 1$. At $r = 30\,\mathrm{R}_\odot$, the temperature and opacity fluctuate by less than 25%, and the opacity is very similar to $\kappa_{\rm es}$. In contrast, the density and radiative flux vary by a factor of 10 due to convective undershooting from the turbulent motion above. The density and radiative flux are also highly inversely correlated, combining with their large fluctuations to cause variations in the radiation pressure gradient. The opacity increases with density and decreases with radiative flux. These correlations match intuition: denser regions are more opaque, making it more difficult for radiation to flow through, and vice versa. There are no strong correlations between $\nabla P_{\rm r}$ and ρ, κ, or $F_{\rm r}$ deep in the envelope.

Moving outward, the next radius choice is just above the iron opacity peak at $r =$

$50\,\mathrm{R}_\odot$ and is shown by the green distributions. The fluctuations in all quantities are larger than at $r = 30\,\mathrm{R}_\odot$ as turbulent convection is playing an important role in both pressure support and energy transport at $r = 50\,\mathrm{R}_\odot$. All the plotted distributions remain log-normal as shown by the log-normal fits (black-dotted lines in histograms), though temperature is starting to deviate. The fluctuations of opacity, temperature, and the radiation pressure gradient are still small compared to those of the density or radiative flux. The radiative flux and density are still highly inversely correlated and density and opacity are now slightly positively correlated with the radiation pressure gradient. Radiative flux and the radiation pressure gradient are slightly anti-correlated causing the fluctuations in ∇P_r to be smaller than that of either ρ or F_r. At $r = 50\,\mathrm{R}_\odot$, the convective motions behave similar to classical MLT, with hot plasma mixing upwards through cooler regions. The main difference being the turbulent velocities are trans-sonic causing the large density and thus radiative flux variations seen in the models.

The pink distributions show quantities at $r = 70\,\mathrm{R}_\odot$ where more than 5% of the area has an optical depth to infinity of less than unity. The radiation pressure gradient now spans five orders of magnitude, comparable to the variations in density. The two are now highly correlated, while the radiative flux has become nearly constant, and is approaching the free-streaming radiative flux, $F_\mathrm{r} \sim E_\mathrm{r} c$ due to the low optical depths. The densest cells are still highly correlated with F_r, however once the radiative flux approaches the free streaming limit, it is no longer correlated with density. Though the opacity and temperature are varying substantially compared to interior radii, they are still nearly

constant when compared to density, radiative flux, and the radiation pressure gradient. Fluctuations no longer strongly follow log-normal distributions. This is likely due to the nature of convection changing. Fluctuations are no longer nearly isotropic, but rather dominated by large, hot, and dense plumes pushing upwards and cool diffuse plasma moving down. We believe this region to encompass the variable, dynamic surface of these envelopes. The explicit nature of this regions and the convective transport in both regions will be explored further in future work. However, as shown by the gray-dotted line in Figure 2.3, distributions of both density and radiative flux variations are still close to log-normal, so we assume both quantities follow log-normal distributions throughout the optically thick regions of these envelope models in order to quantify their variance.

At all radii, temperature and opacity are relatively constant when compared to radiative flux and density and will be treated as such for the remainder of this work, i.e. $\kappa(r) = \langle\kappa(r)\rangle$ and $T(r) = \langle T(r)\rangle$. Including the variations only complicates the analysis and does not have a substantial effect on the resulting prescription. The extreme variations in density and radiative flux throughout the stellar envelope combined with their strong inverse correlation strongly modify the radiation pressure gradient, which will be discussed in detail in § 2.2.

2.1.3 Pseudo-Mach Number Definition and Value

Ideally, a single, local parameter would quantify the large variations caused by the turbulent motion. In the classical model of MLT for gas pressure dominated regimes, a

turbulent Mach number proves a good choice for an independent variable. However, our models are radiation pressure dominated so a new definition is needed. Our heuristic choice is motivated by the work of Jiang et al. (2015) and defines a local advective velocity, v_L, with which the radiative energy density would be carried to account for the entire luminosity, L,

$$v_{\rm L}(r) \equiv \frac{L}{4\pi r^2 a T^4(r)}, \tag{2.5}$$

where a is the radiation constant, and r and T are the local radius and temperature. To convert this advective velocity to a dimensionless number, we divide by the isothermal gas sound speed, $c_{\rm s} = \sqrt{P_{\rm gas}/\rho} = \sqrt{k_{\rm B}T/\mu m_{\rm p}}$, to create a pseudo-Mach number, $\mathcal{M}_\Psi$,

$$\mathcal{M}_\Psi(r) \equiv \frac{v_{\rm L}(r)}{c_{\rm s}(r)} = \frac{L}{4\pi a r^2 T^{4.5}(r)} \left(\frac{\mu m_{\rm p}}{k_{\rm B}}\right)^{1/2}, \tag{2.6}$$

where μ is the mean molecular weight, k_B is the Boltzmann constant, and m_p is the mass of a proton. The choice of the isothermal gas sound speed arises because the largest fluctuations occur in regions where $\tau \ll \tau_{\rm c}$ implying photons are leaking out of fluid parcels rather than supporting them against compression (Jiang et al., 2015). This leaking forces the gas pressure to be the only post-shock support, and thus the isothermal gas sound speed is a good choice for characterizing the amplitude of density fluctuations. Despite the factor of $T^{-4.5}$, the fluctuations of $\mathcal{M}_\Psi$ are still substantially smaller than those of density or radiative flux.

Figure 2.4 shows $\mathcal{M}_\Psi(r)$ for our 3D models, using $T(r) = \langle T(r) \rangle$. Despite the wide variance in radial extent, all models cover similar ranges of $\mathcal{M}_\Psi$. Additionally, each model shows two slope changes. Deep in the envelope (around $\mathcal{M}_\Psi \sim 5$), the turbulent

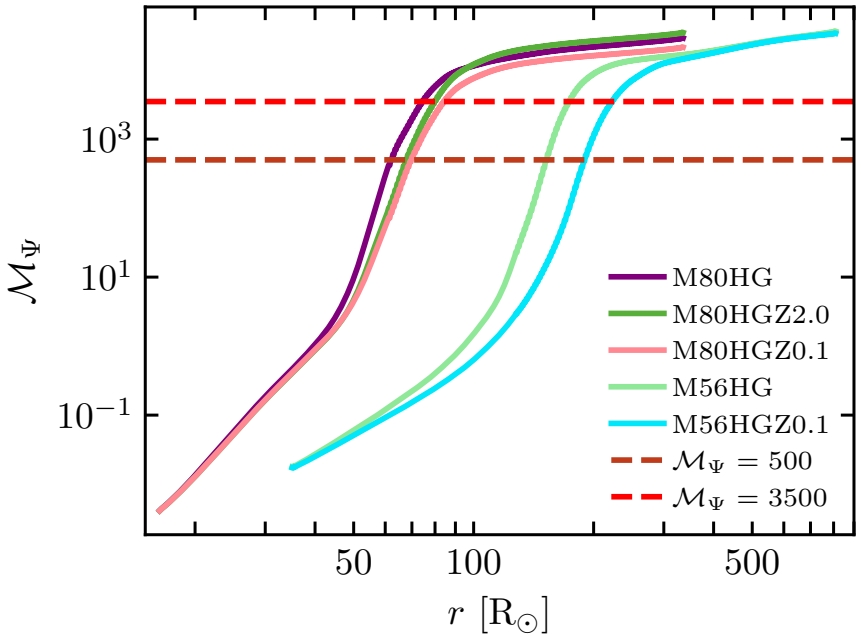

Figure 2.4: Pseudo-Mach number as a function of radius for a single snapshot of all models considered. The horizontal dashed lines correspond to $\mathcal{M}_\Psi = 500$ (dark red) and $\mathcal{M}_\Psi = 3500$ (bright red).

convection begins to carry a flux comparable to radiative diffusion above the iron opacity peak causing a change in the temperature gradient and giving rise to a change in the gradient of $\mathcal{M}_\Psi$. Near the surface (around $\mathcal{M}_\Psi \sim 10^4$), the optical depth drops below unity and the radiation freely streams, causing a second change in the gradient. Both gradient changes occur at different radial locations in all the models, however each occurs at a similar value of $\mathcal{M}_\Psi$. As $\mathcal{M}_\Psi$ is a more universal value than radius for diagnosing the level of fluctuation, it will be solely used for the remainder of this work. The $\mathcal{M}_\Psi$ values of the red horizontal lines in Figure 2.4 are chosen to match the same colored lines in earlier figures.

Figure 2.5 shows the cumulative distribution of the radial area fraction with τ less than a given value at four chosen values of $\mathcal{M}_\Psi$, all above the iron opacity peak. The three distributions plotted are generated from 2800 snapshots ($\approx$ 15 days) of model M56HG (dashed lines), 2800 snapshots ($\approx$ 15 days) of model M80HG (dotted lines), and the sum of the two, a 5600 snapshot sample (solid lines). These snapshots were chosen to encompass the full range of luminosity variations observed in both models. For both models considered, roughly 20% of the area at radii where $\mathcal{M}_\Psi = 3500$ and 5% of the area where $\mathcal{M}_\Psi = 500$ have optical depths to infinity of less than 1. These match the previously plotted red lines in Figures 2.1 and 2.2. Looking at the distributions themselves, the locations with $\mathcal{M}_\Psi = 3500$ are not optically thick as the τ distribution rises sharply after $\tau = 1$ and has 85% of area with $\tau < 10$. The distributions corresponding to locations where $\mathcal{M}_\Psi = 500$ are less extreme with shallower slopes and only 50% of area

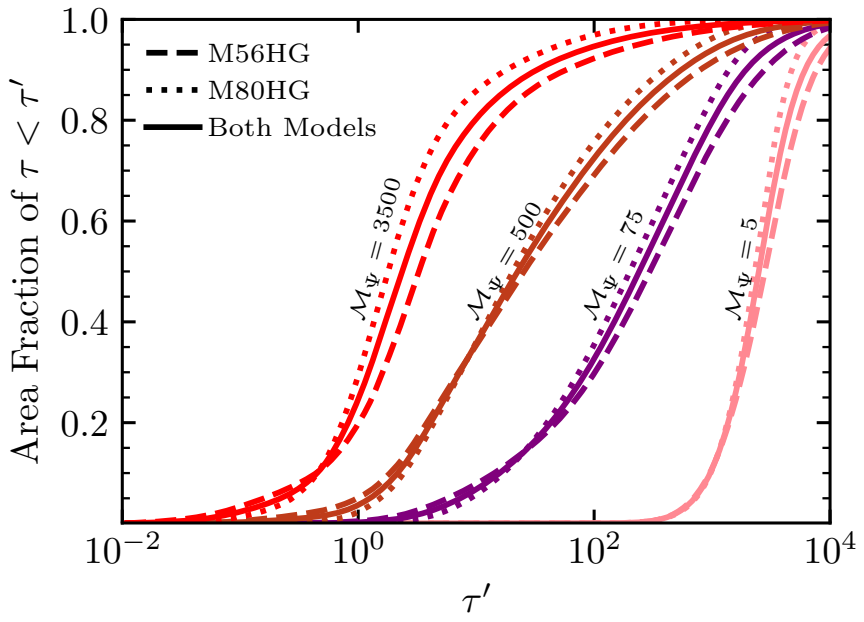

Figure 2.5: Normalized cumulative sum of distributions of τ at four values of $\mathcal{M}_\Psi$. Colors represent different choices of $\mathcal{M}_\Psi$ and are labeled adjacently. Line styles correspond to τ distributions from different 3D models, M56HG, and M80HG. Both models, consisting of the time average of 2800 snapshots, are combined and averaged to create a sample of 5600 snapshots shown by the solid line.

having $\tau < 10$. Despite the two models having different core masses, luminosities, radial extents, and effective temperatures, the optical depth distributions are very similar at locations with equal $\mathcal{M}_\Psi$ values, confirming the selection of $\mathcal{M}_\Psi$ as a good choice for an independent variable. It also provides an additional criterion for when the model starts to become optically thin.

2.1.4 Variance and Covariance of Density and Radiative Flux

The density and radiative flux follow log-normal distributions for the majority of the optically thick region of our models. As they are highly inversely correlated and affect the radiation pressure gradient (and hence the structure of the envelopes themselves) it is important to quantitatively characterize their standard deviations and covariance. Figure 2.6 shows the distributions of the standard deviations of $\ln(\rho)$, $\sigma_{\ln(\rho)}$, and $\ln(F_\mathrm{r})$, $\sigma_{\ln(F_\mathrm{r})}$, as well as their covariance, $\sigma_{\ln(F_\mathrm{r}),\ln(\rho)}$, as functions of $\mathcal{M}_\Psi$.

The color represents the probability of observing a given value for the standard deviation or covariance at a certain $\mathcal{M}_\Psi$, calculated from 5600 snapshots spanning ≈ 15 days of two models (2800 from M56HG and 2800 from T19L6.2). For all quantities, the values are very constrained despite the large variety of stellar models. Though two distributions can be distinguished at $\mathcal{M}_\Psi \lesssim 10$, one from each model used, the distinction is neglected and we consider each variance to follow a single distribution over all values of $\mathcal{M}_\Psi$.

The light purple-dashed lines represent the mean of the colored distributions. The mean standard deviations of both $\ln(\rho)$ and $\ln(F_\mathrm{r})$, as well as the mean of their covariance,

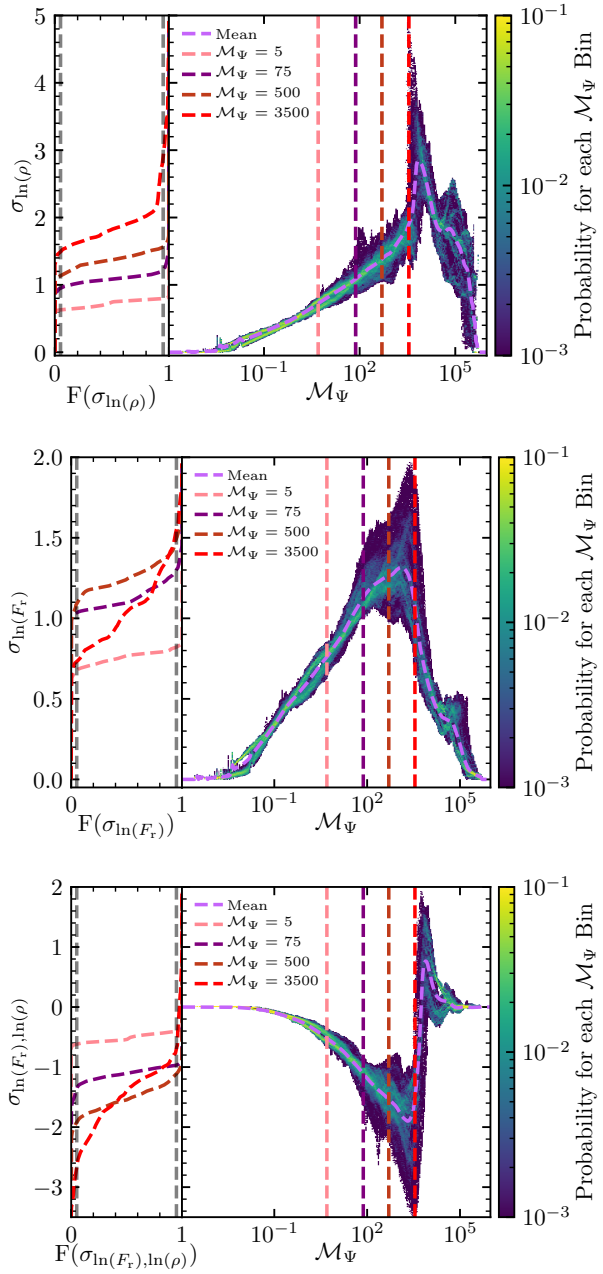

Figure 2.6: Standard deviation of $\ln(\rho)$ (top), and $\ln(F_r)$ (middle) , and the covariance of $\ln(\rho)$ and $\ln(F_r)$ (bottom) as a function of $\mathcal{M}_\Psi$. The right panel of each figure shows the distribution of the quantity as a function of $\mathcal{M}_\Psi$ where the color represents the probability of each value for each $\mathcal{M}_\Psi$ bin. These distributions are generated from 5600 3D snapshots, 2800 from model M56HG and 2800 from model M80HG. The light purple-dashed line represents the mean of the distributions. The left panel shows the cumulative distribution function, $F(\sigma)$, of the quantity at chosen $\mathcal{M}_\Psi$ values, $\mathcal{M}_\Psi = 5$, 75, 500, and 3500 (pink, purple, dark red, and bright red respectively). The dashed, vertical gray lines show where the cumulative distribution is 5% and 95%.

correspond to variations in ρ and $F_{\rm r}$ larger than a factor of 2 at $\mathcal{M}_\Psi = 10$. Moving outwards, the sound speed decreases, increasing the strength of the turbulent motion and thus increasing the variations to a factor of 4 at $\mathcal{M}_\Psi = 500$ where an optically thick assumption, like that used in Equation 2.3, begins to degrade. At $\mathcal{M}_\Psi > 500$, the distributions of density and flux at fixed $\mathcal{M}_\Psi$ start to deviate from log-normal and so despite the standard deviation of $\ln(\rho)$ and covariance approaching expected values (corresponding to factors of 10) these estimations should be taken less quantitatively. In the optically thin region of the models, $\mathcal{M}_\Psi > 3500$, the fluctuations cannot be described by a single log-normal distribution. The characteristics of this region are strongly affected by the wind dynamics and are significantly time dependent which, combined with the fluctuations of the distributions from log-normal in shape, cause the lack of a clear expected value for the standard deviations and covariance. The physics of this region is beyond the scope of this work.

The left panel of each plot shows the cumulative distribution functions, $F(\sigma_{\ln(x)})$, of the standard deviation or covariance at the values of $\mathcal{M}_\Psi$ specified by the colored vertical dashed lines in the right panels. The cumulative distribution functions are defined as,

$$F(\sigma_{\ln(x)}) = \int_0^{\sigma_{\ln(x)}} p(\sigma'_{\ln(x)}) d\sigma'_{\ln(x)}, \tag{2.7}$$

where $p(\sigma'_{\ln(x)})$ is the probability density for that value of $\sigma'_{\ln(x)}$ at that value of pseudo-Mach number. The vertical gray-dashed lines in the left panels show the 90% confidence intervals for the means. The cumulative distribution functions quantify the distributions that are shown qualitatively with color in the right panels, especially the low probability

regions, shown in dark purple. Though these excursions are large at high $\mathcal{M}_\Psi$, such as $\mathcal{M}_\Psi = 3500$, the majority of the probability lies in the central part of the distributions. Typically the 90% confidence intervals span ± 0.5, with higher values of $\mathcal{M}_\Psi$'s having intervals of ± 1 relative to the mean value.

In previous literature (e.g. Owocki & Sundqvist, 2018), density fluctuations occurring in turbulent media, typically clumpy stellar winds, are often characterized by the amplitude of over-densities, defined by $\frac{\langle \rho^2 \rangle}{\langle \rho \rangle^2}$. This definition of clumping is simply related to the standard deviation in the natural log of density, $\sigma_{\ln(\rho)}$. For log-normal distributions, it can be shown that $\ln(\langle \rho \rangle) = \langle \ln(\rho) \rangle + \frac{\sigma^2_{\ln(\rho)}}{2}$ and $\ln(\langle \rho^2 \rangle) = 2\langle \ln(\rho) \rangle + 2\sigma^2_{\ln(\rho)}$. Substituting these equation for the typical definition of over-densities in turbulent media yields,

$$\sigma^2_{\ln(\rho)} = \ln\left(\frac{\langle \rho^2 \rangle}{\langle \rho \rangle^2}\right). \tag{2.8}$$

Hence squaring the distributions in the top panel of Figure 2.6 reveals of the over-densities, or clumping factors, of the turbulent envelope.

2.2 Calibrating the Impact of Fluctuations on Optically Thick Transport

The 3D models exhibit a strong correlation between density and radiation pressure which we must include in 1D models. One dimensional models calculate the local radiation pressure gradient in optically thick regions, $(\nabla P_{\rm r})_{1D}$, using the diffusion equation,

$$(\nabla P_{\rm r})_{1D} = -\frac{1}{c}\langle F_{\rm r} \rangle \langle \kappa \rangle \langle \rho \rangle. \tag{2.9}$$

This approach does not include the correlations of density, radiative flux, and opacity evident in 3D models, and thus does not agree with $\nabla P_{\rm r}$ from 3D models, which will satisfy

$$(\nabla P_{\rm r})_{3D} = -\frac{1}{c}\langle F_{\rm r}\kappa\rho\rangle. \tag{2.10}$$

The opacity is nearly constant when compared to density or radiative flux and so we neglect the correlations with κ and pull the average of κ out of the main average of $\nabla P_{\rm r}$. Extracting κ from the average does not substantially affect the calculation of the radiation pressure; the relative error between $\langle\kappa\rangle\langle F_{\rm r}\rho\rangle$ and $\langle F_{\rm r}\kappa\rho\rangle$ is less than 0.1% within the range of $\mathcal{M}_\Psi$ we are interested in. The ratio of the gradient from the 3D models, $\nabla P_{\rm r}$, and the 1D prediction of Equation 2.9 then defines a new, dimensionless parameter, Ψ, that will account for the difference between the gradients,

$$\Psi \equiv \frac{\langle F_{\rm r}\rho\rangle}{\langle F_{\rm r}\rangle\langle\rho\rangle}. \tag{2.11}$$

As $F_{\rm r}$ and ρ are inversely correlated (detailed in § 2.1.2) Ψ will never exceed unity. The densest regions will have minimal radiative flux transport while the rarefied regions will have more. The largest densities are multiplied by the smallest fluxes, and vice versa, in the numerator of Equation 2.11, significantly reducing the average of the product when compared to the product of the independent averages.

By definition Ψ is invariant to the means of ρ or $F_{\rm r}$ allowing us to calculate it without using a specific model. Using the standard deviations and covariance of ρ and $F_{\rm r}$, shown in Figure 2.6, we synthesize a 2D probability distribution for density and radiative flux at each value of $\mathcal{M}_\Psi$. We generate 10^4 mock values of both ρ and $F_{\rm r}$ spanning five stan-

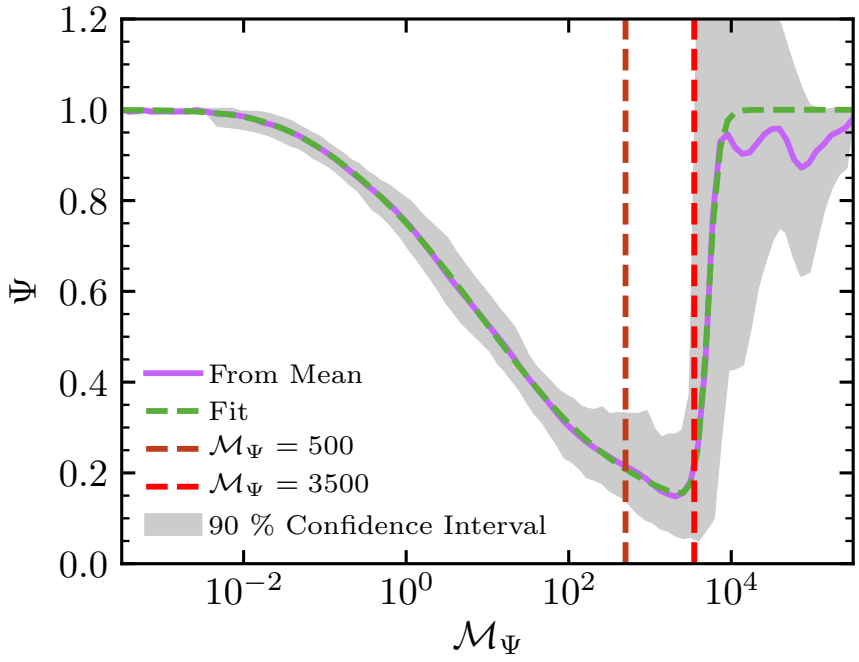

Figure 2.7: Dependence of Ψ on $\mathcal{M}_\Psi$. The light purple line represents Ψ as calculated from the mean of the variance distributions (light purple-dashed lines in Figure 2.6). The gray regions are the 90% confidence intervals from this mean. The green-dashed line follows the functional fit for Ψ given in Equation 2.12. The vertical dashed lines are at $\mathcal{M}_\Psi = 500$ (dark red) and $\mathcal{M}_\Psi = 3500$ (bright red).

dard deviations evenly in log-space. These values are collected to produce 10^8 (density, radiative flux) pairs. Using the probability of each combination as weights, we calculate the averages of density, radiative flux, and their product and thus obtain values of Ψ.

Figure 2.7 shows the calculated values of Ψ as a function of $\mathcal{M}_\Psi$. The light purple line shows the mean values and the gray region corresponds to the 90% confidence intervals around the means. The red vertical dashed lines show the region where an optically thick assumption degrades and where the variations of radiative flux and density deviate from log-normal distributions. This deviation from log-normal distributions, due to the wind playing a dominant role in the dynamics, causes the uncertainty of Ψ to substantially

increase for $\mathcal{M}_\Psi \gtrsim 3500$. Proper characterization of this region is beyond the scope of this work as we choose to focus on the radiatively diffusive region where the radiative flux closely follows the diffusion equation (Equation 2.10).

The values of Ψ become $\ll 1$ within the optically thick region, demonstrating that the 1D approximation of the radiation pressure gradient in Equation 2.9 is a substantial over-estimate for these regions. The decrease in Ψ arises from density and radiative flux fluctuations generated from the turbulence. As the sound speed decreases with radius turbulent shocks become stronger causing larger density and radiative flux contrasts further our in the envelopes, at higher $\mathcal{M}_\Psi$ values. Because the two quantities are highly anti-correlated, this reduces the average radiation pressure gradient of the 3D model, but does not substantially effect the expected values of density or radiative flux alone. The reduction in the average of the radiation pressure gradient while leaving $\langle\rho\rangle$ and $\langle F_{\rm r}\rangle$ constant gives rise to the small values of Ψ.

To simplify future calculations of $\Psi(\mathcal{M}_\Psi)$, we fit the mean values using the product of a hyperbolic tangent of $\log_{10}(\mathcal{M}_\Psi)$ and two Fermi functions. The resulting formula is given by

$$\begin{aligned}\Psi(\mathcal{M}_\Psi) \approx 1+\Bigg\{ &\Big(A\tanh\left(B\log_{10}(\mathcal{M}_\Psi)+C\right)+D\Big)\times \\ &f_{\rm Fermi}(-\log_{10}(\mathcal{M}_\Psi), F_{1A}, F_{1B})\times \\ &f_{\rm Fermi}(\log_{10}(\mathcal{M}_\Psi), F_{2A}, F_{2B})\Bigg\} \\ \text{where } f_{\rm Fermi}(x, F_A, F_B) &= \frac{1}{\exp\left(\frac{x+F_A}{F_B}\right)+1},\end{aligned} \tag{2.12}$$

and the fit coefficients are: $A = 0.441$, $B = -0.533$, $C = 0.525$, $D = -0.473$, $F_{1A} =$

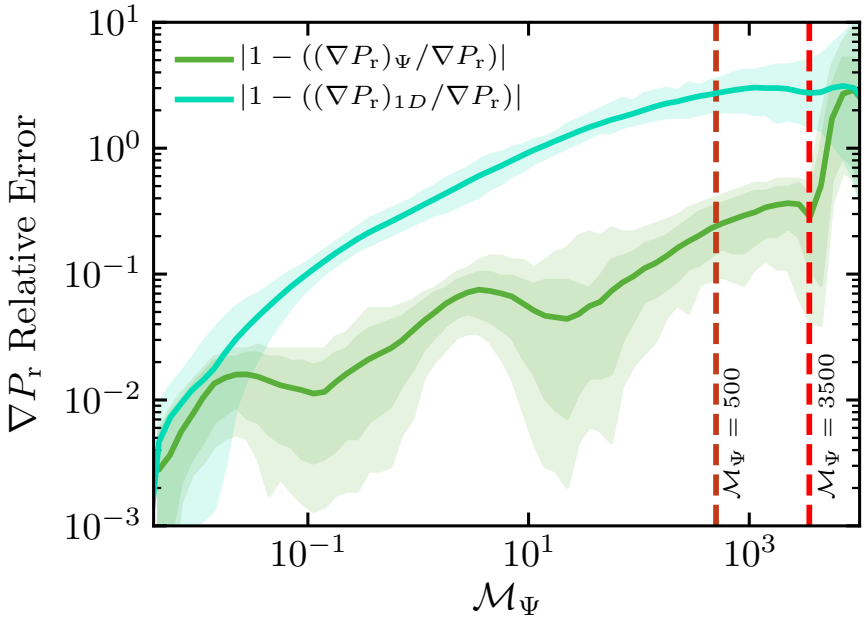

Figure 2.8: Comparison of the fractional difference between the radiation pressure gradient calculated from the 3D model, $\nabla P_{\rm r}$, the 1D approximation, $(\nabla P_{\rm r})_{1D}$ (cyan), and the corrected $(\nabla P_{\rm r})_\Psi$ (green). The two distributions are generated using the same 5600 snapshots used to generate the distributions in Figure 2.6. The solid lines show the means and the shaded regions represent the 70% (darker) and 90% (lighter) confidence intervals. For the relative error of $(\nabla P_{\rm r})_{1D}$, only the 90% confidence interval is plotted for clarity. The vertical dashed lines are at $\mathcal{M}_\Psi = 500$ (dark red) and $\mathcal{M}_\Psi = 3500$ (bright red).

-1.451, $F_{1B} = 0.465$, $F_{2A} = -3.715$, $F_{2B} = 0.067$. This fitting function is shown by the green-dashed line in Figure 2.7. Because of the large uncertainties and many of our assumptions breaking down, we have chosen to generate a fitting function that defaults to no modification to previous $(\nabla P_{\rm r})_{\rm 1D}$ calculation methods at large values of $\mathcal{M}_\Psi$. We understand that this choice may cause some difficulties when implemented in current 1D models and hence provide an alternative in § 2.3.

To account for the correlation of radiative flux and density in the calculation of the 1D radiation pressure gradient in optically thick regions, we simply multiply $(\nabla P_{\rm r})_{1D}$ by

Ψ to get $(\nabla P_{\rm r})_\Psi$ or,

$$(\nabla P_{\rm r})_\Psi \equiv -\frac{1}{c}\langle F_{\rm r}\rangle\langle\kappa\rangle\langle\rho\rangle\Psi. \tag{2.13}$$

This correction is only modifying the 1D radiation pressure gradient in optically thick regions. Until corrections accounting for turbulent pressure and the heat carried by convection are also incorporated, this definition of the radiation pressure gradient should not be implemented in a 1D stellar evolution code. Characterizing turbulent pressure and the resulting convective flux will be addressed in future work.

Figure 2.8 shows the relative error between the averaged 3D radiation pressure gradient, $\nabla P_{\rm r}$, the 1D approximation, $(\nabla P_{\rm r})_{1D}$ (cyan), and the corrected $(\nabla P_{\rm r})_\Psi$ (green), for all 5600 snapshots used to estimate the standard deviations and covariance of $\ln(\rho)$ and $\ln(F_{\rm r})$ (see § 2.1.4). The lines represent the mean and the shaded regions represent 70% (darker) and 90% (lighter) confidence intervals. The fitting formula given in Equation 2.12 determines values of Ψ used for the calculation of $(\nabla P_{\rm r})_\Psi$. The two distributions of relative error overlap for $\mathcal{M}_\Psi \lesssim 10^{-2}$ where turbulent convection is not important and there is little variation in density and radiative flux. However, at higher $\mathcal{M}_\Psi$ values the relative errors differ substantially. At $\mathcal{M}_\Psi = 10$, $(\nabla P_{\rm r})_{1D}$ has a relative error of 100%, or a factor of 2 difference, while $(\nabla P_{\rm r})_\Psi$ only differs by 5%. At $\mathcal{M}_\Psi = 500$ (dark red-dashed line), where 5% of the area has $\tau < 1$, $(\nabla P_{\rm r})_{1D}$ differs from $\nabla P_{\rm r}$ by nearly 300%, while $(\nabla P_{\rm r})_\Psi$ differs by only 22%. The addition of Ψ in the 1D approximation for the radiation pressure gradient results in an order of magnitude correction in relative error. Above $\mathcal{M}_\Psi = 3500$ (bright red-dashed line), $(\nabla P_{\rm r})_\Psi$ quickly approaches the same

relative error as $(\nabla P_{\rm r})_{1D}$. This is due to the fluctuations of radiative flux and density deviating from log-normal distributions. The transition of the probability distribution functions begins near $\mathcal{M}_\Psi = 500$ (dark red vertical dashed line), and though the relative error of our new radiation pressure gradient prescription is promising when compared to the previous method, we caution the use of $(\nabla P_{\rm r})_\Psi$ above $\mathcal{M}_\Psi = 500$. Because of the sharp increase in the relative error of $(\nabla P_{\rm r})_\Psi$, we recommend $\mathcal{M}_\Psi = 3500$ as the strict upper limit to the range of $\mathcal{M}_\Psi$ over which $(\nabla P_{\rm r})_\Psi$ is an accurate approximation.

Implementing the same methods used to make Figure 2.8, we now compare the relative error of 1D approximations to the radiation pressure gradient with and without our Ψ parameter for the four envelope models listed in Table 2.1 that were not used to generate Ψ. Figure 2.9 shows the mean of each distribution generated using over 1000 snapshots ($>$ 5 days) for each model. These ranges of snapshots were chosen to encompass the majority of luminosity variations in the steady-state regions of these models. These models are completely independent of those used in the fitting of our Ψ parameter, making this a test of our modeling approach. As will be shown in future work, changes in metallicity affect the strength of the opacity peaks, and modify the turbulence resulting in different envelope structures. Because of these differences, comparing our prescription for the radiative pressure gradient in these models against the 3D results represents a test of our proposed method.

Deep in the models, the variance of density and radiative flux are small and so the difference is negligible, though the gradient estimate is improved with the addition of Ψ.

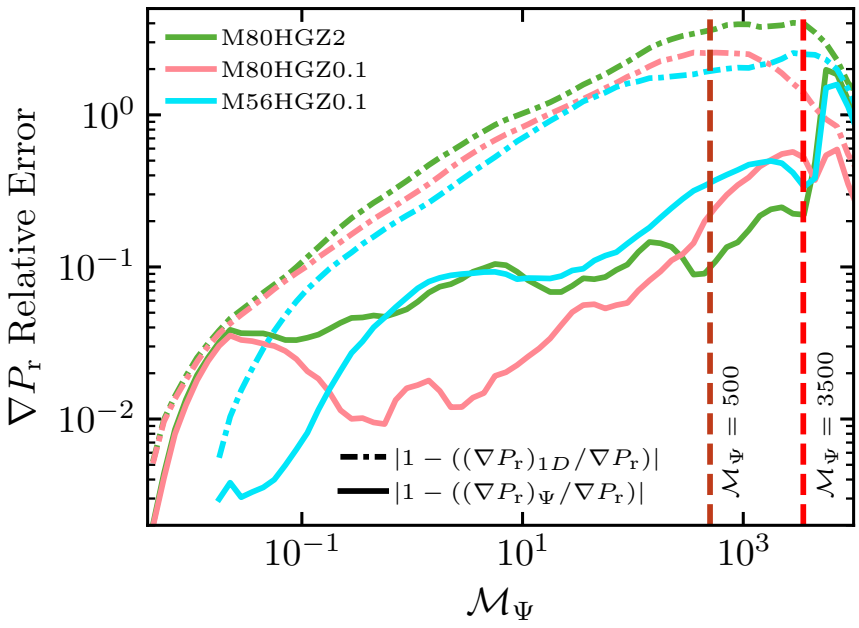

Figure 2.9: Comparison of the fractional difference between the radiation pressure gradient calculated from the 3D model, $\nabla P_{\rm r}$, the 1D approximation, $(\nabla P_{\rm r})_{1D}$ (dot-dashed), and the corrected 1D prescription, $(\nabla P_{\rm r})_{\Psi}$ (solid) for models not used to generate Ψ. Each line represents the mean of a distribution generated using more than 1000 snapshots (> 5 days of simulation time) from each model. The models employ the same color coding as Figure 2.4. The confidence intervals for each line are not plotted for clarity, but are similar to those shown in Figure 2.8. The vertical dashed lines are at $\mathcal{M}_\Psi = 500$ (dark red) and $\mathcal{M}_\Psi = 3500$ (bright red).

In all the models, the 1D radiation pressure gradient begins to diverge from the 3D results at the onset of the iron opacity peak, with the prescription including Ψ staying closer to the 3D result. In all the models, when the 1D approximation $(\nabla P_{\rm r})_{\rm 1D}$ reaches a relative error of 100%, the 1D estimate including Ψ has a relative error of $\lesssim 10\%$. Our prescription reaches a maximal relative error of $\approx 60\%$, though this occurs above $\mathcal{M}_\Psi = 500$ where the optically thick assumption and log-normal characterizations begin to break down. At $\mathcal{M}_\Psi = 500$ the radiative pressure gradient prescription with Ψ included has a relative error of 40% or less, considerably lower than the $> 100\%$ of the uncorrected formula. Again $\mathcal{M}_\Psi \approx 3500$ appears to be the limit above which our prescription for Ψ starts to fail. However, in this regions of higher $\mathcal{M}_\Psi$ our prescription still outperforms the approximation without Ψ.

2.3 Domain of Applicability in 1D Models and Future Work

Fundamentally, the turbulent convection that affects the radiation pressure gradient arises as the stellar luminosity approaches the Eddington luminosity, implying that the utilization of Ψ to correct for radiative flux and density correlations is applicable to any astrophysical situation where any opacity peak arises in a near Eddington limited, radiation pressure dominated plasma. The envelopes of all stars with masses larger than $\approx 30\,M_\odot$ fulfill these requirements and thus 1D models of stars in this mass range will

be affected by this correlation. However, simply reducing the radiation pressure gradient in a 1D model is not a full correction, as the turbulent convection exerts substantial pressure and transports a fraction of the stellar luminosity.

For this reason, we cannot yet implement our Ψ prescription in a modern 1D hydrostatic stellar evolution code. Instead, we show how substantial the impact of our new prescription would be when applied to models produced by the Modules for Experiments in Stellar Astrophysics (MESA; Paxton et al., 2011, 2013, 2015, 2018, 2019).

Using mostly default values, we only set the initial mass and metallicity of the models, as well as setting okay_to_reduce_grad_T_excess = .false. to ensure we are only using classical mixing length theory. With these settings, we modeled $35\,M_\odot$, $56\,M_\odot$, and $80\,M_\odot$ stars through their main sequence lifetimes. These initial models simply reveal the domain of applicability of our new prescription. Specifically, we looked at two types of models: hot models from the zero age main sequence (ZAMS), and cooler models from either the terminal age main sequence (TAMS) or the Hertzsprung gap (HG). From these models, we calculated the value of Ψ at each location. These Ψ profiles are plotted versus τ in Figure 2.10, and show that significant reductions in the radiation pressure gradient (small values of Ψ) are expected near the surface of all the models considered. Looking at the Ψ profiles, there are clearly two distributions; one for the hotter $T_{\rm eff}$ stars and another for the lower $T_{\rm eff}$ stars (see inset HR diagram of Figure 2.10). This is due to a difference in both the location, shown by the two black arrows, and shape of their iron opacity peaks. The lower $T_{\rm eff}$ models have a deeper iron opacity peak along with a steeper

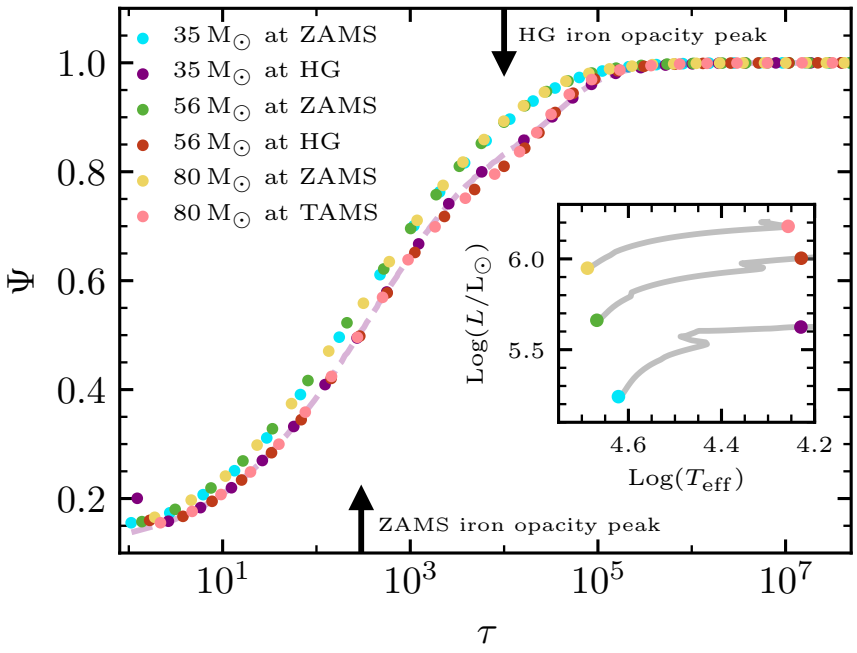

Figure 2.10: Profiles of Ψ versus optical depth for higher and lower $T_{\rm eff}$ models of $35\,M_\odot$, $56\,M_\odot$, and $80\,M_\odot$ solar metallicity stars. The points show the expected values of Ψ for each model using Equation 2.12 but do not represent the resolution of the models; rather they are spaced for clarity of viewing all profiles present. The profiles are smooth between the plotted points. The light purple dashed line shows the full profile associated with the purple points using an alternative definition of Ψ given by Equation 2.14. All Ψ values are calculated in post-processing, after the models have been calculated. The black arrows indicated the location of the peak of the iron opacity peak for the hotter $T_{\rm eff}$, zero age main sequence (ZAMS) profiles (bottom) as well as the cooler, Hertzsprung gap (HG) and terminal age main sequence (TAMS) profiles (top). Inset is a Hertsprung-Russell diagram of the MESA models' stellar evolution. The gray lines show the stellar tracks. The colored points correspond to the luminosity, L, and effective temperature, $T_{\rm eff}$, of the models with Ψ profiles plotted.

rise of the peak, starting at $\tau \approx 10^5$. This steep rise causes the initial sharper decrease in Ψ at $\tau \approx 10^4$. The higher $T_{\rm eff}$ models have the iron opacity peak substantially closer to the surface and a much shallower rise, starting as deep as $\tau \approx 5 \times 10^4$ and peaking at $\tau \approx 300$. In all the profiles, our prescription would recommend reducing the radiation pressure gradient by over 80% at the surface. The inclusion of this prescription will have profound effect on the temperature gradient, changing the nature of convection in these 1D envelopes and substantially affecting the evolution of these models in the HR diagram.

Looking at the purple points in Figure 2.10, we notice an upturn near $\tau \approx 1$ as a result from our choice of convention when generating Equation 2.12. As this upturn occurs quickly and near the surface of the models, it may cause some undesirable effects when implemented in 1D models. It could potentially require stricter surface boundary conditions as well as higher resolutions to resolve the large slope change accurately. Because the upturn in Ψ is likely a product of poorly constrained approximations in this region, we suggest an alternative fitting equation that will alleviate these problem. The generate the new formula, we remove the second Fermi function from Equation 2.12:

$$\Psi(\mathcal{M}_\Psi) \approx 1 + \Bigg\{ \Big(A \tanh\left(B \log_{10}(\mathcal{M}_\Psi) + C\right) + D \Big) \times f_{\rm Fermi}(-\log_{10}(\mathcal{M}_\Psi), F_{1A}, F_{1B}) \Bigg\} \tag{2.14}$$

where the constants are the same as those in Equation 2.12. The resulting Ψ profile is shown by the light purple line in Figure 2.10 and can be directly compared to the purple points. The removal of the second Fermi function does not affect the majority of the

profile, however near the surface of the model the slope does not change sign. Instead, the new fitting function of Ψ approaches ≈ 0.1 at $\mathcal{M}_\Psi \approx 10^6$. We are not claiming either Equation 2.12 or Equation 2.14 will work well in this region ($\mathcal{M}_\Psi \gtrsim 3500$); we are only suggesting Equation 2.14 might allow 1D models to converge more easily.

2.4 Conclusion

We quantified the large density and radiative flux fluctuations and their induced modification to the radiative pressure gradient needed to carry a certain radiative luminosity in optically thick massive star envelopes. As seen in the recent 3D models of Jiang et al. (2018), turbulent velocities drive shocks and very large density and radiative flux fluctuations (see Figure 2.2) that substantially modify the nature of radiative transport even at $\tau \gg 10$. We showed that the density and radiative flux follow log-normal distributions throughout the optically thick region of our models allowing us to accurately quantify their variations by a pseudo-Mach number, $\mathcal{M}_\Psi$. We showed that we can successfully quantify the variance and covariance of ρ and F_r with this single number at every location in thousands of snapshots from two distinct 3D models. The choice of $\mathcal{M}_\Psi$ arose from comparing the convective velocity needed to carry the heat to the isothermal gas sound speed. The isothermal gas sound speed was used because, in the regions of large density fluctuations, the optical depth is low enough the photons cannot prevent the gas from compressing, leaving the gas pressure as the only support. After quantifying the fluctuations and their correlations as a function of $\mathcal{M}_\Psi$, we derived an effective 1D im-

plementation that yields $\lesssim 30\%$ agreement with the 3D $\nabla P_{\rm r}$ in optically thick regions of the models. This prescription is described by a local quantity, $\mathcal{M}_\Psi(L, T, r)$, and a fitting formula, Equation 2.12, that will allow simple incorporation into future 1D models.[1]

[1]Our fitting formula should only be trusted for $\mathcal{M}_\Psi < 3500$.

Chapter 3

The Impact of Turbulence on Stellar Structure

The 3D NSCZs show significant fluctuations in density (ρ) and radiative flux ($F_{\rm r}$) that reduce the radiation pressure support as a result of porosity (Schultz et al., 2020). These density fluctuations also combine with trans-sonic velocities and propagate through the stellar photosphere to produce an optically thick wind in sufficiently high L models (Jiang et al., 2015, 2018). As the plumes become optically thin near the photosphere, they impart significant Doppler broadening on the escaping photons, naturally generating the long-observed microturbulence measured in spectral line widths of massive stars (Cantiello et al., 2009; Schultz et al., 2023). The 3D surface convection also generates stellar brightness variability with amplitudes and frequencies (Schultz et al., 2022) similar to observed massive stars (Bowman et al., 2020) in recent photometric surveys (e.g.

TESS, Ricker et al., 2015) confirming 1D analyses (Cantiello et al., 2021).

In this chapter, we utilize the variety in the optical depth at the Fe opacity peak ($\tau_{\rm Fe}$) in our `Athena++` simulation suite to elucidate the diversity of 3D convection from regimes where energy is transported via convection to the more "lossy" realm where radiative energy transport dominates even though convection is vigorous. As discussed in Ch. 1, when $\tau_{\rm Fe} \ll \tau_{\rm crit}$, convective plumes lose heat from radiative diffusion as they travel upwards causing a reduction in convective efficiency, and a smaller convective flux. For massive main sequence and Hertzsprung Gap stars, $\tau_{\rm crit} \gtrsim 1000$, allowing radiatively leaky NSCZs to exist inside an optically thick envelope. Such a realm of convection is implicitly included in the early works of Henyey et al. (1965); Ludwig et al. (1999); Kuhfuss (1986), and those early estimates of the impact of the radiative losses guided our exploration.

Our focus here is two fold. First, we exhibit that for models where convective transport dominates, the trans-sonic velocities apply a significant pressure, $P_{\rm turb} \propto \rho v_{\rm c}^2$, that affects the outer envelope structure much like that seen in 3D models of red supergiants (e.g. Goldberg et al., 2022). The temperature profiles in these 3D models can then be well explained (and predicted) by incorporating the impact of turbulent pressure using the Henyey et al. (1965) model. Secondly, for hotter massive stars on the main sequence, the effects of turbulent pressure are much less (e.g. Grassitelli et al., 2015). However, these 3D RHD models exhibit convective motions far outside of the regions conventionally defined by 1D models and have detectable photometric variability.

3.1 Hydrostatic Balance in 3D Models of Turbulent Envelopes

Five 3D RHD `Athena++` solar metallicity stellar envelope models were run to steady-state equilibrium, defined by reaching thermal equilibrium beneath the FeCZ. Table 3.1 details relevant quantities with the model names denoted by the core mass and phase of evolution: zero-age, middle of, and terminal age main sequence (ZAMS, MMS, TAMS respectively), and Hertzsprung Gap (HG). The new model, M13TAMS, consists of a narrow wedge spanning > 20 scale heights in both angular directions and a radial range that includes both the radiative region of the envelope below the convection zones and the regions beyond the photosphere. Figure 3.1 shows the location in the HR diagram of these models relative to MESA (Modules for Experiments in Stellar Astrophysics; Paxton et al., 2011, 2013, 2015, 2018, 2019; Jermyn et al., 2023) tracks.

Schultz et al. (2020) showed that these 3D RHD models exhibit correlations that reduce the radiation pressure support, motivating our investigation of hydrostatic balance. To quantify hydrostatic balance, the relative deviations, $(\rho g + dP/dr)/\rho g$ are plotted in Figure 3.2 using different choices for the pressure support. The x-axis is the pseudo-Mach number defined in Schultz et al. (2020) and increases outwards monotonically.

Models M13TAMS and M35ZAMS are in hydrostatic balance with $P = \langle P_{\rm therm} \rangle_V$, deviating by less than 5% throughout their envelopes. For the other three models, however, hydrostatic balance fails with M35MMS, M80HG, and M56HG reaching upwards of

Table 3.1: 3D Model Properties

Model Name	Masses		Temperature		Luminosities		Angular Size
	$M_{\rm core}$	$M_{\rm env}$	$T_{{\rm eff},F}$ [a]	$T_{\rm eff}$ [b]	L	$\Gamma_{\rm Edd,\,Fe}$ [c]	$\Omega_{\rm sim}$
	($\rm M_\odot$)	($\rm M_\odot$)	(10^3 K)	(10^3 K)	($\log(L/\rm L_\odot)$)		
M35ZAMS [1]	35	0.004	42	42	5.2	0.82	0.0013
M35MMS [2]	35	0.027	34	37	5.4	0.97	0.04
M13TAMS	13	0.019	25	27	4.4	0.55	0.0096
M80HG [3]	80	0.032	26	20	6.4	3.23	1.41
M56HG [4]	56	0.036	15	9	6.2	3.38	1.41

Model Name	Optical Depth		MESA Velocities		3D RMS Velocities		
	$\tau_{\rm Fe}$	$\frac{\tau_{\rm Fe}}{\tau_{\rm crit}}$	$v_{\rm MESA,Fe}$	$v_{\rm MESA,He}$	$v_{\rm Fe}$	$v_{\rm He}$	v_F
			($\rm km\,s^{-1}$)	($\rm km\,s^{-1}$)	($\rm km\,s^{-1}$)	($\rm km\,s^{-1}$)	($\rm km\,s^{-1}$)
M35ZAMS [1]	515	0.02	20	0	6.2	8.0	8.9
M35MMS [2]	1,084	0.25	44	0	57	145	148
M13TAMS	3,487	0.24	11	0.01	8.3	12	19
M80HG [3]	4,300	2.3	-	-	145	170	166
M56HG [4]	25,686	8.1	-	-	81	132	161

Model Name	Scale Heights			
	$H_{\rm Fe}$	H_F	$H_{\rm tot,Fe}$	$H_{{\rm tot},F}$
	($\rm R_\odot$)	($\rm R_\odot$	($\rm R_\odot$)	($\rm R_\odot$)
M35ZAMS [1]	0.07	0.01	0.07	0.01
M35MMS [2]	0.25	0.09	0.28	0.13
M13TAMS	0.11	0.02	0.11	0.02
M80HG [3]	3.99	2.58	5.74	8.36
M56HG [4]	13.34	4.83	16.45	31.12

[a] Defined as the average temperature at the radius, r, that satisfies $L/4\pi r^2 = \sigma T_{{\rm eff},F}^4$.

[b] Defined as the average temperature at the location where $\langle\tau\rangle = 1$.

[c] Eddington ratio at the Fe opacity peak.

[1] Model T42L5.0 in Schultz et al. (2022, 2023).

[2] Model T32L5.2 in Schultz et al. (2022) and T35L5.2 in Schultz et al. (2023).

[3] Model T19L6.4 in Jiang et al. (2018); Schultz et al. (2020, 2023).

[4] Model T9L6.2 in Jiang et al. (2018); Schultz et al. (2020).

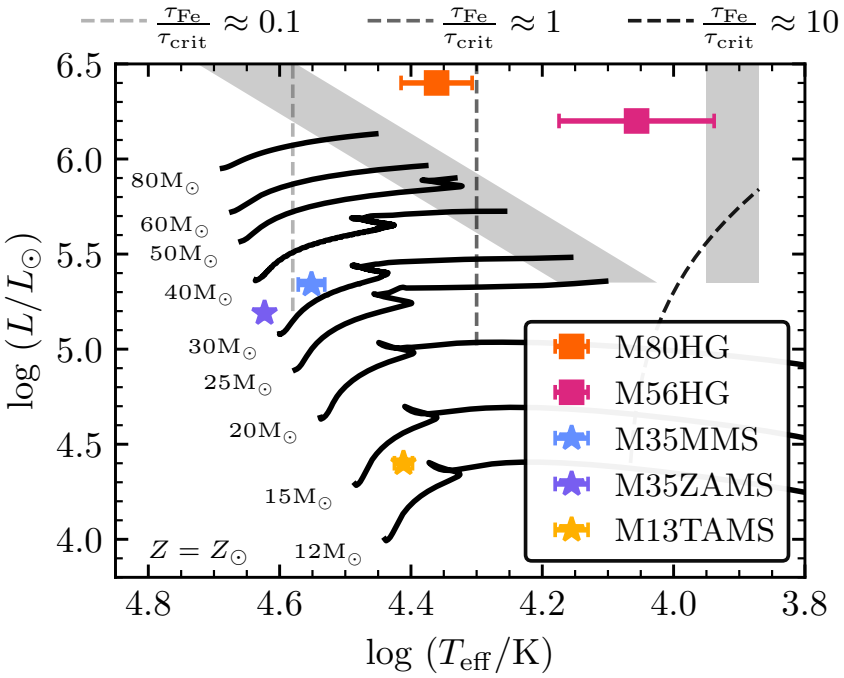

Figure 3.1: HR diagram showing the five 3D models (colored points). Squares represent models from Jiang et al. (2018) while the stars denote models from Schultz et al. (2022) and this work. The errorbars show the difference between definitions of $T_{\rm eff}$ described in § 3.2.1. The black lines are MESA models from Cantiello et al. (2021). The vertical dashed lines are approximate contours of $\tau_{\rm Fe}/\tau_{\rm crit}$ as calculated from the MESA models. Gray shaded regions show the S Dor and LBV outburst instability strips from Smith et al. (2004).

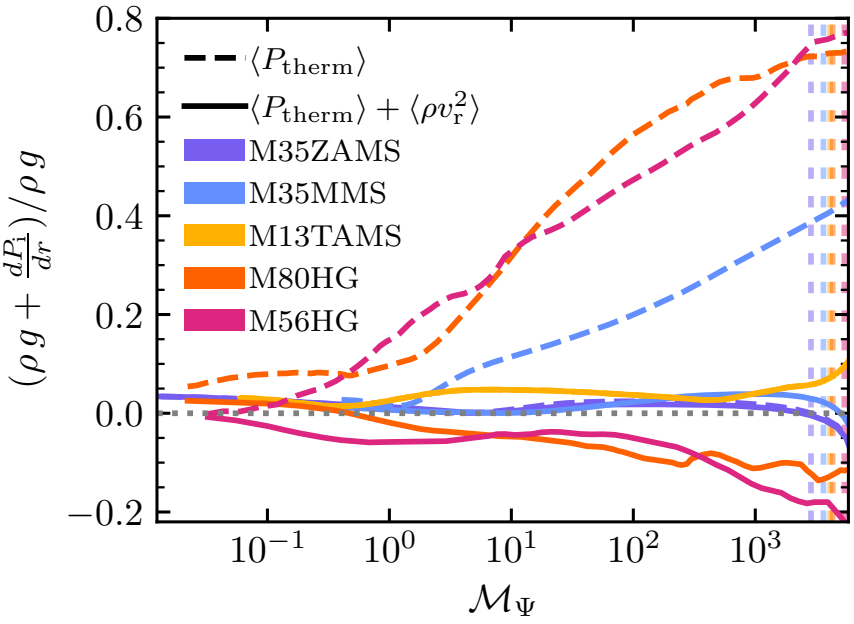

Figure 3.2: Fractional difference from hydrostatic balance for the average pressure of 3D models versus $\mathcal{M}_\Psi$ including and excluding turbulent pressure (solid and dashed respectively). Vertical dashed lines on the right denote the location where the energy flux matches the photospheric criteria of σT^4 (e.g. $T = T_{\rm eff,\,F}$ from Table 3.1).

41%, 73%, and 77% discrepancies at their surfaces respectively. These large deviations cannot be explained by the optically thick winds of M80HG and M56HG, as the advective velocity associated with the wind mass loss is less than the turbulent velocities inside the photosphere. The positive discrepancy indicates additional pressure support is needed to reach force balance for these turbulent models.

As the RMS velocities of the turbulence approach the sound speed, turbulent pressure given by $P_{\rm turb} \equiv \langle \rho v_{\rm r}^2 \rangle_V$ provides support. The choice of the radial velocity component, $v_{\rm r}$, is motivated by expanding the radial component of the 3D spherical polar momentum equation where a $\rho v_{\rm r}^2$ term assists in balancing ρg (Goldberg et al., 2022). This additional pressure does not alter the comparison for M35ZAMS and M13TAMS as $P_{\rm turb} \ll P_{\rm therm}$

in these models. However the other three models show significant improvements in force balance when $P_{\rm turb}$ is added. The deviations of M35MMS reduce to the same 5% as the two less turbulent models. The models with significant optically thick winds only experience $< 20\%$ deviations within their photospheres, a factor of 4 improvement, and moreover, the deviations are in the expected direction. Accounting for $P_{\rm turb}$ in the luminous and massive models is required to correctly balance gravity in 1D stellar evolution models.

3.2 Comparing Averages of 3D Models to 1D Profiles

As 3D RHD models of massive star envelopes are computationally expensive, 1D models remain the most effective way to understand their evolution. However 1D models require approximations that are not always verified with physically motivated 3D models. By comparing the 1D averages of the existing 3D models we can verify the effectiveness of current 1D approximations. Spherical averages of the 3D models were calculated and compared to MESA models chosen to match their core masses and luminosities. Only the three wedge-like models (M35ZAMS, M35MMS, and M13TAMS) were able to be precisely matched as the global models (M80HG and M65H) have luminosities boosted by $\approx 50\%$, to yield faster convergence of their turbulent motions.

3.2.1 Extracting 1D Models from 3D Wedges

Distilling the turbulent 3D RHD models into 1D analogs is not as simple as using a volume weighted average. Using $\langle\rho\rangle_V$ and $\langle T\rangle_V$ to calculate the thermal pressure results in factor of 2 differences from $\langle P_{\rm therm}\rangle_V$ near the surface, motivating a reconsideration of conserved quantities when averaging 3D models to yield 1D profiles.

We chose the mass and internal energy contained within each radial shell to be the conserved quantities in the 3D to 1D translation. As the gas and radiation temperatures in each 3D cell deviate by $< 2\%$, only one temperature is needed when calculating the internal energy there-in,

$$E_{\rm int} = \frac{3}{2}P_{\rm g} + 3P_{\rm r} = \frac{3k_{\rm B}}{2\mu m_{\rm p}}\rho T + a_{\rm r}T^4, \tag{3.1}$$

where μ is the mean molecular weight. Thus we utilized the volume weighted averages of the internal energy, $\langle E_{\rm int}\rangle_V$, and density, $\langle\rho\rangle_V$, to calculate a self-consistent average temperature, $\langle T\rangle_E$, using Equation 3.1. Replacing $\langle T\rangle_V$ with $\langle T\rangle_E$, reduces the fractional difference of the internal energy ($|E_{\rm int}(\langle\rho\rangle_V, \langle T\rangle_i) - \langle E_{\rm int}\rangle_V|/\langle E_{\rm int}\rangle_V$) from upwards of 60% to numerical error. Using $\langle T\rangle_E$ to estimate the thermal pressure results in an average deviation of 10^{-3} with the maximal deviation staying $< 5\%$ for all the models. This is a significant improvement compared to the average and maximal deviations of 5% and 60% respectively when using $\langle T\rangle_V$. Because of these improved agreements, $\langle T\rangle_E$ and $\langle\rho\rangle_V$ are taken to be the 1D averages of the 3D models.

Figure 3.3 compares $\langle T\rangle_V$ and $\langle T\rangle_E$ along with the typical spatial variation of T in a single temporal snapshot. The plotted regions of the models span from the innermost

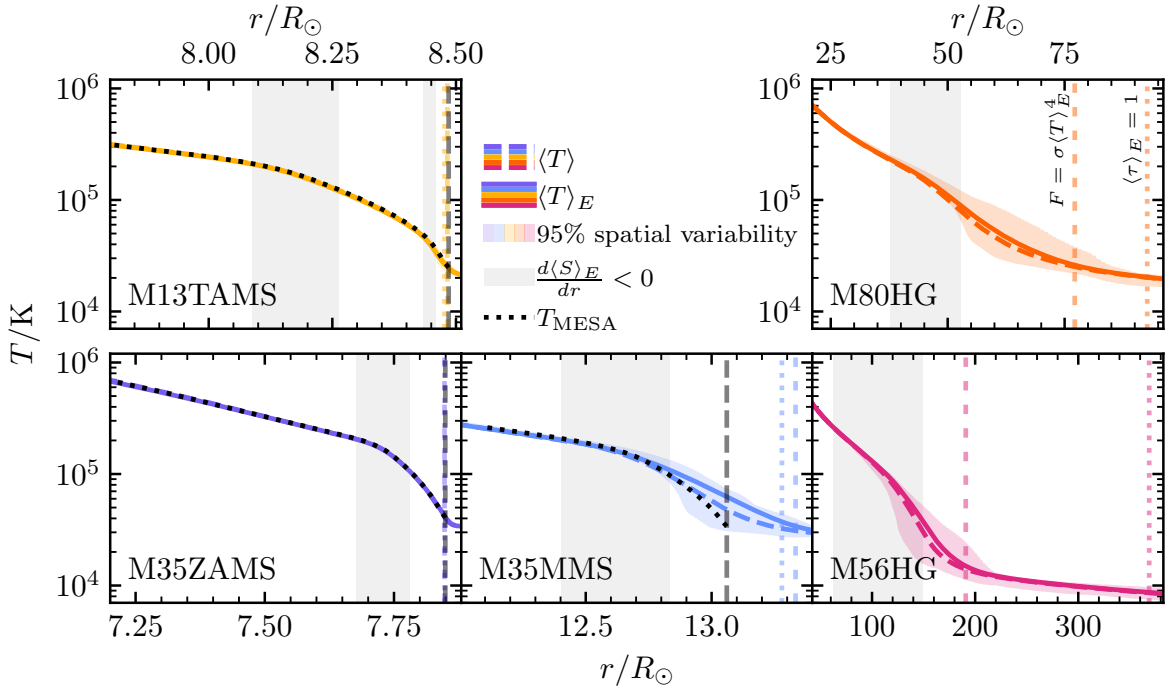

Figure 3.3: Comparison of radial profiles of the volume weighted average temperature, $\langle T \rangle_V$ (dotted lines), and the temperature extracted from the internal energy, $\langle T \rangle_E$ (solid lines), for the five models. The shaded color regions show the 95% spatial variability in a single temporal snapshot. Vertical colored lines show the radii where $\langle \tau \rangle_E = 1$ (dotted) and $L/4\pi r^2 = \sigma \langle T \rangle_E^4$ (dashed). The gray shaded regions denote where the average entropy gradient is negative, signifying a convection zone. Temperature profiles from MESA models of similar stars to M13TAMS, M35ZAMS, and M35MMS are plotted in black dotted lines with their photospheric radii shown by the vertical gray dashed lines.

radius to reach thermal equilibrium to the outer radius where $\langle\tau\rangle_E = 1$ ($\langle\tau\rangle_E(r) \equiv \int_r^\infty \kappa(\langle T\rangle_E, \langle\rho\rangle_V)\langle\rho\rangle_V dr'$). In M13TAMS and M35ZAMS, $\langle T\rangle_E$ deviates from $\langle T\rangle_V$ by less than 1% while it changes by upwards of 23%, 20%, and 13% in M35MMS, M56HG , and M80HG respectively signifying the turbulence generates correlations between T and ρ.

The overlapping or distinct locations of photosphere definitions, highlighted in Figure 3.3, arise from the varied topographies of these 3D RHD models. The 1D nature of M35ZAMS and M13TAMS leads to the location where $\langle\tau\rangle_E = 1$ coinciding within one radial cell of where $F = \sigma\langle T\rangle_E^4$. In contrast, the other three models display convective motions that reach or surpass the sound speed, resulting in strong turbulent motions at the photosphere and complex surface topography. The trans-sonic turbulence of M35MMS results in a 10% discrepancy in the predicted $T_{\rm eff}$ based on the choice of photospheric definitions, with the location where $\langle\tau\rangle_E = 1$ lying inside the flux defined surface. When turbulence becomes super-sonic, as in M80HG and M56HG, the different $T_{\rm eff}$ definitions deviate by 30% and 40% respectively with $F = \sigma\langle T\rangle_E^4$ occurring well below the location where $\langle\tau\rangle_E = 1$.

This contrast highlights the inherently 3D nature of these models. The turbulence causes complex surface topography with the radially integrated $\tau = 1$ surface spanning up to twice the stellar radius and encompassing both photospheric definitions plotted in Figure 3.3 (Schultz et al., 2023). The large topographic features yields factor of two temperature fluctuations, containing both definitions of $T_{\rm eff}$ in Table 3.1 and breaking the

notion of a single $T_{\rm eff}$ or single radius photosphere. In order to show an approximation for the surface of the 1D averages of these 3D RHD models, $F = \sigma\langle T\rangle_E^4$ is chosen to define the 1D photosphere and future figures are truncated there.

3.2.2 Comparing to MESA Models

Matching the solar metallicities of the 3D RHD models and adding exponential core overshooting with $f = 0.0014$, $f_0 = 0.004$ to smooth the HR diagram tracks, pre-main sequence models for each core mass are modeled to ZAMS using the latest release of MESA (r22.11.1). These ZAMS models are then evolved utilizing the Henyey et al. (1965) MLT option, with the default parameters ($\alpha = 2$, $y = 1/3$, $\nu = 8$) until the $\langle T\rangle_E$, $\langle \rho\rangle_V$, and r of the base of the 1D analogs of the 3D RHD models are matched. All three models matched these conditions to within 5% as the base radii are well below the Fe opacity peak in a radiative region. The inlists used to create these models are available on Zenodo under an open-source Creative Commons Attribution license: doi:10.5281/zenodo.7972070.

The T (see Figure 3.3) and ρ MESA profiles agree with M35ZAMS and M13TAMS at all radii, including the photosphere. This is the first direct confirmation that 3D RHD `Athena++` simulations with convective turbulence agree with 1D MESA models and highlights a region of the HR diagram where 1D stellar evolution models are sufficient to capture the stellar structure as well as the photospheric radii and temperatures. This region coincides with $\tau_{\rm Fe} \ll \tau_{\rm crit}$ or $L \ll L_{\rm Edd}$ as in these limits the convection does

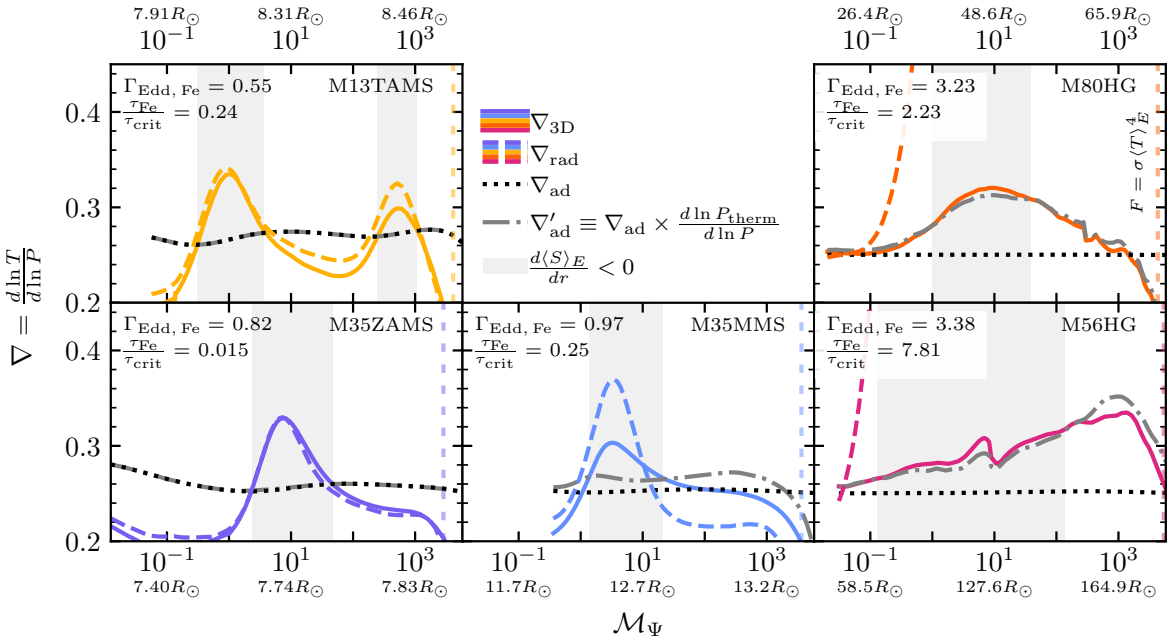

Figure 3.4: Comparison of temperature gradients for the five 3D RHD models including the realized temperature gradient, $\nabla_{\rm 3D}$, radiative temperature gradient, $\nabla_{\rm rad}$, adiabatic gradient, $\nabla_{\rm ad}$, and the modified model adiabatic temperature gradient including $P_{\rm turb}$, $\nabla'_{\rm ad}$ (colored solid, colored dashed, black dotted, and gray dot-dashed lines respectively). The vertical dashed lines are the same as in Figure 3.2. The gray shaded regions denote convectively unstable regions as in Figure 3.3.

not carry significant energy and cannot develop trans-sonic turbulence. In contrast, the MESA analog to M35MMS is slightly more compact and hotter, with $r_{\rm photo}$ and $T_{\rm eff}$ $\approx 2\%$ different than the 3D estimates. Additionally, the 3D estimate exhibits a shallower temperature gradient through and above the FeCZ, causing the change in $r_{\rm photo}$ and $T_{\rm eff}$. Despite the lack of MESA models to compare to, these discrepancies are likely to increase in the models that exhibit stronger turbulent motions (i.e. models with more massive cores, higher luminosities, and with $\tau_{\rm Fe} \gtrsim \tau_{\rm crit}$). It is clear that new prescriptions of turbulent heat transport are required to improve the 1D stellar evolutionary models in this regime.

The MESA models utilizing the default MLT parameters also predict convective velocities at the Fe opacity peak. Table 3.1 shows the difference between these velocities and the 3D RMS velocities at both the Fe opacity peak ($v_{\mathrm{MESA,Fe}}$ and v_{Fe} respectively) and the He opacity peak ($v_{\mathrm{MESA,He}}$ and v_{He} respectively). The He opacity peak velocities disagree with those seen in the 3D models due to convective overshooting. At the Fe opacity peak, the velocities differ by 32% in M13TAMS, a factor of 3 in M35ZAMS, and 22% in M35MMS. Considering these comparisons utilize the same default MLT parameters for all the models, it is surprisingly accurate given the differences of the models.

Modifying the y and α MLT parameters for each MESA model can yield better agreement. Keeping $\alpha = 2$, the peak velocities in MESA's FeCZ agree when $y = 0.2$, $y = 0.1$, and $y = 1$ for M13TAMS, M35ZAMS, and M35MMS respectively. Alternatively, for $y = 1/3$ we find agreement with $\alpha = 1.7$, $\alpha = 1.3$, and $\alpha = 4.5$ for M13TAMS, M35ZAMS, and M35MMS respectively. These changes in y and α do not create significant changes in T_{eff}, r_{photo}, or the temperature profiles with all deviations being $< 0.5\%$ as radiation remains the dominant energy transport mechanism. Both y and α impact the estimates of the convective velocity, however they impact different weak turbulence regimes. Reducing y is likely the correct modification when $\tau \ll \tau_{\mathrm{crit}}$ (M35ZAMS) while reducing α is the better choice in the lower luminosity regime where $L \ll L_{\mathrm{Edd}}$ (M13TAMS).

3.2.3 Temperature Gradients in Turbulent Envelopes

Energy transport defines the temperature gradient, $\nabla \equiv \ln T / d \ln P$, in 1D stellar models which is compared to two distinctly defined gradients. The first is $\nabla_{\rm rad}$, the temperature gradient required to carry the flux solely by radiative diffusion (see Equation 27 of Henyey et al., 1965). The second is the adiabatic temperature gradient, $\nabla_{\rm ad}$, which is often realized in efficient convection as plumes rise and fall nearly adiabatically. Figure 3.4 compares the 3D temperature gradient, $\nabla_{\rm 3D}$, with $\nabla_{\rm rad}$ and $\nabla_{\rm ad}$. For M13TAMS and M35ZAMS, ∇ is well approximated by $\nabla_{\rm rad}$ further agreeing with the $\tau \ll \tau_{\rm crit}$ picture. The convective plumes lose enough heat from radiation as they rise that the convective flux is negligible and thus $\nabla \approx \nabla_{\rm rad}$.

In more turbulent models, a different picture unfolds with $\nabla_{\rm 3D}$ deviating from both $\nabla_{\rm rad}$ and $\nabla_{\rm ad}$. Below the Fe opacity peak in M35MMS, ∇ follows $\nabla_{\rm rad}$ to within 5%, however there is a departure from $\nabla_{\rm rad}$ in and above the convection zone that is also seen in M80HG and M56HG. Models M80HG and M56HG have $L \approx L_{\rm Edd}$ and exhibit $P_{\rm r} \gg P_{\rm gas}$ resulting in $\nabla_{\rm rad} \gg \nabla_{\rm ad}$. As both are convectively efficient ($\tau \gtrsim \tau_{\rm crit}$) the convective flux grows until the velocities approach the sound speed, limiting the energy transport. The resulting $\nabla_{\rm 3D}$ lies between $\nabla_{\rm rad}$ and $\nabla_{\rm ad}$ suggesting a different mechanism of convective inefficiency, aside from radiative losses.

However as discussed earlier, these trans-sonic velocities imply a significant $P_{\rm turb}$, suggesting the need for a modified $\nabla_{\rm ad}$. In this regime, Henyey et al. (1965) used the chain rule to account for the role of turbulent pressure in $\nabla_{\rm ad}$ by defining,

$$\nabla'_{\rm ad} = \nabla_{\rm ad} \times \frac{d \ln P_{\rm therm}}{d \ln P}, \tag{3.2}$$

where $P = P_{\rm therm} + P_{\rm turb}$. For M13TAMS and M35ZAMS, $\nabla'_{\rm ad}$ is equivalent to $\nabla_{\rm ad}$ but for the others there is a noticeable change. In fact, when $\nabla'_{\rm ad}$ is used, the superadiabaticity ($\nabla_{\rm 3D} - \nabla'_{\rm ad}$) of M80HG and M56HG is reduced significantly implying the convection is truly efficient and follows the modified model adiabatic temperature gradient that includes the impact of $P_{\rm turb}$. Additionally, the definition of the convection zones, where $dS/dr < 0$, agree identically with the regions where $\nabla > \nabla'_{\rm ad}$ rather than the conventional $\nabla_{\rm ad}$ in all the models. Thus when models have significant turbulent pressure, 1D models must utilize $\nabla'_{\rm ad}$ to properly estimate the convection zones' properties.

3.3 Conclusions

We present five 3D RHD `Athena++` models that highlight the impact of turbulence in massive star envelopes. When the stellar luminosities are sufficiently high and NSCZs are adequately optically thick as to develop trans-sonic convective velocities, the ram pressure of the turbulence can account for nearly 80% of the pressure support. This additional pressure support modifies the temperature change of an adiabitically rising plume, reducing the estimated superadiabaticity and confirming that convection is efficient. Estimating the turbulent pressure for 1D models using physically motivated prescriptions will be vital for improving estimates of stellar observables. That being said, it is important to remember that turbulence makes photospheres inherently 3D and

care should be taken when interpreting 1D photospheric values in this realm.

Our work has highlighted two clear regimes. In the weak turbulence regime, in the lower left of the HR diagram, the NSCZs are either too radiatively lossy (M35ZAMS) or have sufficiently low luminosities (M13TAMS) to impact the stellar structure. The opposite is true for the efficient luminous regime in the upper right of the HR diagram (M80HG and M56HG) where turbulence dominates the envelope. M35MMS is the only model currently in the transition between these two regimes. As computational costs limit the number of models we can run, we have only attempted to compare the existing models to their MESA counterparts and note the impacts of the turbulent NSCZs. We are excited to see that 1D stellar evolution models agree with 3D RHD simulations in the weak turbulence regime and as more 3D models are computed, the transition between spherically symmetric and inherently 3D envelopes may be mapped and 1D turbulent pressure prescriptions developed to improve stellar evolution models.

Chapter 4

Photometric Variability from Near-Surface Convection Zones

The complex interplay of convection and radiation at massive star surfaces is now being probed by photometric observations of these stars from space-based telescopes (e.g. TESS (Ricker et al., 2015)) which have detected ubiquitous low amplitude temporal brightness variability. Regardless of their spectral class, metallicity (Z), or rotation rate, all massive stars exhibit broad-band photometric variability up to 5 mmag ($\approx 0.5\%$) on timescales of hours to days (Bowman et al., 2019b,a, 2020; Bowman, 2020), which is referred to as stochastic low frequency (SLF) variability. These same stars also exhibit large-scale surface velocity fluctuations with macro-turbulence velocities of $10-120\,\mathrm{km\,s^{-1}}$ that are detected with ground-based, high resolution spectroscopy (Simón-Díaz et al., 2017).

The origin of SLF variability and the large-scale velocity fluctuations is debated. One

possible cause is internal gravity waves (IGWs) generated in the convective hydrogen burning cores that propagate through the radiative envelope and manifest near the stellar surface (Aerts et al., 2009; Aerts & Rogers, 2015; Lecoanet et al., 2019). However, their observability depends on the efficiency of both the excitation processes in the core and the propagation through the envelope. Significant theoretical (Goldreich & Kumar, 1990; Lecoanet & Quataert, 2013) and computational (Aerts et al., 2009; Aerts & Rogers, 2015; Couston et al., 2018) investigations of this phenomenon have occurred. Inhomogeneities from stellar winds combined with rotational effects have also been proposed as a possible explanation of SLF variability (Moffat et al., 2008; David-Uraz et al., 2017; Simón-Díaz et al., 2018), and hydrodynamical simulations are currently predicting SLF variability signatures arising from line-driven wind instabilities (Krtička & Feldmeier, 2018, 2021). A third possible cause is surface disturbances produced by the FeCZ (Cantiello et al., 2009; Jiang et al., 2015; Cantiello & Braithwaite, 2019; Lecoanet et al., 2019), which we explore here with 3D RHD models of surface convection regions.

4.1 3D Models

This work presents two new 3D RHD models: M35ZAMS, a Zero-Age Main Sequence (ZAMS) $35\,\mathrm{M}_\odot$ star, and M35MMS, a $35\,\mathrm{M}_\odot$ star half-way through the main sequence. The model names reflect the effective temperatures, $T_{\mathrm{eff}}/10^4\,\mathrm{K}$, and luminosities, $\log(L/L_\odot)$.

4.1.1 Computational Methods

These 3D RHD simulations model massive star envelopes with the code `Athena++` (Stone et al., 2020) in spherical polar coordinates. The code solves the ideal hydrodynamic equations coupled with the time-dependent, frequency-integrated radiation transport equation for specific intensities over 100 discrete angles based on the numerical algorithm described in Jiang (2021). We use (128×128) to cover $(\theta, \phi) \in [0.4898\pi, 0.5102\pi] \times [0, 0.064]$ for model M35ZAMS and (256×256) to cover $(\theta, \phi) \in [0.4444\pi, 0.5556\pi] \times [0, 0.3491]$ for M35MMS. Model M35ZAMS utilized 384 logarithmically spaced radial bins to span $6.8\,\mathrm{R}_\odot$ to $8.2\,\mathrm{R}_\odot$, while M35MMS covers $9.7\,\mathrm{R}_\odot$ to $15.3\,\mathrm{R}_\odot$ with 336 logarithmically spaced radial bins. Both simulations use periodic boundary conditions in the angular directions and open boundary conditions at the top of the boxes. At their bases, several ghost zones enforce fixed T, ρ, F_r and maintain $v_\mathrm{r} = 0$ (See Jiang et al., 2018). These simulations take 3000 Skylake cores 4 days to run 1 day of model time. The gravitational potential is taken to be spherically symmetric, $\phi(r) = -GM/r$, where G is the gravitational constant, r is the radial coordinate and M is the total mass inside r. All the models were run with solar metallicity. We calculate opacities using OPAL opacity tables (Iglesias & Rogers, 1996) and local densities and temperatures. These opacity tables do not include additional line forces in optically thin regions. Due to computational limitations and the long time required for heat to escape the base of the envelope (> 100 days of model time), M35ZAMS and M35MMS reached thermal equilibrium down to $r = 7.1\,\mathrm{R}_\odot$ and $r = 11.1\,\mathrm{R}_\odot$ respectively and both models' FeCZ evolved for nearly 100

thermal times. The analysis we present in this work only concerns the surface regions of the simulations, in which all properties of interest in the model (e.g. velocities, densities, temperatures) are in thermal equilibrium. Another model, M13TAMS (discussed in Ch. 3) is also included for comparison, but not discussed until § 4.2.2.

To perform a basic resolution study, we ran two additional models with the same initial conditions as M35MMS: one with half the resolution and only 80 angles used for radiation as well as another with the same cell size but half the angular domain ((128×128) to cover $(\theta, \phi) \in [0.4898\pi, 0.5102\pi] \times [0, 0.064]$) and a smaller radial domain, spanning $10.9\,\mathrm{R}_\odot$ to $15.3\,\mathrm{R}_\odot$. We compare T35L5.3 to the lower resolution models in§ 4.2.

In this work, all 1D comparisons are with reference to Modules for Experiments in Stellar Astrophysics (MESA, Paxton et al., 2011, 2013, 2015, 2018, 2019) models. Specifically, MESA models generated using the default inlist values from version 15140 were used to both determine the stellar parameters to use as well as the initial conditions for the `Athena++` simulations. MESA models from Cantiello et al. (2021) were used to show stellar evolutionary tracks in Figure 4.1.

4.1.2 Model Parameters and Characteristics

Figure 4.1 shows where our 3D models lie in the spectroscopic HR (sHR) diagram and compares them to previous RHD models, MESA stellar evolution tracks, and recent TESS observations of solar metallicity stars. M35MMS was chosen to closely match three TESS observations and M35ZAMS was chosen to be a more convectively-quiet

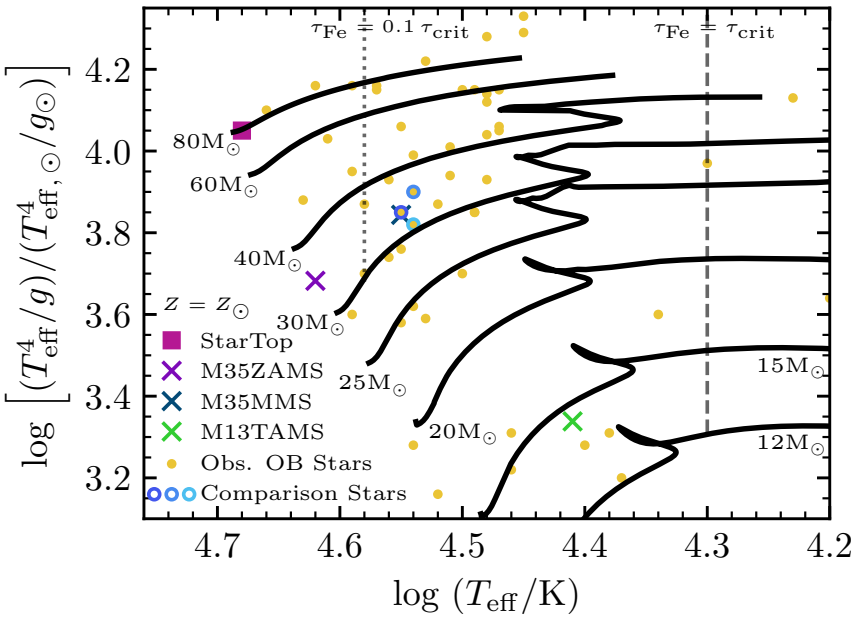

Figure 4.1: Spectroscopic HR diagram showing locations of new models (the three Xs) relative to recent TESS observations and stellar evolution tracks (the black lines). The gold circles denote OB star observations from Burssens et al. (2020) while the blue outlines surround stars against which our models are compared in § 4.2. The magenta square symbolizes the StarTop model from Jiang et al. (2015): a plane parallel model of the surface of an 80 $M_\odot$ star. The vertical lines denote locations where the optical depth to the iron opacity peak, $\tau_{\rm Fe}$, is equal to (dashed) or 10% of (dotted) of $\tau_{\rm crit}$.

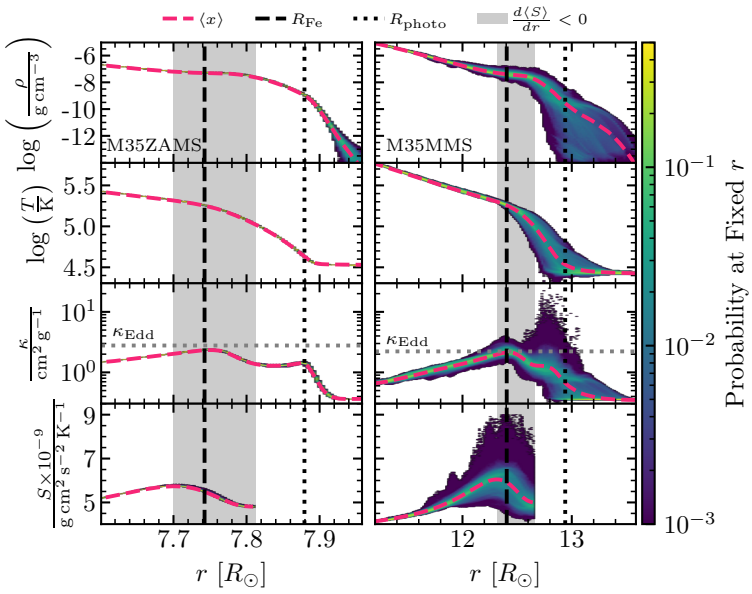

Figure 4.2: Profiles of density, temperature, opacity, and entropy (top to bottom respectively) from a single temporal snapshot of M35ZAMS (left) and M35MMS (right). The pink dashed lines show the radial profile generated from a volume weighted shell average and the color shows the probability that each quantity has the specified value at that radius. The sum of the color along vertical lines in each panel is 1. The vertical dashed black line shows the location of the iron opacity peak and the dotted black line represents the photosphere (where $\langle \tau \rangle = 1$). The gray shaded region denotes where the averaged entropy gradient is negative. In the κ panel, the horizontal line represents the opacity above which the model is super-Eddington.

model for comparison and to probe dynamics in hotter stars with $\tau_{\rm crit} \ll \tau_{\rm Fe}$.

The stark contrast in variance of fundamental variables is depicted in Figure 4.2, which shows the variations in quantities of interest for single temporal snapshots of both models long after they have reached equilibrium. M35ZAMS shows nearly no variations throughout the optically thick region. This is likely because the entire profile of this model is sub-Eddington and convective flux carries $< 1\%$ of the total flux.

In contrast, M35MMS displays significant variations at each radius including several orders of magnitude of density fluctuations in the optically thick region. Vigorous

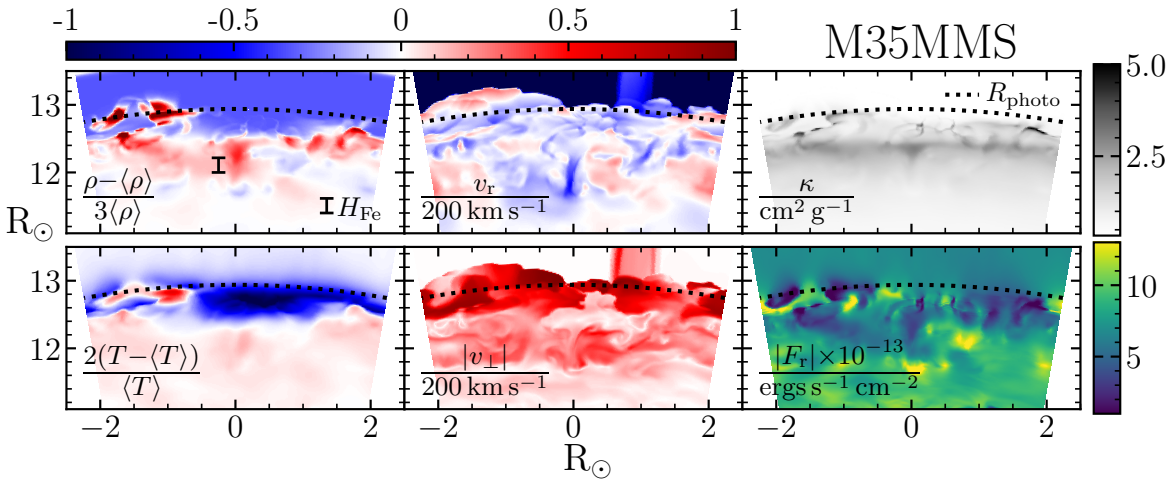

Figure 4.3: Slices of over-density, radial velocity, opacity, diffusive radiative flux, tangential velocity magnitude, and over-temperature (clockwise from upper left respectively) though a θ-r plane of a single temporal snapshot from M35MMS. The black dotted line shows the photosphere for the entire snapshot and the scale height at the iron opacity peak, $H_{\rm Fe}$, is denoted by the scale-bar.

convection in the FeCZ carries $\approx 12\%$ of the total flux and the motion of the convective plumes cause significant variations at higher altitudes. As seen in Red Supergiant models (Goldberg et al., 2021), we find that over-densities propagate upwards due to radiative accelerations, but here associated with the He opacity peak near the surface. Despite the luminosity being larger than the local Eddington luminosity near the Fe and He opacity peaks, the radially-averaged density profile does not have any inversions which plague 1D models.

Shell averaged radial profiles of M35MMS are more compact than the initial 1D MESA model due to reduced radiation support caused by correlations between $F_{\rm r}$, ρ, and κ as discussed in Schultz et al. (2020). These correlations are visible in Figure 4.3 which displays a θ-r plane slice of a snapshot of M35MMS. This shows that ρ and κ are

correlated while both being inversely correlated with $F_{\rm r}$ leading to a reduced radiative pressure gradient $\nabla P_{\rm r}$. Not enough turbulence was generated in M35ZAMS for the correlations to lead to substantial reductions in $\nabla P_{\rm r}$, however the correlations are still present just outside the photosphere.

Figure 4.3 also shows the structure of the opacity, density, and both radial and tangential velocity fields, $v_{\rm r}$ and $v_{\perp}$ respectively. The Fe opacity peak can be seen as the gray band-like structure at $r \approx 12.7\,R_{\odot}$ and the dark clumps near the photosphere are peaks from the He opacity. These opaque regions are associated with dense clumps launched from convective plumes, which are as large as the scale height at the iron opacity peak, $H_{\rm Fe}$. The velocity field is significant throughout the near-surface region, with $v_{\rm r}$ and $v_{\perp}$ comparable below and at the FeCZ, but $v_{\perp}$ dominates by a factor of a few at and above the photosphere. As most of the plumes turn around at the photosphere, the radial velocity decreases and the tangential velocity increases slightly as plumes spread out and begin to fall back into the star.

4.2 Comparisons to Observations

We now compare the surface velocities and photometric variability from the simulations with observations and 1D models.

4.2.1 Near-Surface Convection and Surface Velocities

Figure 4.4 shows the spread of rms velocities throughout our models as well as typical values for the rms tangential and radial velocities, $\langle\sqrt{v_\perp^2}\rangle$ and $\langle\sqrt{v_\mathrm{r}^2}\rangle$ respectively. The rms velocities from the 3D RHD models persist well outside the typically defined FeCZ in 1D models, with both significant undershooting and strong velocity fields at the photosphere. The velocity profiles from the MESA models, shown by the brown line in Figure 4.4, do not extend outside the region where $dS_\mathrm{MESA}/dr < 0$ though the magnitude of the velocities in these regions are comparable.

Further, our models predict there is no convectively quiet zone between the FeCZ and the photosphere. These convective motions, though carrying minimal flux, create a turbulent region spanning the outer $\approx 7\%$ of the stellar radial extent, propagating to the photosphere where we see typical surface velocities of $9.3\,\mathrm{km\,s^{-1}}$ and $123.6\,\mathrm{km\,s^{-1}}$ in M35ZAMS and M35MMS respectively. The three stars similar to M35MMS do not have reported macroturbulence velocities, however the full sample of OB stars have $10 \leq v_\mathrm{macro} \leq 120\,\mathrm{km\,s^{-1}}$ (Burssens et al., 2020). This agreement is striking considering our models are ab initio and is persistent in both our lower resolution models.

Additionally, our models appear to be dominated by tangential velocities at the photosphere, with $\langle\sqrt{v_\perp^2}\rangle/\langle\sqrt{v_\mathrm{r}^2}\rangle \sim 2-10$. This anisotropy agrees with the recent observational work which determined that radial-tangential fits match observed macroturbulent broadening better than an isotropic Gaussian fit (Simón-Díaz et al., 2010, 2014, 2017) though the extremity of the ratio of the tangential and radial components is debated.

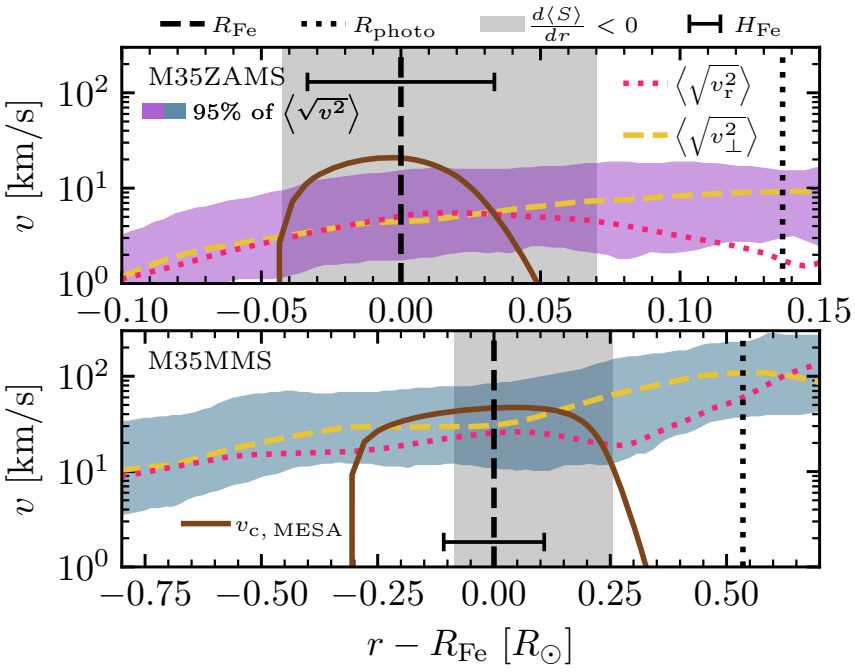

Figure 4.4: Velocity profiles for single temporal snapshots of M35ZAMS (top) and M35MMS (bottom) versus radius relative to the location of the iron opacity peak. The colored shaded regions denote the 95% probability interval of the rms velocities at each radius. Dashed gold and dotted red lines are the volume weighted averages rms tangential and radial velocities respectively. The solid brown line denotes the convective velocity profile from analogous 1D MESA models. The black scale-bar shows the extent of the scale height at the iron opacity peak. Vertical black lines and gray shaded regions are the same as Figure 4.2.

Models of IGW propagation predict drastically more tangential motion compared to radial (Aerts et al., 2009), whereas this work and others predict surface disturbances from the FeCZ produce more isotropic velocity fields (Jiang et al., 2015, 2018). Determining anisotropies in surface velocities is therefore vital to understanding whether surface velocities are dominated by IGWs or near-surface convection and more models with direct observational comparisons are needed to verify either hypothesis.

With this agreement, our models strongly support the hypothesis that surface velocities, both macro- and micro-turbulence, are affected by near-surface convection regions in OB stars with $M \gtrsim 35\,\mathrm{M}_{\odot}$. Additionally, the local velocity fields near the photosphere of our simulations are changing on sub-hour timescales. How this might manifest in time variability associated with spectral lines has yet to be explored, but it conveys the value of time resolved spectroscopy at ~ 10 minute cadence.

4.2.2 Stochastic Low Frequency Variability

TESS is revealing that OB stars have ubiquitous SLF variability. Specifically, the $\log g$ and T_{eff} of M35MMS closely match three O stars (HD41997, HD74920, HD326331) observed by TESS (yellow points outlined in blue in Figure 4.1). Unfortunately, no observed stars lie near M35ZAMS in the sHR diagram so a direct comparison can only be carried out for M35MMS.

Integrated luminosity from model M35MMS as a function of time after the FeCZ had safely reached thermal equilibrium is shown in the top panel of Figure 4.5. To quan-

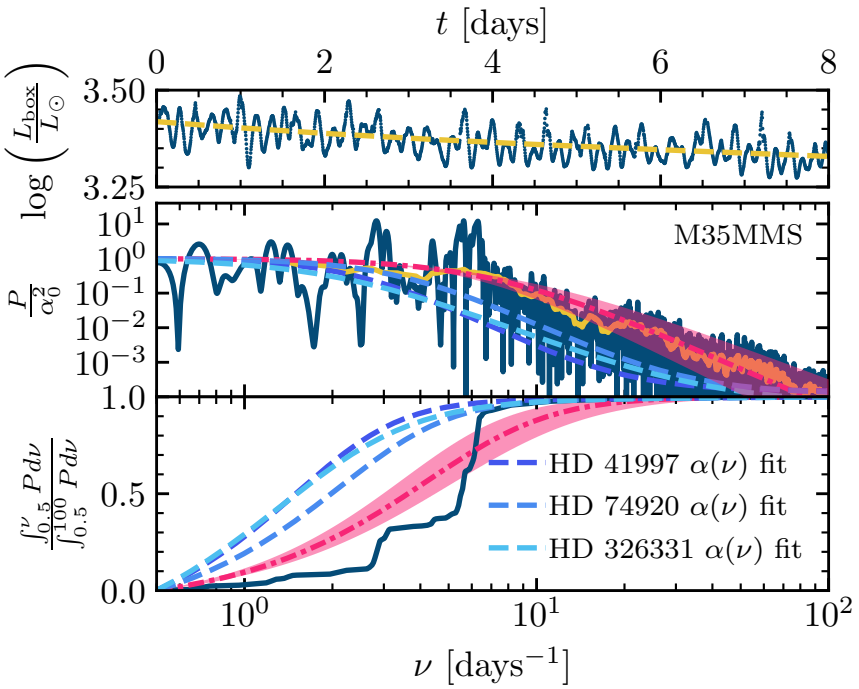

Figure 4.5: Top: Lightcurve of the M35MMS model (dark blue points) for 8 days after the model has reached a steady state equilibrium in the outer regions. The gold dashed line is a first order polynomial fit of the lightcurve used to zero-mean the lightcurve before taking the power spectrum. Middle: Power spectrum of the lightcurve from the top panel (solid dark blue line) compared to the normalized SLF fit, $\alpha(\nu)$, from observed OB stars calculated by Bowman et al. (2020) (dashed blue lines of different shades). The colors of the dashed lines match the outlines of the observed locations in Figure 4.1. The solid gold line shows the result of removing the periodic signals and linearly smoothing the power spectrum. The pink dot-dashed line denotes the $\alpha(\nu)$ fit from M35MMS and the pink shaded region shows the 95% confidence interval. Bottom: Cumulative power spectrum of all normalized power spectra on the middle panel normalize to be zero at the left limit ($\nu = 0.5\,\mathrm{days}^{-1}$) and one at the right edge.

tify the temporal variability, a first order polynomial was fit, subtracted, and divided from the model lightcurve to remove the long timescale decrease in luminosity associated with the lack of thermal equilibrium at the base of the model and calculate $\delta L/L$. Utilizing the Python code framework `SciPy` (Virtanen et al., 2020), a Lomb-Scargle periodogram (Lomb, 1976; Scargle, 1982; Townsend, 2010) was calculated from the $\delta L/L$ model lightcurve and the resulting power spectrum, normalized by the low frequency power, α_0^2, is shown by the solid blue line in the middle panel of Figure 4.5. Several peaks between $\nu = 2.5 - 7\,\mathrm{days}^{-1}$ contain nearly an order of magnitude more power than any other frequency in the power spectrum. This is further quantified in the bottom panel of Figure 4.5, which shows the normalized cumulative power spectrum, as the solid blue line contains 4 cliffs that account for 75% of the total power. Our analysis of M35MMS, M35ZAMS, and the lower resolution models showed these quasi-periodic oscillations are caused by convection driven radial and non-radial pulsations with frequencies and magnitudes that depend on the size of the simulation domain. Properties of these peaks cannot be reliably determined by our simulations.

Aside from the prominent quasi-periodic frequency peaks, SLF variability is apparent in M35MMS. Because the peaks are artifacts of our simulation domain, they are removed before a fit to the SLF variability is carried out. Instead of using the sophisticated prewhitening technique used by Bowman et al. (2019b,a) and others, the peak values were reduced to the mean of the neighboring frequency bins in the power spectrum. Then a simple moving average was used to smooth out the noise in the power spectrum, the

result of which is represented by the solid gold line in the middle panel of Figure 4.5.

Following Bowman et al. (2020), we used a Bayesian Markov chain Monte Carlo (MCMC) framework with the Python code `emcee` (Foreman-Mackey et al., 2013) to fit the amplitude of the modified power spectrum to $\alpha(\nu) = \alpha_0/(1+(\nu/\nu_{\rm char})^\gamma)+C_{\rm W}$, where $\nu_{\rm char}$ is a characteristic frequency of the knee in the SLF variability, γ sets the slope of the exponential decay, and $C_{\rm W}$ sets the amplitude of the white noise floor. As our model does not have a white noise floor, $C_{\rm W}$ was set to 0 for our fitting. The resulting fit, shown by the pink dot-dashed line with the 95% confidence intervals shown by the pink shaded region in Figure 4.5, found $\alpha_0 = 0.0023 \pm 0.0005$ in $\delta L/L$, $\nu_{\rm char} = 7.2 \pm 0.6\,{\rm days}^{-1}$ and $\gamma = 1.9 \pm 0.2$ to be the optimal parameters.

The calculated values of α_0, $\nu_{\rm char}$, and γ from the lower resolution model with the same simulation domain agree well with M35MMS ($\alpha_0 = 0.0025 \pm 0.0004$ in $\delta L/L$, $\nu_{\rm char} = 7.7 \pm 0.5\,{\rm days}^{-1}$ and $\gamma = 1.9 \pm 0.2$). The model with a smaller simulation domain only captures the dynamics of a few plumes causing reduced variability ($\alpha_0 = 0.0016 \pm 0.0005$) and stronger QPOs at different frequencies than M35MMS. The fit value of $\nu_{\rm char} = 9.5 \pm 0.8\,{\rm days}^{-1}$ in the smaller domain model may be affected by the tail of a QPO at $10\,{\rm days}^{-1}$ that our simple pre-whitening prescription cannot sufficiently remove. The plume structure does not appear to affect the power law slope as the fit value of $\gamma = 1.9 \pm 0.2$ agrees with M35MMS.

Fits for three comparison stars done by Bowman et al. (2020) are shown by the dashed blue lines in the middle and bottom panels of Figure 4.5. In an attempt to extrapolate

our small simulation domains to cover half a stellar surface, we assume the stellar surface is simply a conglomerate of our models arranged in an uncorrelated manner, we would expect α_0 to be reduced by up to a factor of $\sqrt{n}$, with $n \approx 50$ being the number of models needed to cover the surface, while $\nu_{\rm char}$ and γ would be unaffected. Using this assumption, we predict $\alpha_0 \approx 0.033 - 0.2\%$ variations in $\delta L/L$, agreeing with observed values (0.03-0.1% variations). Unfortunately, we cannot check the $\sqrt{n}$ extrapolation by comparing the α_0 of narrower box simulation and M35MMS. The small number of plumes in the smaller domain model interact and cause the assumption of uncorrelated dynamics to breakdown. To adequately confirm the $\sqrt{n}$ characterization, a simulation domain larger than that of M35MMS would need to be conducted, which is beyond the scope of this work.

Additionally, the γ value of the model's SLF variability fit agrees well with the observed values of 1.7 – 2.3. However, the characteristic frequency of our model's power spectral fit, which is consistent with the thermal timescale of the iron opacity peak region (≈ 4 hrs), is different than the $2.2 - 3.7\,{\rm days}^{-1}$ observed in similar stars. Though we have no explanation for this quantitative discrepancy in the exact power spectrum, we remain optimistic that 3D RHD models of main sequence O stars exhibit SLF variability originating from the FeCZ.

The power spectrum of the ZAMS model, M35ZAMS, is dominated by a quasi-periodic oscillation driven from a fundamental radial pulsation at $\nu \approx 18\,{\rm days}^{-1}$ but still shows the SLF variability knee with a smaller amplitude of variability compared to M35MMS.

However, when using the same technique as described above to fit $\alpha(\nu)$ for M35ZAMS we find our prediction of $\alpha_0 \approx 3 \times 10^{-6}$, $\gamma = 3.5 \pm 0.2$, and $\nu_{\rm char} = 1.2 \pm 0.05\,{\rm days}^{-1}$ to be potentially consistent with those of similar hot OB star observations (i.e. HD110360 and HD37041).

The introduction of the lower mass model, M13TAMS, allows us to address what occurs in lower mass stars. As the model was only run for 5 days, the low frequency excess cannot be directly resolved in the power spectrum of the simulation's lightcurve. However, following Cantiello et al. (2021), the characteristic frequency, $\nu_{\rm char}$, of M13TAMS is estimated to be $1.5\,{\rm days}^{-1}$ and is consistent with observations of similar stars (e.g. HD46328 and HD 50707). The RMS amplitude of the $\log L$ fluctuations from M13TAMS (accounting for the $\sqrt{n}$ geometric factor of combining n wedge models across the stellar surface) is $\approx 130\,\mu$mag, comparable to the amplitude of variability in observed stars. Thus NSCZs reproduce SLF variability in our massive star envelope models at levels and timescales comparable to those observed.

4.3 Conclusion

Our two new 3D RHD models show extended FeCZs and contain significant photospheric velocities comparable to those observed in OB stars. Vigorous, trans-sonic, turbulent convection develops in the middle main sequence model (M35MMS) causing large variations in ρ and exhibiting a He opacity peak near the surface. There is no quiet region throughout the outer part of the envelope with surface velocities of $\approx 100\,{\rm km\,s}^{-1}$, matching

observed macroturbulent velocities as well as showing a slight anisotropy in directionality, with a preference towards tangential versus radial velocities. Lightcurves from both models show prominent SLF variability which agrees in amplitude with observed OB stars, but with more power at higher frequencies than observed. These results were consistent with lower resolution and lower spatial domain models providing evidence that our models are adequately resolved.

Nearly all the OB stars with SLF variability have substantial measured surface rotation velocities (Bowman et al., 2019b,a; Burssens et al., 2020). However, as the inferred rotation periods ($\sim$ days) are typically much longer than the eddy-turnover times at the opacity peaks ($\sim$ 1 hour), we are comfortable with our current exploration neglecting rotational effects. Some of the observed OB stars with SLF variability are known to have strong magnetic fields (up to ≈ 10 kG) with recent work highlighting that strong fields can potentially alter surface dynamics (Sundqvist et al., 2013; MacDonald & Petit, 2019; Jermyn & Cantiello, 2020; Cantiello et al., 2021). Although `Athena++` has the capabilities to include magneto-hydrodynamics (see Jiang et al., 2017), most observed stars with SLF variability have fields < 10 kG, so we do not see an immediate cause to investigate magnetic field effects.

Chapter 5

Spectroscopic Synthesis from Turbulent Massive Star Envelopes in 3D

Aside from brightness variability, the other observational characteristic of massive stars is spectral line broadening, which provides information about the velocity fields at and above their surfaces. To understand how local velocity information is captured in spectral line broadening, we look to previous methods of modeling lower mass stellar spectra (Gray, 2005). Typically there are four main velocities used to fit photospheric spectral lines. Thermal broadening comes from the intrinsic Maxwell-Boltzmann velocity distribution of the ions, $v_{\rm therm}$, and is Gaussian in profile. This is often combined with the intrinsic broadening, arising from the atomic physics governing the line level transitions,

to generate a Voigt profile for the spectral line. Projected rotational broadening, $v \sin i$, imparts a deep, steep walled trench shape on stellar spectral lines as half the star is red-shifted while the other half is blue-shifted.

The other two velocities arise from the impact of turbulent motions in the line forming regions. The microturbulent velocity, denoted as ξ, accounts for additional velocities impacting scales smaller than the emitting region and is added in quadrature to $v_{\rm therm}$ in the Gaussian broadening of spectral lines. In this work, the emitting region is defined as the volume where photons experience their final interaction before leaving the stellar atmosphere and is typically similar to the scale height near the photosphere. As ξ affects the equivalent width, it is typically quantified using Curve of Growth analyses of heavy elements for which $\xi \gg v_{\rm therm}$. The other turbulent broadening arises from macroturbulence, $v_{\rm macro}$, which corresponds to dynamics on scales larger than the emitting region. This broadens the wings of the spectral lines and is typically used as a fitting parameter as discussed in Gray (2005).

Though these velocity choices were inherited from investigations of lower mass stars, they are very effective in fitting hot, massive star spectral lines (Simón-Díaz et al., 2010, 2014, 2017, 2018; Holgado et al., 2022). However because the turbulent surfaces of massive stars are significantly different than their low mass counterparts (Jiang et al., 2018; Schultz et al., 2020, 2022), it is uncertain just how accurate the inferred ξ and $v_{\rm macro}$ will be based on the existing line fitting approach. One example of an unexplained discrepancy is a strong positive correlation between $v \sin i$ and $v_{\rm macro}$ for massive stars

($M > 20\,M_{\odot}$) across the main sequence (Simón-Díaz et al., 2017). Additionally when using the current fitting method, larger ξ appears to limit the range of recoverable $v \sin i$ and $v_{\rm macro}$ (Simón-Díaz et al., 2014) implying that a quantification of these broadening velocities as well as a better theoretical understanding of their meaning in turbulent massive star surfaces are needed.

Additionally, the violent, turbulent plume structures on the surfaces of these massive stars suggest that 1D spectral synthesis models (e.g. FASTWIND, Santolaya-Rey et al., 1997) may be insufficient. A more realistic method to probe their chaotic surface dynamics are 3D RHD models where the interplay between radiation and matter is taken into account in the excitation of the turbulence. Similar investigations (see, Dravins et al., 2021, and references there-in) have been performed for lower mass (F,G,K) stars where gas pressure dominates radiation and the velocities are subsonic, allowing 3D hydrodynamic models to be used without the need for radiation pressure. These hydro models were then post-processed with radiation transport to synthesize stellar spectra with good agreement. Similar work with RHD models has been done for red supergiants (RSG) where radiation becomes an important source of pressure support near the surface (Chiavassa et al., 2011). Using the 3D radiation transport code, OPTIM3D, Chiavassa et al. (2009) post-processed their CO^{5}BOLD (Freytag et al., 2002; Freytag & Höfner, 2008) RHD models, using tabulated extinction coefficients specific to T and ρ of RSG surfaces to generate wide frequency range spectra.

For hotter massive star envelopes, the problem requires more computational resources

as the entire envelopes are supported by the interplay between plasma, radiation, and turbulence. Near-surface convection zones excited by near-Eddington luminosities traveling through opacity peaks lead to turbulent dynamics and inefficient convection as both the motions become trans-sonic and the optical depths are low enough that rising plumes can lose heat from radiative cooling (Goldberg et al., 2022; Schultz et al., 2022). Fortunately, this physics is within the reach of our 3D gray RHD simulations, which have been run using `Athena++` (Stone et al., 2020), and we can now post-process them for the desired spectroscopic analysis.

We chose to post-process our `Athena++` models using `Sedona`, a Monte Carlo (MC) radiation transport framework originally developed to model supernova light curves, spectra, and polarization (Kasen et al., 2006). `Sedona` calculates frequency-dependent opacities directly from atomic data in the co-moving frame of each cell without the need for the Sobolev or line expansion approximation, allowing for generic applications to a wide range of stellar envelopes with adjustable frequency resolution. Additionally, the MC transport is beneficial as it directly tracks the transport paths of photons through the clumpy and dynamic plume structures and can be used to estimate viewing angle dependencies from 3D simulations. Though not used in this analysis, `Sedona` allows for future expansions of this work: exploring polarization of the emitted flux, comparing gray and non-gray radiation transport, and comparing LTE and non-LTE calculations in investigations of wind lines. Two major modifications to `Sedona` were needed to adapt it to massive star surfaces. A 3D spherical wedge geometry, matching that of our `Athena++`

simulations, was added to be able to initialize our models in the `Sedona` framework. Additionally, a novel emission method was developed to avoid transporting MC particles through excessively optically thick zones. Detailed discussion of these modifications are presented in § 5.2.

Generating synthetic spectral lines from a turbulent stellar surface is nontrivial. Forests of lines and ionization changes cause the stellar atmosphere to become more opaque, the average of which results in the Fe and He opacity peaks seen in gray opacities. This leads to stronger radiation forces on these opaque fluid parcels, which rise until they diffuse enough for the radiation to pass through them. Due to the strong radiation field of these nearly-Eddington-limited atmospheres, the fluid parcels accelerate to trans-sonic speed and collide with adjacent plasma, generating turbulence. To accurately model the RHD of this turbulent medium, including the thermal background as well as the strong, narrow lines, a wide frequency range as well as high frequency resolution are both needed and drive up the computational cost significantly. Additionally the nearly-Eddington-limited radiation field and ρ fluctuations from the trans-sonic turbulence combine to launch plumes from the stellar surface creating a dynamic emitting region for the spectral lines that are starkly different from the 1D atmospheric models. This strong turbulence also generates large velocity contrasts, broadening the lines ($\Delta\lambda \sim 5\,\text{Å}$) to create line blending not expected in static models.

In this work we present our method for post-processing 3D models to synthesize stellar spectra. The 3D gray RHD simulations used for post-processing are described in

§ 5.1, specifically presenting model parameters for the three models investigated and a comparison of the photosphere versus $\tau = 1$ surfaces in the models. In § 5.2 we detail the Monte Carlo radiation transport methods and compare gray transport between the simulations. We describe the process of synthesizing spectral lines in § 5.3 as well as depicting the variety in emitting regions for individual lines in the models. In § 5.4 we highlight the results from one spectral line from each model and compare the impacts of $v_{\rm therm}$ and the models' velocity fields, predicting implications for ξ and $v_{\rm macro}$. We conclude with a brief summary of future work these new methods will allow in § 5.5.

5.1 3D Gray Radiation Hydrodynamic Modeling

A number of 3D gray radiation hydrodynamic (RHD) models have simulated near-surface convection zones in massive star envelopes (Jiang et al., 2015, 2018; Schultz et al., 2022). These models were performed using `Athena++` (Stone et al., 2020) and with additional radiation transport (Jiang et al., 2012; Jiang et al., 2014; Jiang, 2021). In this work, we showcase our novel spectral synthesis software pipeline by post-processing three specific `Athena++` models from the simulation suite. In Section 5.1.1, we briefly summarize the numerical treatments and the stellar properties of the envelope models. We then explain how the common interpretation of having the photosphere at a constant radius is incomplete (Section 5.1.2), and introduce the thermalization optical depth as a reliable basis for estimating where spectral features are formed and explore what these surfaces look like in our 3D models (Section 5.1.2).

5.1.1 `Athena++` Model Description

The `Athena++` stellar envelope models were run on spherical-polar grids and used an HLLC Riemann solver for the hydrodynamics. The radiation transport equation is solved implicitly using discrete ordinates and assuming local thermal equilibrium (LTE), following Jiang (2021). In our model suite, the finite volume approach of radiation transport discretizes the radiation field of each cell into 120 angular directions over the full 4π solid angle. Gravitational acceleration follows $g \propto M_{\rm core}/r^2$, not including self-gravity of the envelope, as the envelope masses within the models, $M_{\rm env}$, are $< 0.1\%$ of the core mass, $M_{\rm core}$. Rotation and magnetic fields are omitted from these models as they are not expected to significantly affect the near-surface opacity peaks or the turbulence they excite (Jiang et al., 2017; Cantiello et al., 2021; Schultz et al., 2022). As the ionization states of the plasma do not drastically affect the equation of state in stellar atmospheres with $T_{\rm eff} \gtrsim 10,000\,{\rm K}$, constant solar mean molecular weights are used in these models. These models utilize gray OPAL Rosseland mean opacities (Iglesias & Rogers, 1996) at solar composition in a fully ionized plasma. The gray opacity approximation and LTE assumption likely break down outside the stellar surface where the continuum opacity falls below atomic line opacity. Thus our analysis is limited to photospheric spectral lines.

The `Athena++` stellar envelope model parameters for the simulations used here are summarized in Table 5.1. The models are named by their $T_{\rm eff}/10^3\,{\rm K}$ and $\log(L/L_\odot)$, and simulate the outer convective regions between boundary radii of $r_{\rm base}$ to $r_{\rm max}$. Because

Table 5.1: Properties of the 3D Stellar Models

Model Name	Masses		Temperature		Luminosities		Resolution
	$M_{\rm core}$	$M_{\rm env}$	$T_{{\rm eff},F_{\rm r}}$ [a]	$T_{\rm eff}$ [b]	L	$L_{\rm Edd}$ [c]	$n_{\rm r}$, n_θ, n_ϕ
	($\rm M_\odot$)	($\rm M_\odot$)	(10^3 K)	(10^3 K)	($\log(L/\rm L_\odot)$)	($\log(L/\rm L_\odot)$)	
T19L6.4	80	0.011	25	19	6.4	6.42	512, 256, 512
T32L5.2	35	10^{-4}	35	32	5.2	6.07	336, 256, 256
T42L5.0	35	10^{-6}	42	42	5.0	6.07	384, 128, 128

Model Name	Angular Size		Radii				
	$\theta_{\rm min}, \theta_{\rm max} \mid \phi_{\rm min}, \phi_{\rm max}$	$\Omega_{\rm sim}$	$r_{\rm base}$	$r_{\rm Fe}$	$r_{F_{\rm r}=\sigma T^4}$ [d]	$r_{\tau=1}$ [e]	$r_{\rm max}$
	($\pi, \pi \mid \pi, \pi$)	(sr/π)	($\rm R_\odot$)	($\rm R_\odot$)	($\rm R_\odot$)	($\rm R_\odot$)	($\rm R_\odot$)
T19L6.4	$0.25, 0.75 \mid 0, 1$	1.41	16.3	44.0	78.6	99.1	335.5
T32L5.2	$0.44, 0.56 \mid 0, 0.11$	0.04	9.7	12.5	13.07	13.15	15.3
T42L5.0	$0.49, 0.51 \mid 0, 0.02$	0.0012	6.8	7.7	7.86	7.86	8.2

Model Name	Optical Depth		RMS Velocities		Scale Heights	
	$\tau_{\rm Fe}$	$\frac{\tau_{\rm Fe}}{\tau_{\rm crit}}$	$v_{{\rm r},\,\tau=1}$	$v_{\perp,\,\tau=1}$	$H_{\rm Fe}$	$H_{\tau=1}$
			($\rm km\,s^{-1}$)	($\rm km\,s^{-1}$)	($\rm R_\odot$)	($\rm R_\odot$)
T19L6.4	5,200	2.5	120	95	4.36	13.2
T32L5.2	1,182	0.28	68	78	0.24	0.09
T42L5.0	490	0.02	2.5	8.6	0.07	0.01

[a] Defined as the angle-averaged temperature at $r_{F_{\rm r}=\sigma T^4}$ ($\langle T(r_{F_{\rm r}=\sigma T^4})\rangle$).
[b] Defined as the angle-averaged temperature at $r_{\tau=1}$.
[c] For an assumed electron scattering opacity.
[d] Defined as the radius where the angle-averaged radiative flux is follows the Stefan-Boltzmann law ($\langle F_{\rm r}(r_{F_{\rm r}=\sigma T^4})\rangle = \sigma\langle T(r_{F_{\rm r}=\sigma T^4})\rangle^4$).
[e] Defined as the radius where the angle-averaged optical depth is unity ($\langle\tau(r_{\tau=1})\rangle = 1$).
* Note that T32L5.2 is the same model as T35L5.2 in Schultz et al. (2022) as a different $T_{\rm eff}$ definition was used.

the pressure scale height ($H \equiv P/\rho g$) is much smaller than the radial extent in these stars ($H \ll R$ in Table 5.1), only a small spherical wedge is modeled over a limited solid angle ($\Omega_{\rm sim} < 4\pi$) to limit the computational costs. The size of each wedge was chosen such that it would include at least 10 scale heights in the angular dimensions at the location of the Fe opacity peak, i.e., $(\phi_{\rm max} - \phi_{\rm min}) \times r_{\rm Fe} \geq 10\, H_{\rm Fe}$. The radial refinement is set to $\delta r/r \lesssim 0.1\%$ and the angular resolution ensures $r\delta\theta \approx r\delta\phi \approx \delta r$. This allows each model to capture ≈ 5 convective plumes, each more than 30 model cells across. The θ extent of each simulation domain is centered on π to alleviate numerical problems at the poles. The inner boundary condition fixes $T, \rho, F_{\rm r}$, and $v_{\rm r} = v_{\perp} = 0$ in the radiative region between the core and modeled regions while the outer boundary is open to allow radiation to escape and possible outflows. The angular boundaries along the θ and ϕ directions are periodic.

The `Athena++` models are initialized using 1D models from the Modules for Experiments in Stellar Astrophysics (MESA) (Paxton et al., 2011, 2013, 2015, 2018, 2019; Jermyn et al., 2023) using the default inlists. The T, ρ, and r at the Fe opacity peak in the MESA models are used with the M and L to create a hydrostatic model that is in thermal equilibrium without any convection, which initializes the 3D simulations. The outer regions of the simulation, outside of the stellar profile, are initialized with a low density floor ($\rho = 10^{-17}\mathrm{g\,cm^{-3}}$) to allow the models to find equilibrium without affecting the envelope mass and results in an integrated optical depth, $\tau_{\rm floor} \approx 10^{-6}$. When the `Athena++` run begins, the initial solution is unstable to convective motion and the

near-surface convection zones develop. The models are run until the time-averaged radial energy flux has converged and the Fe opacity peak has experienced at least three thermal times, $t_{\rm therm} = \int_{r_{\rm Fe}}^{r_{\rm max}} C_{\rm P} T / L dM$, where $C_{\rm P}$ is the heat capacity at constant pressure. Once these conditions have been met, typically after r $\gtrsim 10^7$ core hours, we are satisfied that steady-state equilibrium has been reached.

All these models are hot, bright stars with M80HG in the Hertzsprung Gap, M35MMS in the middle of Main Sequence evolution, and M35ZAMS near the Zero-Age Main Sequence. Their luminosities are nearly Eddington limited for an electron scattering opacity, $L \sim L_{\rm Edd} \equiv 4\pi GMc/\kappa_{\rm es}$, and thus any increase in opacity from prevailing Fe and He opacity peaks will cause vigorous convective dynamics. As discussed in Ch. 1, comparing the optical depth of the iron opacity peak, $\tau_{\rm Fe}$, to the critical optical depth, $\tau_{\rm crit}$, can shed light on the efficiency of the convection in the near-surface convection zone. Looking at $\tau_{\rm Fe}/\tau_{\rm crit}$ in Table 5.1, it is clear M35ZAMS will have much less efficient convection in the Fe opacity peak convection zone and thus weaker surface turbulence. Following the same logic, we expect M80HG to have the strongest convection and fastest velocity fields while M35MMS is somewhere in the middle. Comparing the surface velocities ($v_{{\rm r},\,\tau=1}$ and $v_{\perp,\,\tau=1}$) we confirm this to be the case with M80HG having the strongest velocity field and M35ZAMS having the weakest.

5.1.2 Photospheric Definition in a Clumpy Surface

All of our 3D RHD models, independent of θ and ϕ, lack the conventional manifestation of a photosphere at a constant radius. The 3D analogy to a 1D model photosphere would be identifying the location where the angle-averaged optical depth is unity ($r_{\tau=1}$, see Table 5.1). However, individual line-of-sight (e.g. along specific θ, ϕ) optical depths can differ significantly when near-surface convection is vigorous. Additionally a second photospheric definition, the location where the angle-averaged radiation field follows the Stefan-Boltzmann law ($r_{F_{\rm r}=\sigma T^4}$, see Table 5.1) also disagrees with $r_{\tau=1}$ by roughly a pressure scale height in the 3D models when turbulence is strong. Trans-sonic velocity fields, generated by the Fe and He opacity peaks near the surface (Jiang et al., 2015, 2018; Schultz et al., 2020, 2022), create large density contrasts ($\rho/\langle\rho\rangle \gtrsim 100$) over a relatively narrow temperature range ($T/\langle T\rangle \lesssim 1$). As opacity is very sensitive to density in these opacity peak regions, any over-density strongly modify the local heat transport. The complex topography of the photosphere is also characteristic for constant-tau surfaces for $\tau \gtrsim 100$.

Figure 5.1 shows ρ variations across slices of constant radius, or radial slices, at two choices of integrated volume-weighted, angle-averaged optical depth, $\langle\tau\rangle = 1$ and $\langle\tau\rangle = 10$. The optical depth is integrated along radial lines-of-sight, lines of constant (θ, ϕ), from the outer boundary of the simulation domain to the cell then angle-averaged to calculate $\langle\tau\rangle$. In M35ZAMS, the density only deviates from the mean by less than 12% at $\langle\tau\rangle = 1$ as the turbulent velocities are small and subsonic. In contrast, M35MMS and

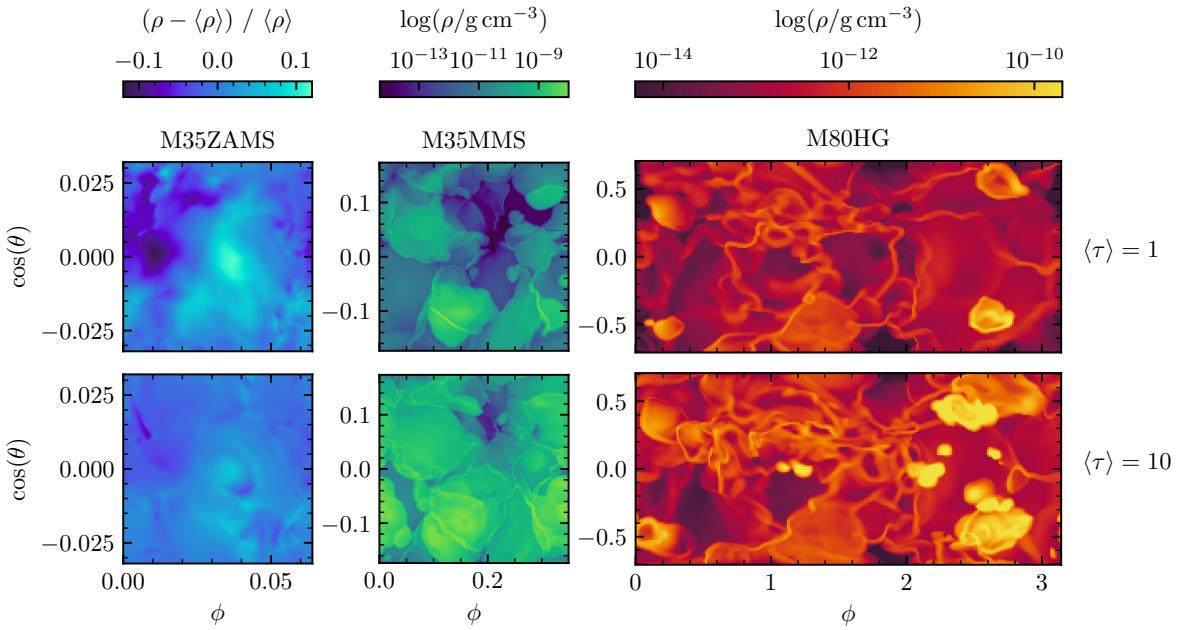

Figure 5.1: Density fluctuations through a slice at constant radius where the angle-averaged optical depth, $\langle\tau\rangle$, is 1 (top) and 10 (bottom) for M35ZAMS, M35MMS, and M80HG (left to right). Colors show over- and under-densities in the left column and $\log\rho$ for the middle and right.

M80HG contain ρ values spanning more than four orders of magnitude at single radial locations resulting from the trans-sonic turbulence at both $\langle\tau\rangle = 1$ and $\langle\tau\rangle = 10$. As $\langle\tau\rangle$ is approximately the optical depth of the deepest cell, and $\tau_{\rm cell} \approx \kappa\rho\delta r$, the large ρ contrasts with comparatively small changes in κ and δr result in optical depth variations of $\tau \sim 0.1 - 1000$ along these radial slices. Defining a single radius where the angle-averaged optical depth equals a chosen constant is therefore not a reliable approximation for the photosphere. Instead, we found that surfaces of constant thermalization optical depth, which can span several scale heights, are the more realistic representation of the local photosphere.

Thermalization Optical Depth Surfaces

Identification of the line-emitting region is paramount for establishing a physical understanding of the velocity broadening seen in synthetic spectral lines. Thus instead of looking at $\tau(r) \equiv \int_r^\infty \kappa(r')\rho(r')dr'$, where $\kappa(r')$ is the total opacity, dividing the opacity into absorption and scattering components, $\kappa_{\rm a}$ and $\kappa_{\rm s}$ respectively, when performing the mean free path analysis results in the thermalization optical depth (also known as the effective optical depth, see §1.7 of Rybicki & Lightman, 1979),

$$\tau_{\rm th} \equiv \int_r^\infty \sqrt{\kappa_{\rm a}(r')\left(\kappa_{\rm a}(r') + \kappa_{\rm s}(r')\right)}\rho(r')dr'. \tag{5.1}$$

This defines the optical depth with regards to creation events (via thermalization) of the photon rather than the location of last scattering. We can estimate the typical number of emission and absorption events using $N \approx \tau_{\rm th}^2$. The condition $\tau_{\rm th} = 1$ thus characterizes

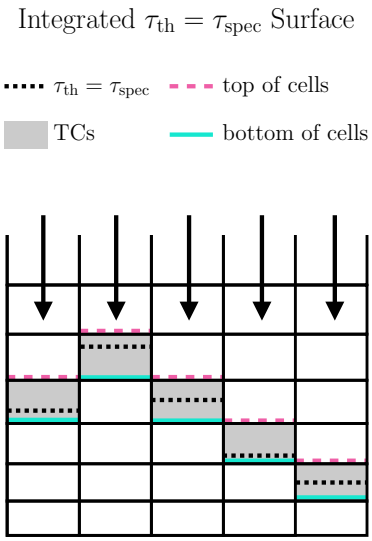

Figure 5.2: Schematic of the constant (θ, ϕ) integration process for integrated $\tau_{\rm th} = \tau_{\rm spec}$ surfaces, where $\tau_{\rm spec}$ is the desired value for $\tau_{\rm th}$. The black dotted line depicts the location along each radial line-of-sight where $\tau_{\rm th}$ is equal to the desired value, while the pink dashed and solid cyan lines show the top and bottom of the cell in which the equality is met respectively. The cells themselves, referred to as thermalization cells (TCs), are shaded in gray.

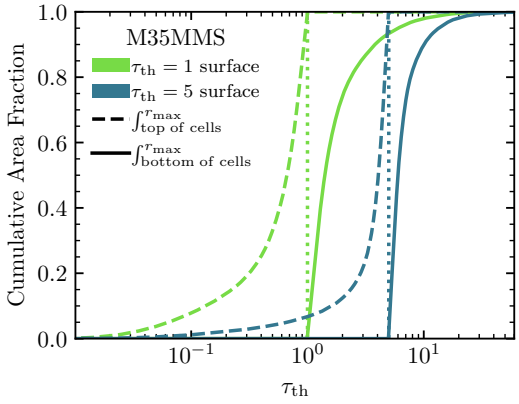

Figure 5.3: Variety in definition of integrated $\tau_{\rm th}$ surfaces for M35MMS shown as the cumulative area fraction versus thermalization optical depth (see Equation 5.1). Linestyles indicate the location of the termination of the optical depth integral, stopping at the top and bottom of the layer cells, $x_{\tau_{\rm th}}$, shown by the dashed and solid lines respectively. Vertical dotted lines mark the value of $\tau_{\rm thresh}$ and the colors identify different choices of $\tau_{\rm th}$ for the iso-tau surfaces ($\tau_{\rm th} = 1$ and $\tau_{\rm th} = 5$ being green and blue respectively).

the regions where the photons are created.

To identify the surface along $\tau_{\rm th} = 1$, Equation 5.1 is integrated from the outer edge of the simulation domain to the local radius along fixed (θ, ϕ) radial lines of sight. The contribution of the low density floor material ($\rho = 10^{-17}\,{\rm g\,cm^{-3}}$) to the optical depth is small ($\tau_{\rm floor} \approx 10^{-5}$) and is ignored. We identify the outermost cell that contains the location where the integrated $\tau_{\rm th} = 1$, referred to as the thermalization cell (TC). A schematic diagram of this integration process to accumulate $\tau_{\rm th}$ inwards to a given value, $\tau_{\rm spec}$, as well as the definition of TCs is depicted in Figure 5.2.

Figure 5.3 compares the variety of $\tau_{\rm th}$ when integrating to the top (dashed) and bottom (solid) of the TCs in the M35MMS model. Integrating to the top of the TCs, 10% of lines of sight see significantly lower thermalization optical depths whereas including the entirety of the TCs results in 10% of lines of sight seeing twice the expected $\tau_{\rm th}$. The variety along the same $\tau_{\rm th} = 1$ surfaces in the other two models is comparable to Figure 5.3.

The large variety in $\tau_{\rm th}$ of adjacent cells are created by the turbulent structure. Infalling material, previously ejected from earlier plumes penetrating the surface, collides with rising plumes creating shocks and thus high density contrasts. These high density contrasts are responsible for the significantly higher $\tau_{\rm th}$ along many of the $\tau_{\rm th} = 1$ surfaces (green solid line in Figure 5.3).

The spatial variety of integrated $\tau_{\rm th}$ along the bottom of the TCs is shown in the top panel of Figure 5.4, which also depicts the r, T, $v_{\rm r}$, and $v_{\perp}$ (in vertical order) for the

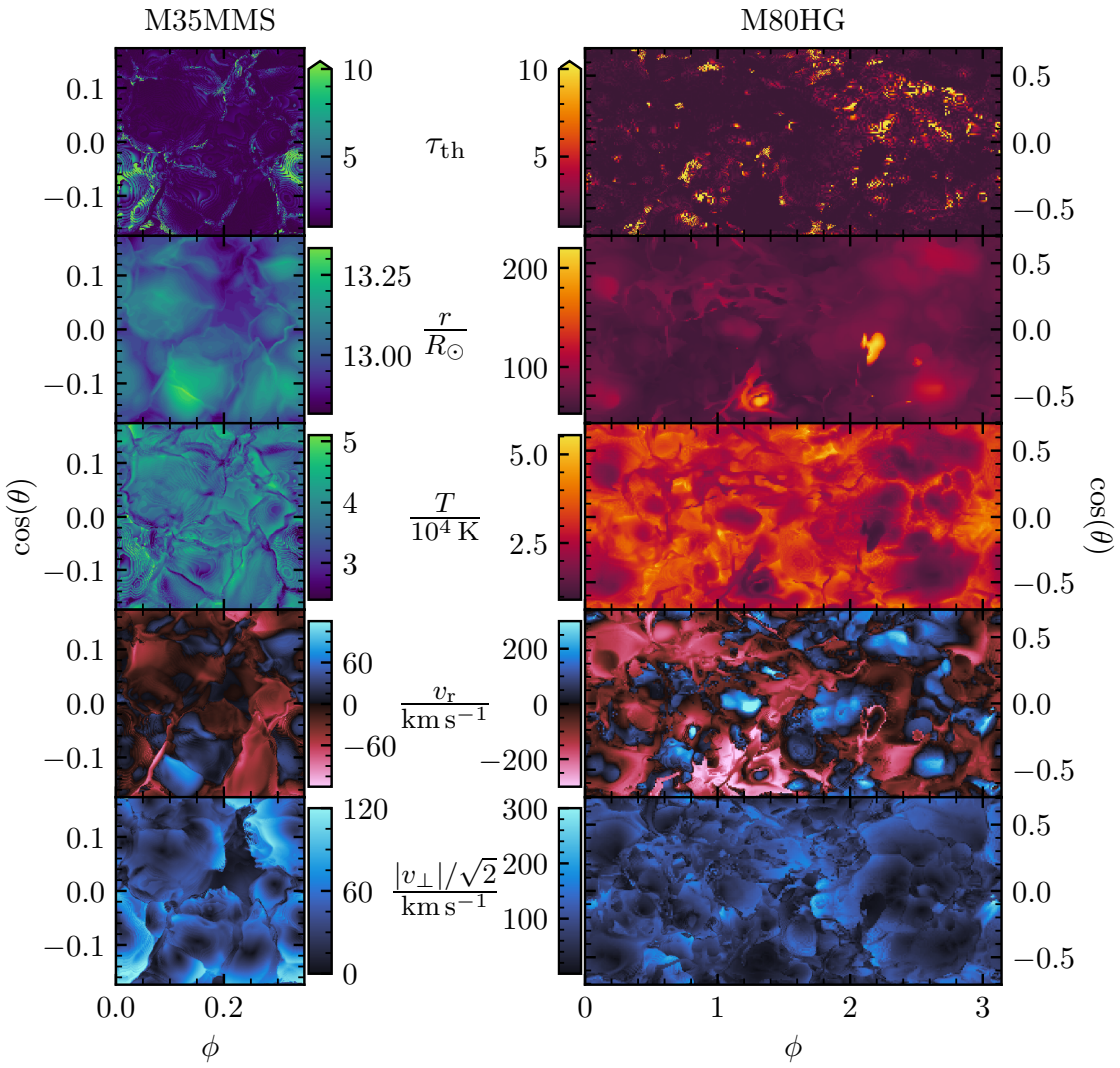

Figure 5.4: Properties of models M35MMS (left) and M80HG (right) along the integrated $\tau_{\rm th} = 1$ surface from the outer boundary of the simulation domain along radial lines of sight. The thermalization optical depth integrated through the cell ($\tau_{\rm th}$), radius (r), temperature, (T), radial velocity ($v_{\rm r}$), and tangential velocity magnitude ($|v_\perp|/\sqrt{2} = \sqrt{0.5(v_\theta^2 + v_\phi^2)}$) are plotted from top to bottom. The colorbars for the tangential velocity panels are identical to the positive (outward velocity) halves of the radial velocity panels.

TCs for M35MMS and M80HG. Several distinct plumes can be seen as the radial extent varies in the second-to-top panels with two plumes extending an additional stellar radius in M80HG. The plume structure is also emphasized by the contrasts in radial velocity, shown in the second-to-bottom panels. The temperature is more or less stratified with higher material being cooler than that beneath it, though the variety in temperature is relatively small. Looking at T along this surface in M80HG it may be surprising that we find $T_{\rm eff} = 19,000\,{\rm K}$ when visually the average temperature along $\tau_{\rm th} = 1$ appears closer to $30,000\,{\rm K}$. This is due to $\tau_{\rm th} = 1$ being below the $\tau = 1$ surface and because the stated $T_{\rm eff}$ is defined by the location where $\langle\tau\rangle = 1$. The cool, dense plumes shift this photospheric definition further out, reducing the calculated $T_{\rm eff}$. If instead we use the photospheric definition of $\langle F_{\rm r}\rangle = \sigma\langle T\rangle^4$, we find better agreement (see $T_{\rm eff,\,F_r}$ in Table 5.1). These are just two choices of a photosphere, that are typically consistent in 1D modeling but have drastic differences in 3D models implying more care is needed when defining the emission surface of a 3D clumpy envelope.

In LTE, T, ρ, and chemical composition determine which lines are excited while velocities determine their resulting profile. As T varies along the last emitting region, different regions could be exciting different lines. Furthermore, as temperature is relatively smooth along fixed (θ, ϕ), this implies that spectral lines are emitted from a relatively broad region rather than a single radial location. We also expect significant spectral broadening as both the radial and tangential components of the velocity field are strong ($\gtrsim 100\,{\rm km\,s^{-1}}$) with large plumes circulating up and down with substantial tangential motions. These

plumes are a scale height in size setting the scale of the velocity field, which at $\tau = 1$, implies a photon mean free path comparable to the turbulent scale. As the boundary between micro- and macro-turbulent velocities is often identified by the coherence length of the velocity field being larger or smaller than the emitting region, we expect this complex velocity structure to contribute to both the micro- and macro-turbulent broadening. Both the extended emission region and the turbulent velocity field significantly impact photospheric lines and motivate our spectroscopic analysis.

5.2 Post-Processing Using Monte Carlo Methods

The required computational resources needed for frequency-dependent 3D RHD would be more prohibitively expensive than the gray 3D RHD models. Instead, a more productive approach to predict observables is to post-process the 3D RHD models with a frequency-dependent radiation transport code. To this end, we modify the Monte Carlo radiation transport framework `Sedona`, originally developed for synthesizing photometric and spectral observations from stellar transients (Kasen et al., 2006).

Monte Carlo particles (MCPs), each representing many actual photons, are propagated through a user defined medium, interacting with the matter before reaching the outer boundary of the simulation domain where they are collected and binned to yield a synthetic spectrum. `Sedona` computes frequency-dependent opacities for each zone by including the contributions from electron scattering, bound-free/photoionization cross sections (Verner et al., 1993), free-free absorption (Gronenschild & Mewe, 1978), as well

as bound-bound/line opacity (Kurucz & Bell, 1995; Verner et al., 1996). By default, `Sedona` incorporates line opacity via the line expansion formalism suitable for the steep velocity gradients of supernovae (Eastman & Pinto, 1993). In our work, we remove the line expansion formalism while aggregating the contributions from individual lines to build the opacity table for radiation transport and use atomic data from the CMFGEN database (Hillier, 2012). We adopt solar abundances for both `Athena++` and `Sedona` models. We assume LTE in `Sedona` to compute the ionization fractions and level populations of each atomic species. Performing single-zone NLTE validation calculations at similar T, ρ combinations from our 3D models confirmed that the level populations that give rise to the photospheric lines investigated in this work are not affected by non-LTE effects by more than 20%, even at the extremes of the atmospheric conditions. However, other level populations can deviate by an order of magnitude so further care will be needed to expand this work beyond the chosen lines. As `Sedona` has been used for numerous frequency dependent applications (e.g. Kozyreva et al., 2020; Tsang et al., 2020), the radiation transport methodology has been extensively tested and compared with other codes, so we focus on describing our substantial modifications that extend `Sedona`'s application realm to the surfaces of massive stars.

In `Sedona`, the MCPs are propagated in Cartesian coordinates, allowing for simple particle propagation during the transport step and the flexibility of utilizing different grid geometries. As the `Athena++` models used a spherical wedge geometry, which `Sedona` lacked, the first modification included a 3D spherical wedge geometry with peri-

odic boundary conditions. The full sphere geometry was modified to have finite angular extents with periodic boundary conditions in both θ and ϕ. Specifically, when the MCPs encounter a θ or ϕ boundary, their (θ, ϕ) positions are set such that the MCP is just inside the opposite boundary [e.g. $(\theta_{\max}, \phi_{\min}) \rightarrow (\theta_{\min} + \delta, \phi_{\max} - \delta)$ where δ is small], whereas their spherical velocity components ($v_{\rm r}$, v_θ, and v_ϕ) are unchanged.

The second major modification dealt with the large radial extent of the photosphere prevalent in the 3D models. As shown in Figure 5.4 and discussed in Section 5.1, the `Athena++` envelope models have very clumpy surfaces with sharp transitions in optical thickness. Thus if particles were initialized at a constant radius where all lines of sight had $\tau > 1$, some photons would be propagating through cells with $\tau_{\rm cell} > 100$ causing the MC transport to be computationally prohibitive. Moreover, radiation transport in such high $\tau_{\rm cell}$ region is tedious as the particles are purely diffusive, and is already well-characterized by the `Athena++` gray model. Thus, instead of using a constant radius, we defined a custom emitting region (CER) using the TCs described above that avoids the unnecessary computational cost of following long particle histories in diffusive zones.

We initialized the CER using the TCs defined by $\tau_{\rm th}$ surfaces similar to those plotted in Figure 5.4. The main difference being that a higher $\tau_{\rm th}$ should be chosen to ensure thermalization before the MCPs reach optically thin material and escape. Through testing, we found no noticeable difference between $\tau_{\rm th} = 5$ and $\tau_{\rm th} = 10$ and thus used the $\tau_{\rm th} = 5$ surface for the CER in our models. The co-moving radiative flux, contained in the input model, then defines the initial energy emitted from the desired grid zones

of the CER. The user then defines the total number of particles to emit that is evenly divided among the emitting zones.

More specifically, the MCPs are randomly generated along the faces through which radiative flux is leaving the cell. The particles are then isotropically emitted along the direction normal to the cell faces. To validate this initialization approach, an alternate method was developed in which the MCPs are placed in the center of each zone and isotropically emitted along the direction of the co-moving radiative flux to ensure sufficient angular sampling of the radiation field. In this work, as particles are only emitted in the optically thick, diffusive regime both initialization methods produce the same results. As `Athena++` is an Eulerian code with cell centered values, using the first prescription is technically more correct for propagation. However, as this forces the MCPs to propagate though half the optically thick zone it is noticeably slower than the face emission technique. Thus for this work we use the face emission method as the results have proven to be identical.

5.2.1 Verifying Novel Modifications: Comparing Gray Radiation Transport

The major modifications to `Sedona` were first tested using a gray radiation transport setup. Using ρ, T, and the gray κ_{Ross} from the M35MMS `Athena++` model as input, a CER was initialized using the $\tau_{\text{th}} = 5$ TCs using the co-moving radiative flux from `Athena++`. `Sedona` then initialized particles and propagated them through the $\tau_{\text{th}} < 5$

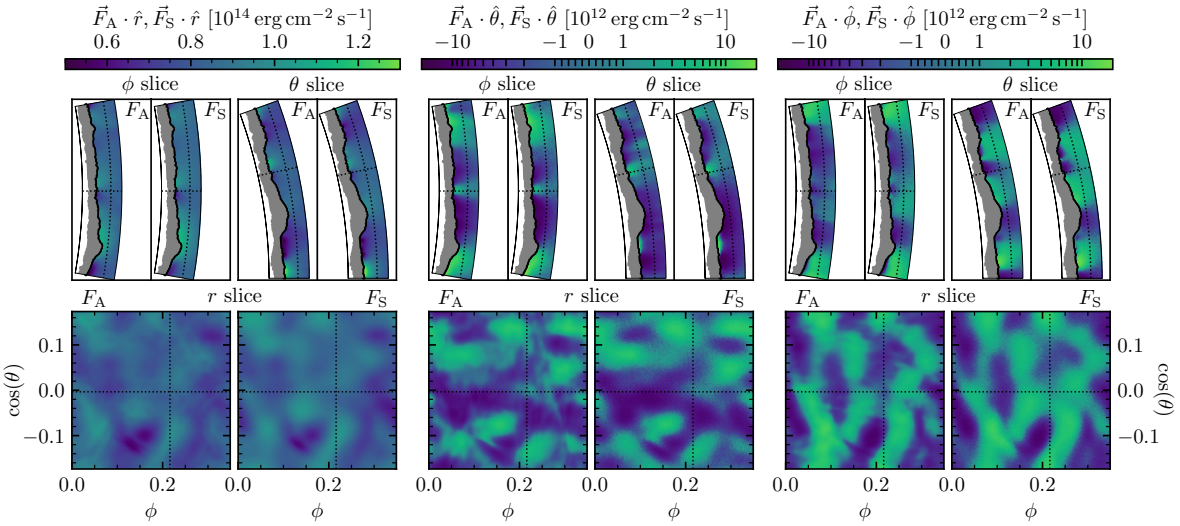

Figure 5.5: Side-by-side comparison of radiative flux in gray radiation transport of `Athena++`, $\vec{F}_A$, and `Sedona`, $\vec{F}_S$ through the same snapshot from M35MMS. The three components of the flux in spherical coordinates are directly compared: radial, longitudinal, and latitudinal from left to right. Each component is compared in three slices, one at constant longitude (ϕ slice), constant latitude (θ slice), and constant radius (r slice). The gray shaded region shows the extent of the custom emitting region (CER) from the full wedge of the `Sedona` run with the black line highlighting the outermost extent at $\tau_{th} \approx 5$. The outer extent of the computational domain is well beyond the photosphere. The black dotted lines depict where the slices intersect. All panels have unity aspect ratios.

region of the model, tallying the flux through this region while keeping $T_{\rm gas}$ and ρ fixed. Figure 5.5 compares the spherical components of the co-moving flux above the CER between `Sedona` and `Athena++`. The location of the angular slices were chosen to highlight the agreement across the high dynamic range in radiative flux. The large scale structures in the radiative flux are well reproduced and the overall radiation transport through the models are consistent.

`Athena++` appears to have some smaller scale structures that are smoothed in the `Sedona` recreation. These differences are amplified when comparing the θ and ϕ components of the flux as they are an order of magnitude less than the radial component. Regardless of the number of MCPs used in `Sedona`, the diffusive nature of radiative flux (highlighted in the ϕ slice of the θ component of the flux in Figure 5.5) remained implying the isotropic emission used in the CER method to likely be the culprit. Fortunately, the agreement between the gray radiation transport of `Sedona` and `Athena++` is strong and does not affect the generation of synthetic spectra making it suitable for this work.

It is also interesting to note that the radiation flux at $\tau \geq 1$ is not purely radial. The large-scale plume structures generate tangential temperature gradients producing diffusive radiative flux in the θ and ϕ directions. This can be seen in the center and right collections of panels in Figure 5.5 where the two components are non-zero even at the emitting layer at $\tau \approx 5$. These tangential temperature gradients lead to a $\approx 10\%$ deviation from the purely radial gradient used in deriving limb darkening mechanisms at stellar surfaces. It is unclear how the non-radial temperature gradient will affect limb

darkening but we would not expect them to be the same and further investigation is warranted.

5.3 Synthesizing Spectra via Post-Processing

Performing full frequency-dependent transport through a 3D envelope model, even when post-processing a simulation snapshot, is computationally expensive. The frequency dependent opacity, κ_ν, must be calculated for each cell individually based on the local T, ρ, and chemical composition. Furthermore, sufficient frequency resolution is needed to resolve the line-width in the co-moving frame, the lower limit of which is set by the thermal velocities of ionic species, $v_{\rm therm} \approx \sqrt{2kT/Am_{\rm p}}$ where A is the atomic number. For our models, $v_{\rm therm} \sim 1 - 10\,{\rm km\,s^{-1}}$ resulting in a requirement of $\delta\nu/\nu \sim 10^{-6}$. Enforcing the required frequency resolution across a full stellar spectrum becomes extremely memory intensive for the spatial resolution of our models. Additionally, as κ_ν near line centers greatly exceeds the opacity of the adjacent continuum, the MCPs tend to be re-emitted near the opacity peaks of spectral lines, increasing the true computational cost over the $\tau_{\rm th}$ estimate.

Therefore, in order to demonstrate the utility of proper spectral modeling, we focus on single, isolated spectral lines. We chose known photospheric lines (O III at 5594 Å and He I at 6680 Å) which were isolated from neighboring lines to ensure lines would not merge and enough continuum is present for correct normalization. Additionally, we chose lines whose κ_ν peak rose to at least ten times the continuum opacity at each

model's photospheric T and ρ to ensure similar, reasonable run-times. We constrained $\Delta\lambda > 4(1 + v_{\tau=1}/c) * \lambda_0$, where $v_{\tau=1}$ is the maximum photospheric velocity, c is the speed of light, and λ_0 is the line center.

At line centers, κ_ν is much larger than their adjacent continuum, which is typically also larger than the gray Rosseland mean opacity for a given T and ρ. Thus calculating the gray $\tau_{\rm th}$ surface using the Rosseland mean opacities will be deeper than the frequency-dependent emitting surface. Using the gray emitting surface will result in longer computation times as MCPs have to travel through optically thick cells with long particle histories. However, as we are using a Monte Carlo approach, we can increase the calculation efficiency by identifying the region of last thermalization for the MCPs and using that as a CER. We determine the layer of last thermalization by initializing MCPs at the outer boundary of the simulation domain and propagate them radially inwards along constant (θ, ϕ). Recording the cells where each MCP first experiences a thermalization event, which is typically a line-absorption event as $\kappa_\nu \gg \kappa_{\rm gray}$, provides a good localization to the expected emission region. Along radial rays with constant (θ, ϕ), cells below the deepest cells in which a thermalization event occurs are used as the CER for spectral synthesis to ensure all MCPs experience at least one thermalization event before escaping.

To further improve computing time we also reduced the angular dimensionality of the 3D RHD models used as input to the spectral synthesis calculation by a factor of 4 (e.g. 256x256 $\rightarrow$ 64x64) by averaging quantities in each cell. Volume-weighted averages were

used for ρ and the radiative energy density, $E_{\rm r} \propto T^4$, while velocities and opacities were mass-weighted and all fluxes were weighted by both opacity and mass. The weighting of the fluxes were chosen due to significant correlations between ρ, κ, and $F_{\rm r}$ which need to be accounted for in the average (see Schultz et al., 2020). In preliminary testing this re-binning had no effect on the resulting spectral line profiles when compared to the full resolution. Combining the lower resolution with the isolation of a single line allowed a full spectral profile of M80HG to be modeled with 200 frequency bins in 32 hours on a single compute node with 40 cores. This computational efficiency was important for our spectral synthesis code as it allows others to use the methodology on easily attainable resources.

The top panels of Figure 5.6 compare the thermalization locations of inwardly propagating the MCPs to several integrated $\tau_{\rm th}$ surfaces for each model. Despite being classified as photospheric lines, the majority of observed thermalization locations lie outside the $\tau_{\rm th} = 1$ surface and reach out too $\tau_{\rm th} \lesssim 0.1$. Using the inward MCPs to define the CER, the MCPs are propagated outward as detailed in § 5.2. The location of last thermalization for each MCP before it leaves the outer boundary is also recorded and the distribution of these locations are shown by the purple shaded regions in the bottom panels of Figure 5.6. The spatial locations of the green and purple distributions match well, validating the inward propagation method used to approximate the region of last thermalization and ensures each MCP experiences at least 1 thermalization event before escaping.

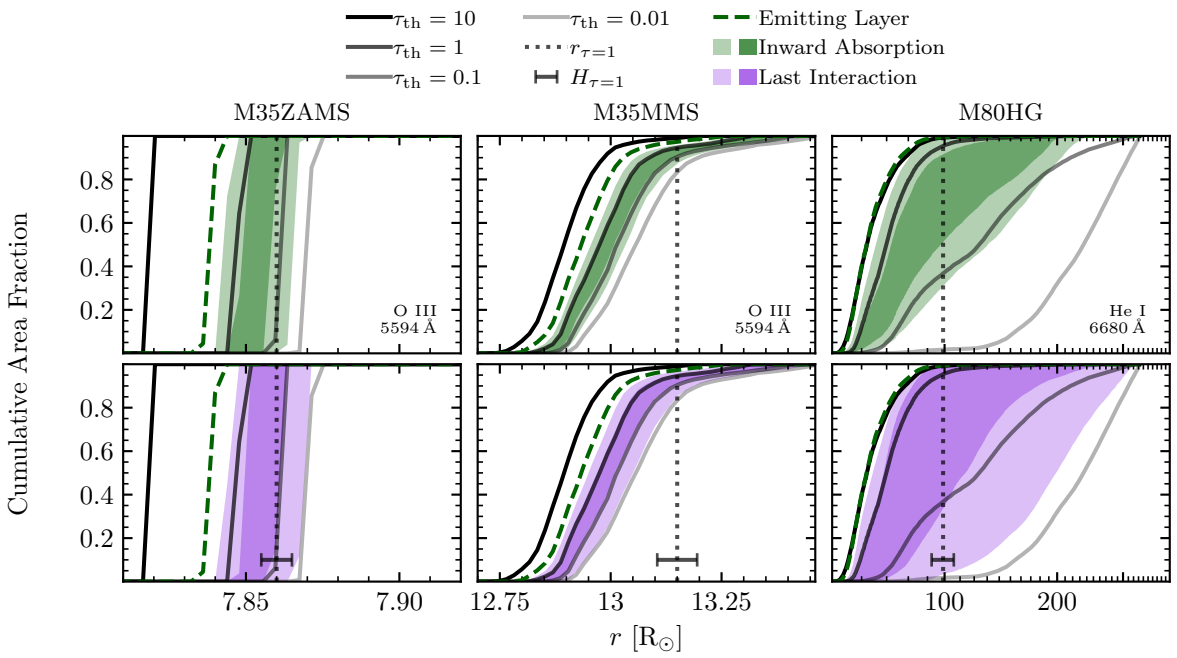

Figure 5.6: Comparison of $\tau_{\rm th} = 10, 1, 0.1, 0.01$ surfaces (solid black lines from opaque to transparent respectively) with the regions where Monte Carlo particles (MCPs) are first thermalized when propagating radially inwards (green shaded region in top panels) and the regions where the MCPs last thermalized when propagating outward (purple shaded region in bottom panels) in our 3D models. Each column is for different 3D models, M35ZAMS, M35MMS, M80HG (left to right respectively) showing individual spectral lines, O III 5594 Å for M35ZAMS and M35MMS, and He I 6680 Å for M80HG. The two shades of the shaded regions signify the areas where 68% and 95% (lighter and darker respectively) of the MCPs interact. The green dashed line shows the furthest inward location where inwardly propagating the MCPs reach, which is also used as the emitting layer for the outward moving the MCPs. The vertical gray dotted line shows the spherically averaged photosphere, $r_{\tau=1}$ and the gray scale bar shows the spherically averaged scale height at that radius, $H_{\tau=1}$.

Figure 5.6 also highlights the differences in surface variability in the different models. In M35ZAMS, where turbulence is sub-sonic, both the $\tau_{\rm th}$ surfaces and the two shaded regions appear step-like in shape implying the constant radius approximation is acceptable in these cases. Comparing M35ZAMS to M35MMS and M80HG, we see much more

extended $\tau_{\rm th}$ surfaces and emitting regions, with the more turbulent M80HG spanning nearly an order of magnitude in radius. Additionally, though the shaded regions do not lie on single $\tau_{\rm th}$ surfaces, their trends do match that of the $\tau_{\rm th}$ surfaces implying the assumption of an emission layer with a finite depth is justified as $\Delta\rho/\rho \ll 1$.

The region of last interaction in all three models can be compared to the local pressure scale height, $H_{\tau=1}$, to estimate the relative importance of micro- and macroturbulence in the spectral broadening. In M35ZAMS, the emitting region spans two local pressure scale heights, which is consistent with the small degree of ρ fluctuations as shown in Figure 5.1. Similarly, the last interaction region in M35MMS only spans a single local pressure scale height for most of the surface area, yet covers a much larger radial extent similar to the $\tau_{\rm th}$ surface shown in Figure 5.4. The variety of radial location of the emitting region causes the MCPs to thermalize at different T, ρ, and $v_{\rm r}$, $v_{\perp}$ which should manifest as macroturbulent broadening in the spectral line profile. The most turbulent model, M80HG, displays an emitting region that spans many $H_{\tau=1}$, covering nearly twice the stellar radius in extent. The turbulent broadening should be dominated by individual plume dynamics as they are expelled from the stellar surface.

5.4 Variety in Synthetic Spectra of 3D Envelope Models

To model the individual spectral profiles, selected using criteria outlined in § 5.3, we use a frequency range centered on the line center and extending to include three Doppler widths associated with the maximum surface velocity on either side. Mathematically, the frequencies range from $\nu \in [\nu_0 - 3v_{\rm max}/c, \nu_0 + 3v_{\rm max}/c]$, where ν_0 is the frequency at line center and $v_{\rm max}$ is the maximum magnitude of $v_{{\rm r},\,\tau=1}$ and $v_{\perp,\,\tau=1}$ for each model in Table 5.1. To ensure adequate sampling of the spectral lines, we divide the frequency range linearly into 200 frequency bins, ensuring that turbulent broadening will be captured by at least ten frequency bins on either side of the line center.

5.4.1 Viewing Angle Dependence

To investigate spectral lines as a function of viewing angle, we divide the outgoing MCPs into 17 $\mu \equiv \cos(\theta)$ bins, where θ is the angle between the propagation direction of an escaping MCP and the pole. The pole of each model is defined as the radial unit vector at $\theta = (\theta_{\rm min} + \theta_{\rm max})/2$ and $\phi = (\phi_{\rm min} + \phi_{\rm max})/2$. Panel (a) of Figure 5.7 shows a schematic of the μ discretization with color-coded bins, which are are evenly spaced in μ to standardize the surface area of each bin. The two most tangential bins are omitted from this analysis (not shown in Figure 5.7) as most of the flux is radial ($\vec{F}_{\rm r} \approx F_{\rm r}\hat{r}$) and thus few MCPs leave the domain at these small μ. Due to the limited number of MCPs in these μ bins,

we omit them from this analysis.

The median number of escaping MCPs per frequency bin of outgoing radiation as a function of μ is shown in panel (b) of Figure 5.7. The $\mu = 1$ bin receives two orders of magnitude more MCPs than the most tangential bin as a result of the radial component of the flux surpassing the tangential components by an order of magnitude. This reduction in particle number is also responsible for the increase in spectral noise when going from $\mu = 1$ to $\mu = 0.125$ (green to purple lines in panels (c) and (d) of Figure 5.7). This noise is quantified assuming Poisson statistics and using $\sigma = \epsilon\sqrt{N}$ where ϵ is the average flux carried by each MCP and N is the number of MCPs in each ν bin. The shaded regions around each spectral line in panels (c) and (d) of Figure 5.7 show the extent of 3σ above and below the smoothed spectral line shape (black line). The smoothed profiles utilize a Gaussian kernel of $0.5 - 1$ Å with a $\sigma_{\rm smooth} \approx 0.1$ Å. Panel (e) overlays all the smoothed spectral line profiles for comparison.

The μ dependence of spectral lines from all three models for two temporal snapshots more than a day apart can be seen in Figure 5.8. The temporal separation between snapshots is much longer than the eddy turnover times at the Fe opacity peak (1-4 hours) so the surface dynamics of these snapshots should be uncorrelated. Specifically, these times were chosen to display some of the maximally different spectral profiles that appear in our models. The three models show very different spectral line shapes as well as temporal line profile variability.

For models M35ZAMS and M35MMS, the depth of each line appears to change as

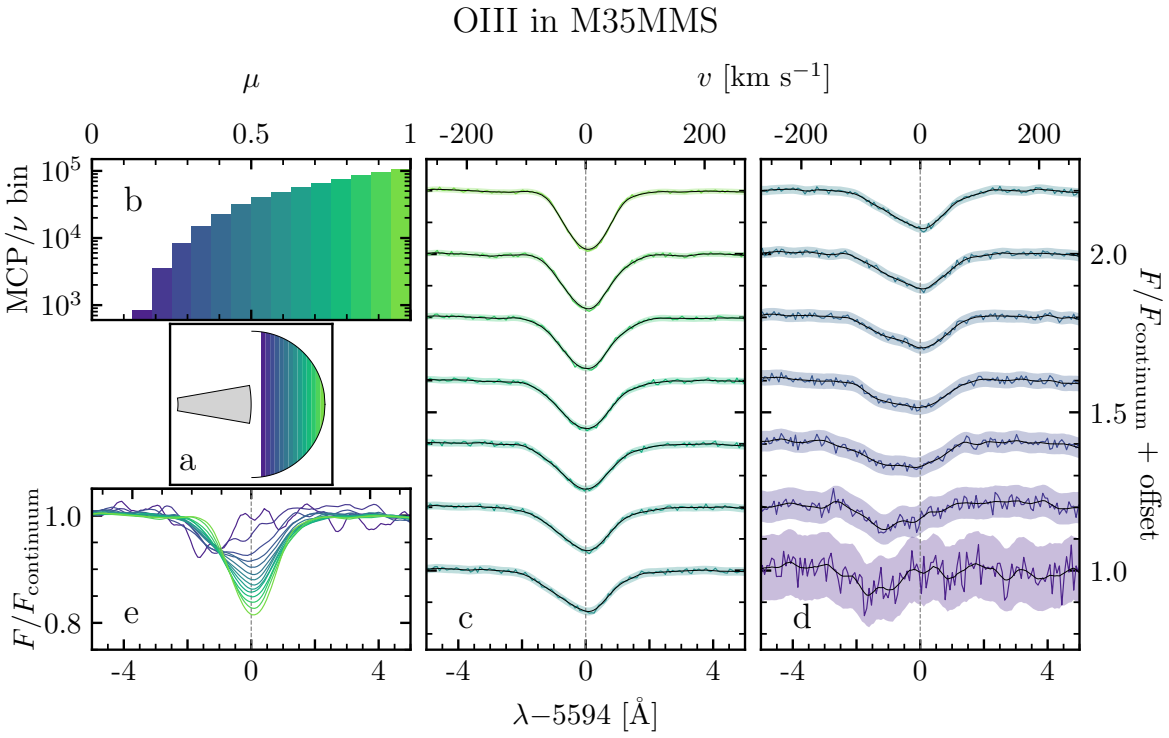

Figure 5.7: Analysis of viewing angle dependence in the O III line of M35MMS. (a): Schematic showing the simulation domain in gray and the colored areas show the different $\mu \equiv \cos(\theta)$ bins relative to the pole of the capturing surface. In all panels the color represents the given μ bin shown in this schematic. (b): Histogram of the median number of MCPs per frequency bin in each μ bin. (c) and (d): Normalized spectral lines including a vertical offset. Colored lines are the raw synthesized spectra from the different μ bins shown in (a), which are then smoothed with a Gaussian kernel (black lines). The colored regions show the 3σ error from the smoothed spectral line. (e): Overlay of all smoothed, normalized spectral lines from (c) and (d).

a function of μ. Line profiles at lower μ, generated from MCPs with more tangential trajectories, appear to have shallower depths, and thus smaller equivalent widths. These decreases in the μ dependence of the absorption depth are likely due to a limb-darkening-like effect. The MCPs collected in the lower μ bins are emitted from higher up in the model atmosphere where the line excitation is weaker resulting in shallower lines. This is further confirmed by the the lack of this μ dependence in M80HG, which covers much more of the stellar surface, allowing every μ bin to be dominated by the radial component of the flux and thus more consistent line depths. In M35MMS, the low μ trajectories are also broadened and less symmetric as the emitting region is more complex with dynamic topography and velocity fields arising from the stronger turbulent plume motions. The additional broadening is a result of $v_{\perp,\,\tau=1} > v_{\mathrm{r},\,\tau=1}$ (see Table 5.1), which broadens the more tangential trajectories of low μ bins. The asymmetry originates from the development of plume structures. As individual plumes are now separated from each other, their bulk motion affects the spectral line shape by Doppler shifting part of the profiles. As the individual plumes do not cover a large area fraction, most of the effects cancel resulting in the high μ peaks being nearly centered on the line center. However, individual plumes with large tangential velocities cause the slight shifts away from the line center in the low μ profiles.

The μ dependence is starkly different in M80HG compared to the previous two models. The stellar model is more radially extended resulting in a larger scale height, and therefore larger plumes. The motion of individual plumes, which cover a significant fraction of the

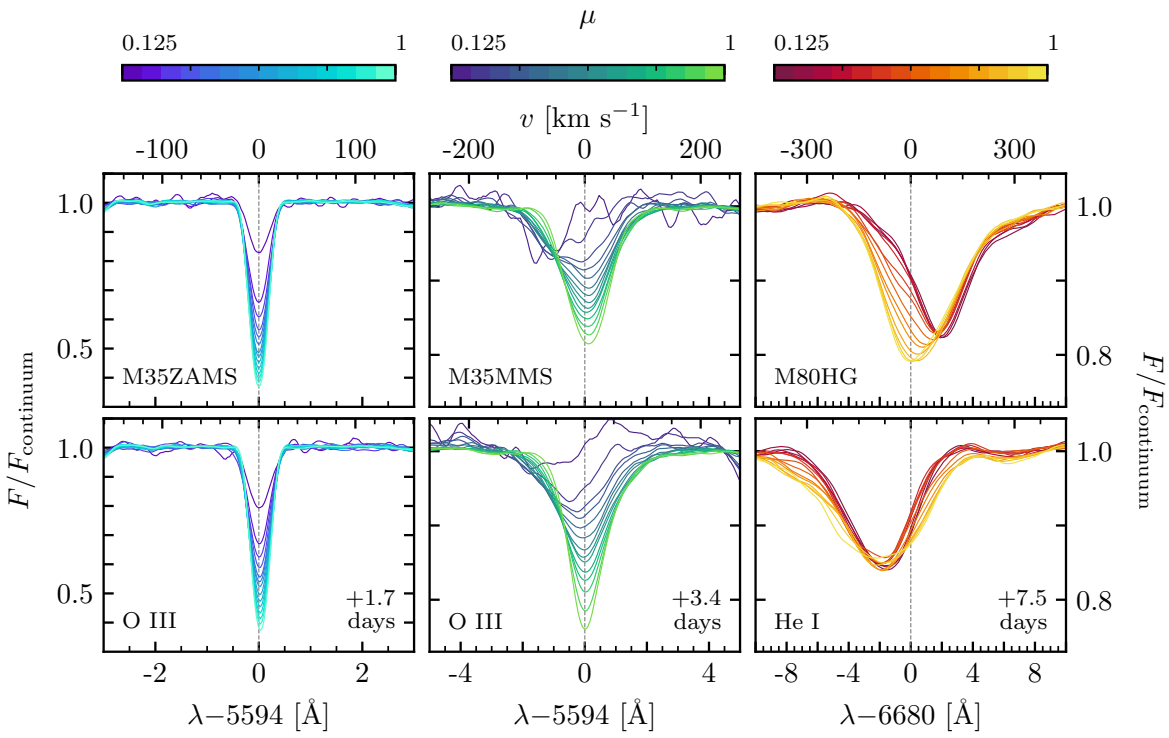

Figure 5.8: Comparison of viewing angle (colors) and temporal (top versus bottom panels) dependence on chosen spectral lines in M35ZAMS, M35MMS, and M80HG (left to right). Each panel is generated equivalently to panel (e) in Figure 5.7.

stellar surface, significantly alter the spectral profiles. For example, the redshift seen in the dark red lines, low μ profiles, in the upper right panel of Figure 5.8 are the result of plumes previously launched from the stellar surface falling back down. In contrast, the central regions (yellow lines in the same panel) do not exhibit a dominant plume motion and thus show no bulk Doppler shift. In the second snapshot (bottom right panel), all the μ profiles are blue shifted as several uncorrelated plumes are being launched in different directions. The change of slope in the upper panel near $v \approx 300\,\mathrm{km\,s^{-1}}$ arises from a neighboring spectral line that is four times weaker than the main He I line and does not impact the broadening of the line investigated here. The temporal changes in spectral shape should be observable in some of the models and are explored further in the next section when more realistic synthetic profiles are generated.

5.4.2 Synthetic Spectral Profiles

Our 3D RHD models only cover a patch of the stellar surface and especially in M35ZAMS and M35MMS the small patch size may affect the resulting spectral shapes. One way to produce more realistic spectral profiles would be to tessellate uncorrelated simulation domains together to generate a hemispherical model. Post-processing this hemispherical model would produce more realistic spectral profiles. The computational memory overhead of such an analysis depends on the atmospheric H/r value, and for our current models would be computationally challenging, but may be explored in future work. Another solution is to use the viewing angle dependence to perform a weighted average

of uncorrelated snapshots. In this subsection we present approximate spectral profiles based on combining the μ binned spectral lines from the temporally uncorrelated snapshots shown in Figure 5.8. Because we are only using two snapshots, we refrain from performing detailed quantitative spectral line analysis for the synthesized profiles. However, an approximate quantitative analysis of the different broadening mechanisms is provided below.

As the narrow models (M35ZAMS and M35MMS) are small (covering only a 50th of the stellar surface), we perform a weighted sum of the spectral flux from individual snapshots using each μ bin's projected area on the stellar disk as weights. Dividing by the mean of the resulting continuum produces the solid red and blue lines in the left and center panels of Figure 5.9. The same procedure is performed for M80HG however as the original angular coverage is much larger (covering $\approx 80\%$ of the stellar disk), the $\mu = 1$ bin is taken for the whole area of the simulation domain and weighted by its projected area on the stellar disk. The remaining area of the stellar disk is added to the weighted sum using the same procedure as above and the normalized spectral profiles are shown by solid red and blue lines in right panel of Figure 5.9. In an attempt to represent what an uncorrelated surface may look like, we perform a weighted average using alternating μ bins from the two available snapshots. Shown by the dashed lines in Figure 5.9, the similar colors represent which snapshot's $\mu = 1$ bin was used (e.g. the cyan dashed line used the same central bin as the blue solid line). To investigate how the bulk velocity field of the cells affects the spectral lines, additional calculations were

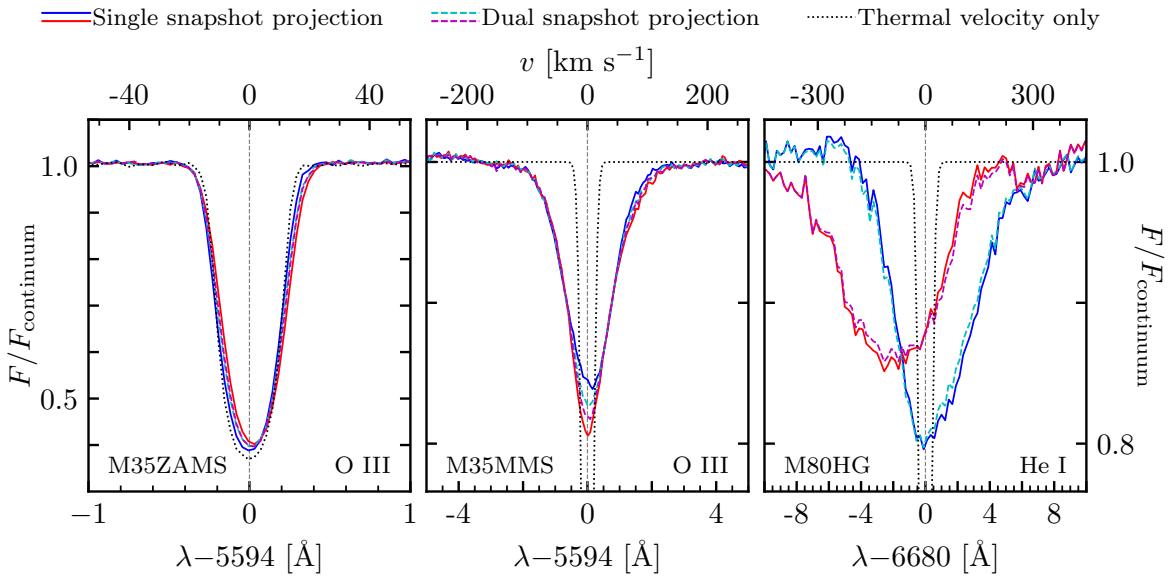

Figure 5.9: Synthetic spectral lines generated from combining the μ dependent components shown in Figure 5.8. Three combinations were chosen: the solid red and blue lines show single snapshots estimates, the dashed cyan and magenta lines show when alternating μ bins were used from both of the temporal snapshots, and the black dotted line shows a single snapshot with only the thermal velocity used.

run with all the cell velocities set to zero to generate spectral profiles resulting only from thermal broadening (shown by the black dotted lines). Ideally, we would have used many temporally uncorrelated snapshots in the projection, however as computational resources are limited, we leave this as a future exercise.

Taking these simple synthetic spectral profiles as truth, we predict all three models to show some temporal variability. The variability in M35ZAMS would be very challenging to observe, requiring a $R \sim 200,000$ spectrometer to measure the slight line center shift and very high signal to noise to catch the change in the depth of the absorption line. Model M35MMS would show signs of variability with only a $R \sim 20,000$ spectrograph

with sufficient signal to noise to resolve the change in line shape. The temporal variability of the third model, M80HG, should be easy to resolve with many spectrometers. All small fluctuations present in the colored spectral profiles are due to the Poisson noise from the finite number of MCPs and are compounded by the fact that only two uncorrelated snapshots were used. If more snapshots and MCPs were used, we would expect significantly smoother lines. Additionally, the inclusion of more uncorrelated snapshots in the projection process may reduce variability, further constraining the challenge of observing the temporal line variability.

5.4.3 The Effect of Micro- and Macroturbulence

All three panels of Figure 5.9 clearly show additional broadening beyond thermal broadening. As there is no rotation in the models, this additional broadening can only be attributed to the impact of the envelopes' velocity field, resulting in ξ and $v_{\rm macro}$. However it is difficult to determine the individual impact of ξ or $v_{\rm macro}$ on the broadening without a full quantitative analysis. The simplest distinction could be made by comparing the equivalent widths of the thermal profiles to the full velocity field lines. If the equivalent width was conserved, $v_{\rm macro}$ is likely the dominant factor and $\xi < v_{\rm therm}$ (Gray, 2005). Conversely, if the equivalent width changes, $\xi > v_{\rm therm}$ and microturbulence is likely playing a dominant role, making it hard to quantify $v_{\rm macro}$.

Unfortunately due to the noise present in the spectral line shapes, it is hard to compare the equivalent widths between the lines without pushing to more MCPs or using

more temporally uncorrelated patches. However, comparing the full width half minimum (FWHM) of each line can tell us about the dominant velocity. For M35ZAMS, the FWHM is $\approx 20\,\mathrm{km\,s^{-1}}$ which is consistent with thermal broadening as the FWHM for a Gaussian $\approx 2.4\sigma$. Visually however, it is clear the tails of the synthetic profiles in the left panel of Figure 5.9 are wider than the thermal profile suggesting the additional presence of macroturbulent broadening. For M35MMS the FWHM velocity of $\approx 80\,\mathrm{km\,s^{-1}}$ is comparable to the surface velocities, $v_{\mathrm{r},\,\tau=1}$ and $v_{\perp,\,\tau=1}$ in Table 5.1, suggesting ξ and v_{macro} are important. Due to the trumpet like shape of the profiles, we suspect v_{macro} to be more dominant though thorough fitting is required to ascertain. The FWHM velocity of M80HG is $\approx 275\,\mathrm{km\,s^{-1}}$ and is nearly double the surface velocities in Table 5.1. This suggests both ξ and v_{macro} are important in this very turbulent model and more investigation of the broadening mechanisms is warranted.

Qualitatively, our calculated spectral profile for the OIII line in M35MMS strongly resembles observed spectral profiles seen in Simón-Díaz et al. (2014). As our models contain no rotation, the $v \sin i$ values do not agree between our calculations and observations. However the observed macroturbulence velocities agree quite well with the calculated FWHM and thus the turbulent velocities in the simulation. Unfortunately, no observations of stars similar to M35ZAMS or M80HG have been carried out. Future spectroscopic surveys (e.g. Bowman et al., 2022) will observe stars that could be directly compared to our other models.

5.4.4 Thermal Profile Comparison

All the models display noticeable differences from the inclusion of velocity fields. As expected, the cell velocities broaden the profiles and decrease their absorption amplitude, providing strong evidence for the presence of macroturbulence. To quantify their widths, each thermal profile (black dotted lines) was fit to a Voigt profile (orange solid lines) in Figure 5.10. As can be seen in the left panel, but is also present in the other two panels, the Voigt profiles does not fit the full thermal profile very well: the peak is too narrow and the tails are too wide. The discrepancies arise despite the fact that the fit is dominated by the Gaussian component of the Voigt profile, making the peak as wide and the tails as narrow as possible. The lack of a Lorentzian component is not surprising as `Sedona` does not include natural broadening in the calculation of $\kappa_{\rm nu}$. However at the high temperatures of these massive star surfaces and for our chosen spectral lines, the intrinsic widths should be small compared to the thermal broadening, justifying this assumption.

Despite the shape mismatch between the thermal profiles, the widths of the fits appear to be approximately correct, especially at the FWHM, implying the standard deviation of the distribution could be used to estimate a thermal velocity using $v_{\rm fit} = \sigma c/\nu_0$, where ν_0 is the frequency at line center. However, $v_{\rm fit} \approx 1.3\, v_{\rm therm}$ when the thermal velocity is calculated with the temperatures of the emitting region, using $T = T_{\rm eff}$ (e.g. for M35MMS: $v_{\rm fit} = 7.5\,{\rm km\,s^{-1}}$ and $v_{\rm therm} = 5.7\,{\rm km\,s^{-1}}$). This difference cannot be explained by microturbulence as $v_{\rm therm}$ is the only velocity in the calculation of the thermal line

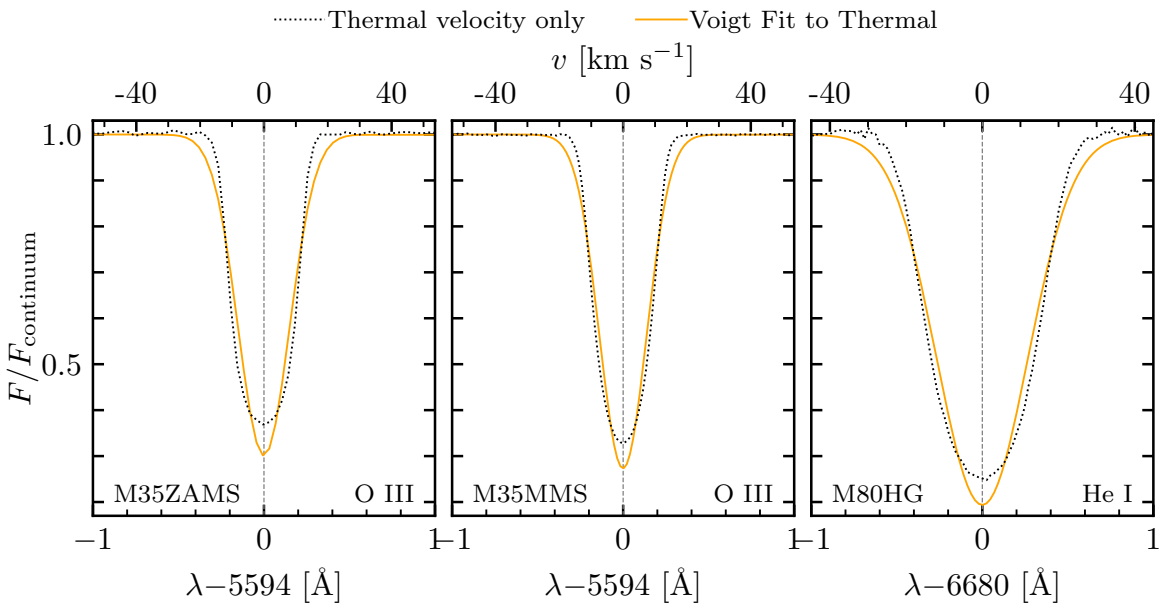

Figure 5.10: Comparison of the thermal spectral line (black dotted line from Figure 5.9) to a Voigt profile fit (orange solid line).

profiles. Thus the discrepancies are either due to the range of T across the emitting region (which vary by $\gtrsim 50\%$ about the mean) or imperfections in the projection method.

5.5 Conclusion

Three dimensional spectroscopic analysis of hot massive star surfaces is now possible using the `Sedona` Monte Carlo radiation transport code to post-process 3D RHD, LTE `Athena++` models. The turbulence excited by near-surface convection zones, predominantly those generated from the Fe and He opacity peak, create large ρ and velocity contrasts that persist through the $\tau = 1$ surface. Because of the inherent plume structure of the turbulent motions and many order of magnitude density contrasts, the $\tau = 1$

surface is not uniform in radius but rather spans several pressure scale heights resulting in factor of two variations in T. The T, ρ, and v fluctuations impact photospheric line broadening implying observed spectroscopic broadening could be used to determine the presence and strength of photospheric turbulence.

The viewing angle dependence appears to deviate from classical limb darkening predictions partially due to the small simulation domain but also due to the tangential temperature gradients generated from the dynamic plume structures at the surface. Additionally synthesized spectral lines of our models predict observable spectral line variability in Hertzsprung gap stars on several day timescales. Unfortunately, these calculations only use a small simulation domain and future calculations which mimic the full observed hemisphere of the star are needed for stronger predictions.

Though our calculated line profiles clearly exhibit the large velocities realized in our simulations, it remains to be seen whether they are well represented by the commonly used macroturbulent fitting approach of Gray (2005). For many OB stars, the only inference regarding rotation comes from broad spectral lines that yield a $v \sin i$ based on the assumption that rotation is a dominant broadening mechanism carried over from analyses of lower mass stars. Our work here may confound such inferences, as the broadening we see from turbulence alone may well exceed that from any rotation in many instances, especially stars viewed along its rotation axis. Indeed, the lack of reports of low $v \sin i$ with large $v_{\rm macro}$ speaks to this possible challenge to the rotational interpretations.

Chapter 6

Future Directions

Fundamentally, the turbulent convection that affects the stellar envelope structure occurs as luminosity approaches the Eddington luminosity, implying that our findings will be applicable to other astrophysical situations where opacity peaks arises in a near Eddington limited, radiation pressure dominated plasmas. Recent work (Jiang et al., 2016; Jiang & Blaes, 2020) has shown the iron opacity peak modifies the structure and instigates convection throughout accretion disks around active galactic nuclei (AGN) suggesting our prescription could be useful in future 1D modeling of AGN evolution. Additionally, the envelopes of all stars with masses larger than $\sim 20\,M_{\odot}$ fulfill these requirements and thus 1D models of stars in this mass range will be affected by this correlation.

Unfortunately, these 3D RHD `Athena++` simulations are computationally expensive (taking 3000 Skylake cores 4 days to run 1 model day), limiting our ability to populate the HR diagram and generate a 1D prescriptions to be used in stellar evolution models.

However, running additional 3D models would also allow for further exploration of observational consequences of near-surface convection zones. Inspired by the realization of SLF variability in our 3D RHD models, we plan to investigate if stars in other parts of the spectroscopic HR diagram with different stellar parameters generate SLF variability via NSCZs. Lower mass stars ($M \lesssim 10\,\mathrm{M}_{\odot}$) are substantially less Eddington limited, with weaker turbulent convection near the surface giving rise to a debate about the origin of their SLF variability. The amplitude of the SLF variability observed by TESS for these lower mass stars is significantly smaller (Bowman et al., 2020), which could be explained by the weaker effects of the opacity peaks. SLF variability is also present in recent observations of the SMC and LMC (e.g. Kourniotis et al. (2014); Bowman et al. (2019a); Dorn-Wallenstein et al. (2020)) and we plan to investigate how metallicity impacts the observed variability with future models.

Any newly run models could also be spectroscopically analyzed using our post-processing methodology. Once spectral lines are synthesized from hemispherical stellar surfaces, we could use the same methodology as observers to fit rotational and turbulent velocities to the spectral lines. These spectroscopic measurements could then be compared with fluid velocities in the 3D models. Many spectral lines from single ions could be synthesized and combined to make a curve of growth allowing ξ to be identified and related to intrinsic turbulent velocities of the plasma. With microturbulence quantified, v_{macro} could be identified by calculating the additional broadening needed to fit the spectral line profiles. Lastly though the models lack rotation, we could set a

bulk rotational velocity distribution to a hemispherical model and begin to probe the interplay between $v \sin i$, ξ and $v_{\rm macro}$ in massive star surfaces. Better understanding of the interplay between velocity fields in massive star surfaces could lead to a better theoretical understanding and a more physically motivated explanation of spectral line fitting parameters.

Additionally, the spectral line post-processing methodology presented in this work is not specific to our 3D RHD models of hot massive stars. Recently novel 3D red supergiant envelope models presented in Goldberg et al. (2022) could be analyzed to better understand how larger plume structures affect recent spectroscopic measurements (e.g. Guerço et al., 2022). Though these models were also run with `Athena++` any 3D model could be used in this method. An additional extension of `Athena++` using non-gray radiation transport would also allow for exploring the impact on velocity and density fluctuations as well as changes in the temperature gradient compared to the existing gray models. Additionally these methods are not specific to optical lines. Other lines could be used, however further care may be needed to ensure the non-LTE effects do not drastically alter the level populations. With these new methodologies, a comprehensive spectroscopic analysis of massive star surfaces is within reach.

A remaining research project not completed in this thesis involves comparing the observational characteristics (SLF variability and spectral line broadening) of the varied metallicity models that are already computed (M8056Z0.1, M80HGZ0.1, M80HGZ2). These models are not ideal as they are over-luminous for their mass and therefore cannot

be directly be compared with observations. However preforming the same SLF variability and spectroscopic analysis as the solar metallicity models (M56HG and M80HG), we could extract a trend to compare with the observed trends.

Beyond this, further 3D RHD stellar envelope models need to be computed and there are many directions these explorations could take. Running a M35MMS-like model at Large Magellanic Cloud metallicity would allow for an investigation of the metallicity dependence of both SLF variability and spectroscopic broadening. Additionally, running a higher mass ($60 - 80\,M_{\odot}$) stellar envelope model with $\tau_{\rm Fe} \gtrsim \tau_{\rm crit}$ would both gain another model for comparison with observations and explore the upper transition to the regime where turbulence dominates the envelope structure. It would be advantageous to ground this high mass regime in the observations as we have done with the M35MMS and M13TAMS models.

Disentangling the velocity fields from spectral lines remains the direction of most interest, however it is also the most computationally expensive. For rotation to impact spectral line widths in a turbulent envelope, $v \sin i$ must be comparable to $v_{\rm macro}$, implying the rotation will be at a significant fraction of the critical rotation rate of the star. Thus latitude-dependent effects, like the Coriolis force and limb darkening, will impact both the envelope structure as well as the photospheric line generation. Thus a single narrow wedge model near the equator will not reliably recreate a synthetic spectral line, rather to accurately investigate the interplay between rotation and turbulent surface velocities, several 3D RHD simulations are needed for the same stellar model making this the most

expensive expansion of this work.

Appendix A

1D Velocity Estimates

After discovering the extremes of radiative leakage in the $\tau \ll \tau_{\rm crit}$ regime, we set out to find an independent way to estimate convective velocities rather than relying on MLT. In this regime, the convective flux is so small that classical 1D convection theories are not entirely reliable as $F_{\rm conv}/F_{\rm rad} \lesssim 1\%$. The main goals were to decrease the number of free parameters that could be tweaked and reliably match the 3D model velocities with realistic values for the free parameters. MLT relies on α as a coefficient to the scale height that sets the eddy turnover scale and Henyey et al. (1965) uses y to account for the temperature structure of the plumes which determines the plumes' ability to lose heat. Thus we began from first principles to attempt to generate an estimation of convective velocities.

For this calculation, we will only consider convection in NSCZs excited by opacity peaks and thus assume the gravitational potential will follow $g \propto r^{-2}$. Imagine a coherent

plume of material that is slightly perturbed from the surrounding, hydrostatic stellar envelope structure in a 1D model. The goal is to calculate how the plume will move relative to the static stellar background. The fundamental acceleration lifting the plume is buoyancy, however this is counteracted by a ρv^2 drag force. Thus the radial acceleration is given by

$$\frac{dv_r}{dt} = \frac{\rho_s - \rho_b}{\rho_s}\frac{GM}{r^2} - \mathrm{sgn}(v_r)\rho_b * v_r^2 * \pi(l/2)^2/m_b, \tag{A.1}$$

where ρ_s is the background density of the star; and ρ_b, v_r, l, $m_b = 4\pi(l/2)^3\rho/3$ are the density, radial velocity, width, and mass of the convective blob respectively. The sign convention is chosen such that the plume rises, or $\frac{dv_r}{dt} > 0$, when $\rho_b < \rho_s$.

As these models are often radiation pressure dominated, utilizing overdensities are not as reliable as comparing the temperatures of the plume and the stellar background, T_b and T_s respectively. To find the relation between ρ_b and T_b we assume that the bubble is in pressure equilibrium with the star, or $P_s = P_b$ (assuming $P = P_\mathrm{g} + P_\mathrm{r}$ as $P_\mathrm{turb} \ll (P_\mathrm{g} + P_\mathrm{r})$ when $\tau \ll \tau_\mathrm{crit}$). Solving for ρ_b, we find

$$\rho_b = \frac{1}{R_g T_b}\left(\rho_s R_g T_s + \frac{a}{3}(T_s^4 - T_b^4)\right) = \frac{1}{R_g T_b}\left(P_{\mathrm{therm},s} - \frac{a}{3}T_b^4\right). \tag{A.2}$$

Thus it is possible to determine the radial acceleration with only the blob's temperature and stellar quantities.

As the blob moves throughout the envelope, its temperature will evolve. In order to track the temperature evolution, we begin by utilizing the time evolution of the plume's entropy, which matches the divergence of the its energy flux, or

$$T\frac{ds_b}{dt} = \frac{-1}{\rho_b}\nabla \cdot \vec{F}_b \tag{A.3}$$

where s_b is the entropy per unit mass of the blob and $\vec{F}_b$ is the radiative flux leaving the blob as it moves. The entropy density is defined as $s \equiv R_g \ln(T^{3/2}/\rho) + 4aT^3/3\rho$ and assuming the flux is purely radiative diffusion,

$$\nabla \cdot \vec{F}_b \approx \frac{1}{l} \frac{ac}{3\kappa_b \rho_b} \frac{T_b^4 - T_s^4}{l} \tag{A.4}$$

where l is a free parameter for the size of the bubble or plume.

Differentiating the definition of the entropy density and combining it with Equation A.4 in Equation A.3, we find a differential equation following the evolution of both T_b and ρ_b,

$$\frac{dT_b}{dt}\left(\frac{3R_g}{2T_b} + \frac{4aT_b^2}{\rho_b}\right) - \frac{d\rho_b}{dt}\left(\frac{4aT_b^4}{3\rho_b^2} + \frac{R_g}{\rho_b}\right) = \frac{-1}{l^2\rho_b^2}\frac{ac}{3T_b\kappa_b}(T_b^4 - T_s^4). \tag{A.5}$$

Directly differentiating Equation A.2 results in the time derivative of ρ_b,

$$\frac{d\rho_b}{dt} = \frac{1}{R_g T_b}\left[\frac{dP_{\text{therm},s}}{dr} v_r - \frac{dT_b}{dt}\left(\frac{P_{\text{therm},s}}{T_b} + aT_b^3\right)\right], \tag{A.6}$$

where $\frac{dP_{\text{therm},s}}{dr}$ is the thermal pressure gradient from the stellar background and can be numerically estimated from the 1D model. Combining Eqs. A.6 and A.5 we isolate $\frac{dT_b}{dt}$,

$$\begin{aligned} \tfrac{dT_b}{dt} &= \tfrac{numer}{denom} \\ numer &= \tfrac{-1}{l^2\rho_b^2}\tfrac{ac}{3T_b\kappa_b}(T_b^4 - T_s^4) + \tfrac{\nabla P_{\text{therm},s} v_r}{R_g T_b}\left(\tfrac{R_g}{\rho_b} + \tfrac{4aT_b^3}{3\rho_b^2}\right) \\ denom &= \tfrac{3R_g}{2T_b} + \tfrac{4aT_b^2}{\rho_b} + \tfrac{1}{R_g T_b}\left(\tfrac{R_g}{\rho_b} + \tfrac{4aT_b^3}{3\rho_b^2}\right)\left(\tfrac{P_{\text{therm},s}}{T_b} + aT_b^3\right). \end{aligned} \tag{A.7}$$

Without a perturbation, $T_b = T_s$ and $v_r = 0$, thus no velocities would be generated. To initiate the motion, we perturbed the plume by shifting it a small fraction of the scale height above the starting location adiabatically. The exact size of the shift did not significantly impact the results when less than a 1% change was made. Numerically integrating Eqs. A.1 and A.7 results in the time evolution of the location, velocity, and

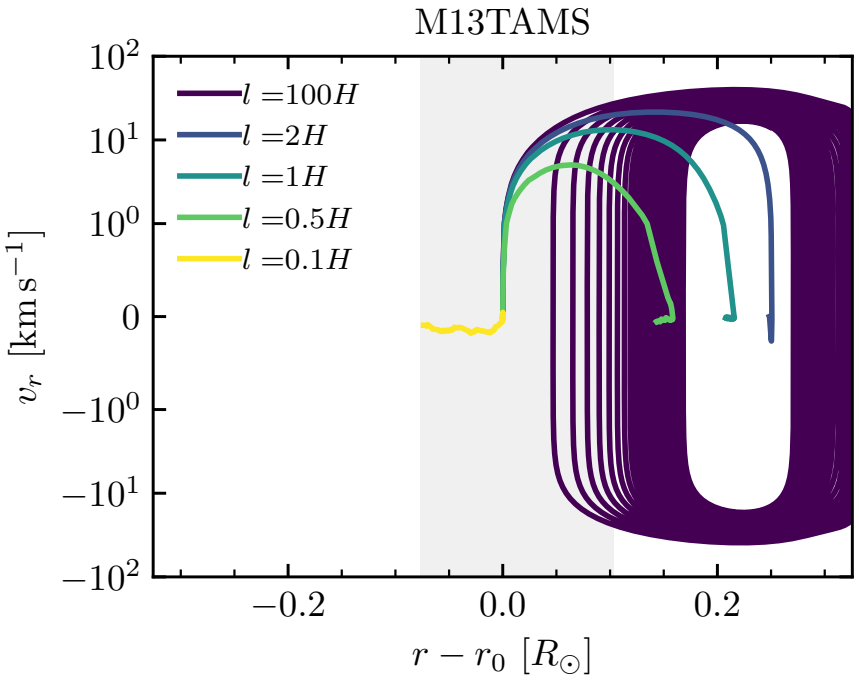

Figure A.1: Velocity evolution when numerically integrating Eqs. A.1 and A.7 using the 1D average of M13TAMS as the stellar background model plotted versus radius normalized by the integration starting location, r_0. Different lines represent different plume sizes defined by coefficients multiplied by the pressure scale heights. Shaded regions shows the negative entropy gradient which distinguishes the convection zone.

temperature of the plume as it moves through the NSCZs.

Figure A.1 shows the results of the numerical integration using a 1D average of M13TAMS as the stellar background. The temporal integration was performed for 5 days and the lines are generated using a 10 second resolution. For large l, we see adiabatic-like behavior with mild radiative leakage. The plume rises until it is close to the photosphere (right limit of the plot) before turning around and falling back into the model. Due to the radiative leakage, the plume approaches thermal equilibrium with the background before returning to the initial perturbation radius, resulting in the converging loops in Fig-

ure A.1. For smaller l, the plumes experience an initial acceleration out of the convection zone, but fails to fall back as the radiative leakage allows for thermal equilibrium faster than the downward velocity can overcome the drag resistance. The interplay between the small, downward acceleration from the temperature contrast and the drag friction results in the noise-like behavior with small negative velocities. For $l = 0.1H$, the plume loses all of its heat contrast quickly resulting in almost no vertical motion and thus quickly enters the noisy balance of acceleration and drag.

When $l \approx 1$ the results of our integration are comparable to those of classical MLT with the default parameters ($\alpha = 1.6$, $y = 1/3$). For M13TAMS, $v_r = 12\,\mathrm{km\,s^{-1}}$ at the top of the convection zone, matching the MESA prediction of $v_c = 11\,\mathrm{km\,s^{-1}}$ with one fewer free parameter suggesting MLT is reproducing the behavior of these equations in the $\tau \ll \tau_{\mathrm{crit}}$ regime. Reducing $l \approx 0.8H$ in our calculations reproduces the smaller convective velocities seen in the 3D models ($v_c = 8\,\mathrm{km\,s^{-1}}$). Despite this success, more work is needed to develop a method to estimate the convective velocity realized in 3D models using 1D profiles.

Bibliography

Aerts, C., Puls, J., Godart, M., & Dupret, M. A. 2009, A&A, 508, 409

Aerts, C., & Rogers, T. M. 2015, ApJL, 806, L33

Bowman, D. M. 2020, Frontiers in Astronomy and Space Sciences, 7, 70

Bowman, D. M., Burssens, S., Simón-Díaz, S., et al. 2020, A&A, 640, A36

Bowman, D. M., Burssens, S., Pedersen, M. G., et al. 2019a, Nature Astronomy, 3, 760

Bowman, D. M., Aerts, C., Johnston, C., et al. 2019b, A&A, 621, A135

Bowman, D. M., Vandenbussche, B., Sana, H., et al. 2022, arXiv e-prints, arXiv:2208.01533

Bromm, V., & Larson, R. B. 2004, ARA&A, 42, 79

Burssens, S., Simón-Díaz, S., Bowman, D. M., et al. 2020, A&A, 639, A81

Cantiello, M., & Braithwaite, J. 2019, ApJ, 883, 106

Cantiello, M., Lecoanet, D., Jermyn, A. S., & Grassitelli, L. 2021, ApJ, 915, 112

Cantiello, M., Langer, N., Brott, I., et al. 2009, A&A, 499, 279

Chiavassa, A., Plez, B., Josselin, E., & Freytag, B. 2009, A&A, 506, 1351

Chiavassa, A., Pasquato, E., Jorissen, A., et al. 2011, A&A, 528, A120

Couston, L.-A., Lecoanet, D., Favier, B., & Le Bars, M. 2018, Journal of Fluid Mechanics, 854, R3

Cox, J. P., & Giuli, R. T. 1968, Principles of Stellar Structure (Gordon and Breach, New York)

Crowther, P. A. 2007, ARA&A, 45, 177

David-Uraz, A., Owocki, S. P., Wade, G. A., Sundqvist, J. O., & Kee, N. D. 2017, MNRAS, 470, 3672

Davis, S. W., Jiang, Y.-F., Stone, J. M., & Murray, N. 2014, ApJ, 796, 107

Davis, S. W., Stone, J. M., & Jiang, Y.-F. 2012, The Astrophysical Journal Supplement Series, 199, 9

Dorn-Wallenstein, T. Z., Levesque, E. M., Neugent, K. F., et al. 2020, ApJ, 902, 24

Dravins, D., Ludwig, H.-G., & Freytag, B. 2021, A&A, 649, A16

Eastman, R. G., & Pinto, P. A. 1993, ApJ, 412, 731

Edelmann, P. V. F., Ratnasingam, R. P., Pedersen, M. G., et al. 2019, ApJ, 876, 4

Farmer, R., Fields, C. E., Petermann, I., et al. 2016, ApJS, 227, 22

Foreman-Mackey, D., Hogg, D. W., Lang, D., & Goodman, J. 2013, PASP, 125, 306

Freytag, B., & Höfner, S. 2008, A&A, 483, 571

Freytag, B., Steffen, M., & Dorch, B. 2002, Astronomische Nachrichten, 323, 213

Goldberg, J. A., Jiang, Y.-F., & Bildsten, L. 2021, arXiv e-prints, arXiv:2110.03261

—. 2022, ApJ, 929, 156

Goldreich, P., & Kumar, P. 1990, ApJ, 363, 694

Gräfener, G., Owocki, S. P., & Vink, J. S. 2012, A&A, 538, A40

Grassitelli, L., Fossati, L., Simón-Diáz, S., et al. 2015, ApJL, 808, L31

Gray, D. F. 2005, The Observation and Analysis of Stellar Photospheres (Cambridge University Press, New York)

Gronenschild, E. H. B. M., & Mewe, R. 1978, A&AS, 32, 283

Guerço, R., Smith, V. V., Cunha, K., et al. 2022, MNRAS, arXiv:2208.10529 [astro-ph.SR]

Harris, C. R., Millman, K. J., van der Walt, S. J., et al. 2020, Nature, 585, 357–362

Heger, A., Fryer, C. L., Woosley, S. E., Langer, N., & Hartmann, D. H. 2003, ApJ, 591, 288

Henyey, L., Vardya, M. S., & Bodenheimer, P. 1965, ApJ, 142, 841

Hillier, D. J. 2012, in From Interacting Binaries to Exoplanets: Essential Modeling Tools, ed. M. T. Richards & I. Hubeny, Vol. 282, 229

Holgado, G., Simón-Díaz, S., Herrero, A., & Barbá, R. H. 2022, arXiv e-prints, arXiv:2207.12776

Hunter, J. D. 2007, Computing in Science Engineering, 9, 90

Iglesias, C. A., & Rogers, F. J. 1996, ApJ, 464, 943

Jermyn, A. S., Anders, E. H., Lecoanet, D., Cantiello, M., & Goldberg, J. A. 2022, Research Notes of the American Astronomical Society, 6, 29

Jermyn, A. S., & Cantiello, M. 2020, ApJ, 900, 113

Jermyn, A. S., Bauer, E. B., Schwab, J., et al. 2023, ApJS, 265, 15

Jiang, Y.-F. 2021, ApJS, 253, 49

Jiang, Y.-F., & Blaes, O. 2020, arXiv e-prints, arXiv:2006.08657

Jiang, Y.-F., Cantiello, M., Bildsten, L., Quataert, E., & Blaes, O. 2015, The Astrophysical Journal, 813, 74

Jiang, Y.-F., Cantiello, M., Bildsten, L., Quataert, E., & Blaes, O. 2017, ApJ, 843, 68

Jiang, Y.-F., Cantiello, M., Bildsten, L., et al. 2018, Nature, 561, 498

Jiang, Y.-F., Davis, S. W., & Stone, J. M. 2016, ApJ, 827, 10

Jiang, Y.-F., Stone, J. M., & Davis, S. W. 2012, ApJS, 199, 14

Jiang, Y.-F., Stone, J. M., & Davis, S. W. 2014, The Astrophysical Journal Supplement Series, 213, 7

Joss, P. C., Salpeter, E. E., & Ostriker, J. P. 1973, ApJ, 181, 429

Kasen, D., Thomas, R. C., & Nugent, P. 2006, ApJ, 651, 366

Kennicutt, R. C. 2005, in IAU Symposium, Vol. 227, Massive Star Birth: A Crossroads of Astrophysics, ed. R. Cesaroni, M. Felli, E. Churchwell, & M. Walmsley, 3

Köhler, K., Langer, N., de Koter, A., et al. 2015, A&A, 573, A71

Kourniotis, M., Bonanos, A. Z., Soszyński, I., et al. 2014, A&A, 562, A125

Kozyreva, A., Nakar, E., Waldman, R., Blinnikov, S., & Baklanov, P. 2020, MNRAS, 494, 3927

Krtička, J., & Feldmeier, A. 2018, A&A, 617, A121

—. 2021, A&A, 648, A79

Krumholz, M. R., & Thompson, T. A. 2012, ApJ, 760, 155

—. 2013, MNRAS, 434, 2329

Kuhfuss, R. 1986, A&A, 160, 116

Kurucz, R. L., & Bell, B. 1995, Atomic line list (Cambridge, MA)

Lecoanet, D., & Quataert, E. 2013, MNRAS, 430, 2363

Lecoanet, D., Cantiello, M., Quataert, E., et al. 2019, ApJL, 886, L15

Lomb, N. R. 1976, Ap&SS, 39, 447

Ludwig, H.-G., Freytag, B., & Steffen, M. 1999, A&A, 346, 111

MacDonald, J., & Petit, V. 2019, MNRAS, 487, 3904

Maeder, A. 1987, A&A, 173, 247

Maeder, A., Georgy, C., Meynet, G., & Ekström, S. 2012, A&A, 539, A110

Moffat, A. F. J., Marchenko, S. V., Zhilyaev, B. E., et al. 2008, ApJL, 679, L45

Owocki, S. P. 2015, in Astrophysics and Space Science Library, Vol. 412, Very Massive Stars in the Local Universe, ed. J. S. Vink, 113

Owocki, S. P., & Sundqvist, J. O. 2018, MNRAS, 475, 814

Paxton, B., Bildsten, L., Dotter, A., et al. 2011, ApJS, 192, 3

Paxton, B., Cantiello, M., Arras, P., et al. 2013, ApJS, 208, 4

Paxton, B., Marchant, P., Schwab, J., et al. 2015, ApJS, 220, 15

Paxton, B., Schwab, J., Bauer, E. B., et al. 2018, ApJS, 234, 34

Paxton, B., Smolec, R., Schwab, J., et al. 2019, ApJS, 243, 10

Ricker, G. R., Winn, J. N., Vanderspek, R., et al. 2015, Journal of Astronomical Telescopes, Instruments, and Systems, 1, 014003

Rogers, T. M., Lin, D. N. C., McElwaine, J. N., & Lau, H. H. B. 2013, ApJ, 772, 21

Rosdahl, J., & Teyssier, R. 2015, MNRAS, 449, 4380

Rybicki, G. B., & Lightman, A. P. 1979, Radiative processes in astrophysics (Wiley-VCH)

Santolaya-Rey, A. E., Puls, J., & Herrero, A. 1997, A&A, 323, 488

Sanyal, D., Grassitelli, L., Langer, N., & Bestenlehner, J. M. 2015, A&A, 580, A20

Scargle, J. D. 1982, ApJ, 263, 835

Schultz, W. C., Bildsten, L., & Jiang, Y.-F. 2020, ApJ, 902, 67

—. 2022, ApJL, 924, L11

Schultz, W. C., Tsang, B. T. H., Bildsten, L., & Jiang, Y.-F. 2023, ApJ, 945, 58

Simón-Díaz, S., Aerts, C., Urbaneja, M. A., et al. 2018, A&A, 612, A40

Simón-Díaz, S., Godart, M., Castro, N., et al. 2017, A&A, 597, A22

Simón-Díaz, S., Herrero, A., Sabín-Sanjulián, C., et al. 2014, A&A, 570, L6

Simón-Díaz, S., Herrero, A., Uytterhoeven, K., et al. 2010, ApJL, 720, L174

Smith, N. 2014, ARA&A, 52, 487

Smith, N., Vink, J. S., & de Koter, A. 2004, ApJ, 615, 475

Stone, J. M., Tomida, K., White, C. J., & Felker, K. G. 2020, The Athena++ Adaptive Mesh Refinement Framework: Design and Magnetohydrodynamic Solvers, arXiv:2005.06651 [astro-ph.IM]

Stothers, R., & Chin, C. W. 1979, ApJ, 233, 267

Sundqvist, J. O., Petit, V., Owocki, S. P., et al. 2013, MNRAS, 433, 2497

Thyng, K. M., Greene, C. A., Hetland, R. D., Zimmerle, H. M., & DiMarco, S. F. 2016, Oceanography

Townsend, R. H. D. 2010, ApJS, 191, 247

Tsang, B. T. H., Goldberg, J. A., Bildsten, L., & Kasen, D. 2020, ApJ, 898, 29

Tsang, B. T. H., & Milosavljević, M. 2015, MNRAS, 453, 1108

—. 2018, MNRAS, 478, 4142

Tsang, B. T. H., & Schultz, W. C. 2019, ApJL, 877, L14

van der Velden, E. 2020, The Journal of Open Source Software, 5, 2004

Verner, D., Yakovlev, D., Band, I., & Trzhaskovskaya, M. 1993, Atomic Data and Nuclear Data Tables, 55, 233

Verner, D. A., Verner, E. M., & Ferland, G. J. 1996, Atomic Data and Nuclear Data Tables, 64, 1

Virtanen, P., Gommers, R., Oliphant, T. E., et al. 2020, Nature Methods, 17, 261

Wolf, W. M., & Schwab, J. 2017, wmwolf/py_mesa_reader: Interact with MESA Output